THÈSE

présentée pour l'obtention du grade de

Docteur

de

L'Université Paris 13

Spécialité: Mécanique et Matériaux

et de

L'Université de Science et Technologie AGH de Cracovie

par

Marcin Wroński

Etude expérimentale et modélisation du laminage asymétrique d'alliages de titane et d'aluminium

soutenue publiquement **le 18 octobre 2013 à Cracovie**
devant le jury composé de

M. **Pierre Gilormini**, Directeur de recherche CNRS, PIMM, ENSAM ParisTech (France), rapporteur
M. **Luzny Wojciech**, Professeur, Université AGH (Pologne), rapporteur
M. **Yann Charles**, Maître de Conférences, Université Paris 13 (France), examinateur
M. **Czeskaw Kapusta**, Professeur, Université AGH (Pologne), examinateur
M. **Alain Lodini**, Professeur, Université de Reims (France), examinateur
M. **Jacek Tarasiuk**, Professeur, Université AGH (Pologne), examinateur
Mme **Brigitte Bacroix**, Directeur de recherche CNRS, LSPM, Université Paris 13, directrice de thèse
M. **Krzysztof Wierzbanowski**, Professeur, Université AGH (Pologne), directeur de thèse

Faculty of Physics and Applied Computer Science
AGH University of Science and Technology,
Kraków, Poland

LSPM – CNRS,
Université Paris 13, PRES Sorbonne Paris Cité
99. av. J.B. Clément, 93430 Villetaneuse, France

DISSERTATION

submitted for the degree of

Doctor

of

Paris 13 University

Specialty: Mechanics and Materials

and of

AGH University of Science and Technology,

by

Marcin Wroński

Modelling and experimental study of asymmetric rolling of titanium and aluminium

Defended publicly on October 18th, 2013 in Kraków
In the presence of the committee composed of

M. **Pierre Gilormini**, CNRS Research Scientist, PIMM, ENSAM ParisTech (France), referee
M. **Luzny Wojciech**, Professor, AGH University (Poland), referee
M. **Yann Charles**, Associate Professor, Paris 13 University (France), examiner
M. **Czeskaw Kapusta**, Professor, AGH University (Poland), examiner
M. **Alain Lodini**, Professor, University of Reims (France), examiner
M. **Jacek Tarasiuk**, Professor, AGH University (Poland), examiner
Mme **Brigitte Bacroix**, CNRS Research Scientist, LSPM, Université Paris 13, PhD supervisor
M. **Krzysztof Wierzbanowski**, Professor, AGH University (Poland), PhD supervisor

Faculty of Physics and Applied Computer Science
AGH University of Science and Technology,
Kraków, Poland

LSPM – CNRS,
Université Paris 13, PRES Sorbonne Paris Cité
99. av. J.B. Clément, 93430 Villetaneuse, France

Acknowledgements

First of all I would like to thank my supervisors: Prof. Krzysztof Wierzbanowski and Dr Brigitte Bacroix for their guidance and help.

I am also grateful to all the members of my French – Polish PhD committee for the time they spend reading my thesis and elaborating their report.

Thanks are also due to Dr Sebastian Wroński, and Dr Andrzej Baczmański from AGH and to O. Brinza and Th. Chauveau from LSPM for discussions and assistance in carrying out many experiments using X-ray diffraction and EBSD and to Dr Mirosław Wróbel for help in preparing some samples.

I am grateful to Dr Torben Leffers for his remarks and help in a part of computer simulations. Thanks to his great assistance, Chapter 2 was much improved.

Finally, I would like to express my gratefulness for my family and especially for my wife Barbara for her patience and support.

This PhD thesis has been completed within the framework of the Human Capital Operational Program POKL.04.01.01-00-434/08-02 co-financed by the European Union. The work was also partly supported by the grant of Polish National Centre for Science (NCN): DEC-2011/01/B/ST8/07394

Table of Contents

Streszczenie

W otaczającym nas świecie współczesnej technologii wzrasta zapotrzebowanie na materiały konstrukcyjne posiadające określone własności. Ich projektowanie i wytwarzanie jest jednym z najważniejszych zadań fizyki ciała stałego i nauki o materiałach. W ostatnich latach obserwuje się dynamiczny rozwój technik formowania metali, które wpływają radykalnie na zmianę ich właściwości fizycznych. Wiele z nich opiera się na procesach odkształcenia plastycznego bądź też intensywnego odkształcenia plastycznego. Celem postawionym przez autora niniejszej pracy jest zbadanie i zrozumienie mechanizmów deformacji materiałów polikrystalicznych, występujących podczas złożonych odkształceń plastycznych. Proces walcowania asymetrycznego został wybrany jako przykład takiego odkształcenia. Badania przeprowadzone zostały dla dwóch polikrystalicznych materiałów: aluminium 6061 (o sieci krystalicznej regularnej ściennie centrowanej) i tytanu Grade 2 (o sieci heksagonalnej). Wybór tych materiałów nie był przypadkowy, gdyż skupiono uwagę na materiałach posiadających zastosowania technologiczne i przemysłowe. Aluminium i tytan są właśnie takimi materiałami; wykorzystywane są one m. in. w przemyśle lotniczym, motoryzacyjnym (Al, Ti) oraz w implantologii (Ti). W pracy użyto dwóch technik eksperymentalnych: dyfrakcji elektronów wstecznie rozproszonych (EBSD) oraz dyfrakcji rentgenowskiej. Zbadano wpływ asymetrii procesu walcowania na teksturę krystalograficzną oraz na mikrostrukturę materiałów. Wyniki pomiarów zostały porównane z wynikami obliczeń. Zastosowany w pracy model odkształcenia sprężysto-plastycznego jest użytecznym narzędziem w badaniu materiałów polikrystalicznych. Modelowanie jest bowiem pierwszym etapem w procesie projektowania nowoczesnych materiałów. Dzięki niemu można przewidywać makroskopowe własności materiału bazując na znajomości parametrów mikrostruktury.

W pierwszym rozdziale pracy opisane zostały podstawowe krystalograficzne mechanizmy odkształcenia plastycznego: poślizg oraz bliźniakowanie. Zostały również opisane: prawo oddziaływania pomiędzy ziarnami a otaczającym je materiałem oraz prawo umocnienia systemów ścinania (poślizgu i bliźniakowania). Mechanizmy te zostały włączone do modelu LW odkształcenia materiałów polikrystalicznych (model Leffers'a-Wierzbanowskiego). Model ten pozwala przewidywać makroskopowe własności materiału (teksturę krystalograficzną, krzywe rozciągania, rozkład naprężeń wewnętrznych i własnych, itp.) w oparciu o parametry mikrostrukturalne (poślizg krystalograficzny, bliźniakowanie,

prawo umocnienia, początkowa tekstura krystalograficzna, początkowy stan naprężeń własnych, itp.).

W rozdziale 2 został omówiony znany z literatury problem występowania dwóch typów tekstur walcowania metali i stopów o sieci regularnej ściennie centrowanej, a mianowicie tekstur typu miedzi i mosiądzu. Przykładowo, miedź i mosiądz posiadają tę samą strukturę krystaliczną, jak i te same systemy poślizgu, a jednak w procesie walcowania uzyskują różne tekstury. Problem ten jest istotny, gdyż jednym z badanych w niniejszej pracy materiałów jest aluminium, który posiada teksturę walcowania typu miedzi. W ramach modelu LW zbadane zostały różne parametry oraz mechanizmy odkształcenia w aspekcie ewentualnego przejście między teksturą typu miedzi i mosiądzu (np. silne lub słabe oddziaływanie ziarna z otoczeniem, dwie definicje obrotu sieci krystalicznej, bliźniakowanie mechaniczne, a także aktywacja dodatkowych systemów poślizgu). Przewidywane tekstury zostały przeanalizowane i porównane ilościowo z danymi doświadczalnymi. Zaproponowano proste wyjaśnienie powstawania obu typów tekstury w metalach o sieci regularnej ściennie centrowanej.

W rozdziale trzecim opisany został sposób połączenia modelu odkształcenia w skali makro, opartego na metodzie elementów skończonych (MES), z modelem w skali mikro czyli modelem krystalograficznym (LW). Istotą metody elementów skończonych jest zastąpienie analizowanego obiektu trójwymiarowego zbiorem oddzielnych elementów, np., prostopadłościennych. Jednym z istotnych ograniczeń metody elementów skończonych jest pominięcie krystalicznej struktury badanych materiałów. W klasycznym podejściu MES materiał jest traktowany jako jednorodny ośrodek ciągły o określonych własnościach. Jednym z celów pracy było stworzenie nowego narzędzia, które pozwoliłoby modelować procesy o złożonej geometrii, uwzględniając przy tym krystaliczną strukturę materiałów. Środowiskiem obliczeniowym opartym na MES i wykorzystanym w pracy jest pakiet obliczeniowy ABAQUS. Jest to zaawansowany program umożliwiający rozwiązywanie złożonych problemów inżynierskich. Model LW został zaimplementowany do ABAQUS-a przy pomocy zewnętrznej funkcji użytkownika VUMAT. Procedura ta pozwala użytkownikowi wprowadzić własną definicję materiału. Poprawność powyższej implementacji (MES+LW) została sprawdzona na podstawie testów rozciągania. Obliczone tekstury krystalograficzne zostały porównane z tekturami zmierzonymi. Przetestowany w ten sposób model (MES+LW) został następnie użyty do modelowania procesów o złożonej geometrii, jak badane w niniejszej pracy walcowanie asymetryczne (sam model krystalograficzny, LW, nie jest wystarczającym narzędziem do badania procesów o dużej niejednorodności odkształcenia).

W rozdziale 4 zbadano wpływ walcowania asymetrycznego na zmiany tekstury krystalograficznej oraz mikrostruktury w polikrystalicznym aluminium i tytanie. W pierwszej części rozdziału zostały przedstawione szczegóły dotyczące samego eksperymentu. Walcowanie asymetryczne przeprowadzono na specjalnej walcarce, której dwa jednakowe walce napędzane są niezależnymi silnikami. Asymetria procesu definiowana jest jako stosunek prędkości kątowych obu walców. W celu wyjaśnienia wpływu asymetrii walcowania na teksturę oraz na mikrostrukturę materiału użyto dwóch technik doświadczalnych: dyfrakcji rentgenowskiej (pomiar tekstury) oraz techniki EBSD. W wyniku pomiarów metodą EBSD otrzymujemy mapy powierzchni, które dają nam jednocześnie informację o topografii ziaren jak i ich orientacji krystalograficznej. Próbki aluminiowe zostały zwalcowane do zgniotu 36%. W przypadku tytanu badano dwie grupy próbek: próbki o niskim i średnim odkształceniu (zgniot: 20% i 40%) oraz próbki silnie odkształcone (zgniot: 60%, 70% i 80%) i następnie rekrystalizowane. Na podstawie danych z pomiarów EBSD dla wszystkich próbek zostały wykonane analizy statystyczne. Wyznaczono tekstury oraz parametry charakteryzujące mikrostrukturę (np. średnią wielkość ziaren) oraz jej rozdrobnienie. Istotnym rezultatem walcowania asymetrycznego jest stwierdzenie większego rozdrobnienia mikrostruktury materiałów oraz, w wielu przypadkach, zmniejszenie się średniej wielkości ziaren (w porównaniu z walcowaniem symetrycznym). Ten ostatni efekt występuje szczególnie wyraźnie w materiałach walcowanych asymetrycznie i zrekrystalizowanych.

W ostatnim rozdziale zostały przedstawione i omówione obliczenia modelowe dla procesu walcowania symetrycznego i asymetrycznego. Wszystkie obliczenia zostały wykonane przy użyciu modelu (MES+LW), opisanego w rozdziale trzecim. Jest to bardzo użyteczne narzędzie obliczeniowe, umożliwiające badanie niejednorodności odkształcenia plastycznego w głąb próbki z uwzględnieniem polikrystalicznej struktury materiałów. Model ten był używany do przewidywania ewolucji tekstury jak i znalezienia rozkładu naprężeń wewnętrznych w materiale podczas walcowania symetrycznego i asymetrycznego (dla różnych stopni asymetrii walcowania). We wszystkich przypadkach, przewidywane tekstury zostały porównane z teksturami doświadczalnymi i stwierdzono dobrą zgodność. Stwierdzono, że walcowanie asymetryczne modyfikuje teksturę (w porównaniu z walcowaniem symetrycznym) i prowadzi do jej jednorodnego rozkładu w objętości materiału.

Résumé

Dans la quête incessante de matériaux à propriétés améliorées, pour une plus grande durabilité et un allègement des structures, le développement de simulations numériques des processus de mise en forme plus fiables est plus que jamais d'actualité. Or, la compréhension et la modélisation des mécanismes d'écrouissage et de restauration actifs lors de sollicitations dites complexes sont encore largement insuffisantes pour un grand nombre d'alliages métalliques pour que les simulations de processus de mise en forme puissent être qualifiées de prédictives. Par ailleurs, il est également important de pouvoir modifier les procédés standard de mise en forme afin d'optimiser celle-ci en développant de nouveaux procédés permettant par exemple un affinage de la taille de grain, paramètre important pour optimiser les propriétés mécaniques finales.

Parmi ces nouveaux procédés, ceux dits de déformation plastique sévères sont largement étudiés : on peut citer par exemple l'extrusion coudée à aires égales (EqualChannel Angular Pressing, ECAP), le co-laminage cumulatif (Accumulative Roll Bonding, ARB), la torsion sous haute pression (High Pressure Torsion, HPT), le laminage asymétrique (Asymetrical Rolling, AR), ... Toutes ces méthodes permettent d'imposer de grandes déformations au matériau sans dommage, et modifient fortement les microstructures formées. Notamment, on recherche souvent à fragmenter les grains, ce qui permet d'avoir in fine une taille de grain réduite, synonyme de résistance mécanique accrue. Parmi ces méthodes, le laminage asymétrique est particulièrement intéressant par le fait qu'il est beaucoup plus facilement implantable en milieu industriel que les autres méthodes.

Dans ce contexte, l'objectif de ce travail de thèse est donc double : il s'agit tout d'abord d'étudier plus à fond le procédé de laminage asymétrique et notamment son influence sur les modifications de microstructures, d'anisotropie et de propriétés mécaniques de deux alliages métalliques retenus en raison de leur intérêt pour la mise en forme ; on se propose ensuite de s'appuyer sur les résultats expérimentaux obtenus afin d'améliorer la loi de comportement des matériaux étudiés utilisée dans le cadre des simulations par éléments finis.

Les deux matériaux retenus sont un alliage d'aluminium (de grade 6061) de structure cubique à faces centrées (cfc) et un titane de pureté commerciale (de grade 2) de structure hexagonale compacte (hc). Le laminoir asymétrique implanté récemment au LSPM qui permet d'imposer de forts taux d'asymétrie (et donc de grandes rotations) a été retenu comme mode de déformation et le suivi des microstructures et des textures cristallographiques a été

réalisé par EBSD (Electron Back Scattering Diffraction) et diffraction des rayons X. L'influence du laminage asymétrique sur les évolutions microstructurales a pu être ainsi analysée en détails et a permis de proposer des paramètres matériau pour les lois de comportement utilisées dans les modèles. Ensuite, en couplant un modèle micromécanique à un code d'éléments finis, les simulations réalisées ont permis d'étudier l'influence du laminage asymétrique sur les propriétés mécaniques.

Plus précisément, les objectifs que nous nous sommes fixés ont été les suivants :

- Caractériser qualitativement et quantitativement les évolutions microstructurales des deux alliages lors du laminage asymétrique, en fonction des paramètres procédé retenus ;
- Identifier les paramètres matériaux de la loi de comportement cristalline utilisée dans la partie modélisation, à partir des observations microstructurales et d'essais mécaniques simples ;
- Coupler un modèle de type polycristallin à un code d'éléments finis, afin de réaliser des simulations de mise en forme permettant d'accéder non seulement aux évolutions des grandeurs mécaniques mais également aux évolutions de texture ;
- Valider le modèle de comportement retenu par confrontation des résultats expérimentaux et numériques (textures surtout).
- Discuter finalement de la pertinence du laminage asymétrique pour améliorer les propriétés d'emploi des tôles déformées (avec ou sans recuit après laminage).

Le mémoire de thèse est structuré en 5 chapitres principaux, encadrés par une introduction et une conclusion générale.

Dans le chapitre 1, le modèle polycristallinretenu est décrit ; il s'agit du modèle polycristallindit LW (Leffers-Wierzbanowski), retenu pour sa simplicité de mise en œuvre et donc associé à des temps de calcul pas trop lourds, permettant un couplage avec un code d'éléments finis. La loi de comportement utilisée pour le monocristal tient compte du glissement et du maclage (pour le titane uniquement). La capacité de ce modèle à décrire les évolutions microstructurales des alliages métalliques est analysée.

Comme, il est par ailleurs bien connu que plusieurs modèles, plus ou moins rigoureux dans leur formulation permettent de reproduire les textures expérimentales au prix parfois d'un ajustement arbitraire de certains paramètres, la capacité prédictive du modèle retenu est analysée plus en détails dans le chapitre 2, qui s'intéresse à la transition de texture bien connue dans les matériaux cfc à énergie de faute d'empilement variable. En effet, en passant d'un matériau à faible énergie de faute d'empilement comme le laiton par exemple à un matériau à énergie de faute d'empilement plus élevée comme le cuivre, on observe une transition dans les textures de laminage, d'une texture dite « Laiton » à une texture dite « Cuivre », composées d'orientations principales différentes. La capacité du modèle LW à reproduire cette transition en ne faisant varier que les paramètres matériau du modèle est donc examinée en détails.

Le chapitre 3 décrit la procédure d'implémentation du modèle LW dans le code d'éléments finis ABAQUS/Explicit. Cette procédure s'appuie sur l'écriture d'un module de comportement de type VUMAT, décrit en détails. Ce module est ensuite testé par la simulation d'un essai simple de traction, pour lequel les textures simulées ont été comparées à des textures expérimentales.

Le chapitre 4 décrit la partie expérimentale du travail réalisé : les méthodes expérimentales retenues sont tout d'abord décrites (laminage, diffraction X pour les textures crystallographiques, diffraction des électrons rétrodiffusés – EBSD en anglais – dans le microscope électronique à balayage EBSD pour les microstructures). La description des évolutions microstructurales et texturales des deux matériaux déformés à différents taux de déformation et d'asymétrie est ensuite présentée et analysée en détails. On montre notamment que l'asymétrie de laminage permet d'affiner la taille de grain dans la majorité des cas ; cette réduction de la taille de grain est également conservée après le recuit permettant de supprimer l'écrouissage dû au laminage.

Le Chapitre 5 décrit ensuite les simulations numériques réalisées. La comparaison des textures simulées et expérimentales pour différents niveaux d'asymétrie et de taux de déformation est très satisfaisante. L'outil développé permet également de reproduire le fait que la distribution des déformations et des contraintes est plus uniforme au sein du matériau après laminage asymétrique qu'après laminage symétrique standard.

Les principaux résultats de l'étude sont finalement reprécisés dans la conclusion générale.

Summary

In the world of modern technology, there is a demand for construction materials having desired properties. Their design and production is one of the most important tasks of solid state physics and materials science. In recent years there has been a rapid development of metal forming techniques that modify radically the physical properties of materials. Many of them are based on processes of plastic deformation or severe plastic deformation. The main goal of present work is to check and understand the mechanisms of plastic deformation of polycrystalline materials during complex loading. Our study was done for two polycrystalline materials: aluminium 6061 (with f.c.c. structure) and titanium grade 2 (with h.c.p. structure). The asymmetric rolling process was chosen as an example of complex loading processes. Using two experimental techniques: EBSD and X-ray diffraction, the influence of rolling asymmetry on microstructural and mechanical parameters, as well as on crystallographic texture was examined. Many of experimental results were compared with model calculations. The present work is organized as follows.

In Chapter 1 the crystallographic deformation model is described. Two basic mechanism of plastic deformation: crystallographic slip and twinning were considered. These mechanisms were incorporated into polycrystalline deformation model (Leffers-Wierzbanowski model, shortly: LW model). This model is a very efficient and useful tool, which enables the prediction of macroscopic material properties (e.g., texture, stress-strain curves, residual stress, etc.) basing on the micro-structural characteristics (crystallography of slip and twinning systems, hardening law, initial texture, residual stress state, etc.).

In Chapter 2 the well known problem of appearance of two types of f.c.c. rolling textures in metals (copper and brass types) was discussed. It should be noted that in aluminium the copper-type rolling texture is developed. Different crystallographic deformation mechanisms, which explain the copper-brass texture transition (e.g., high and low levels of grain-matrix interaction, two definitions of crystal lattice rotation, activation of twinning or of additional slip systems, etc.) were examined in the frame of LW model. The predicted textures were analyzed and compared quantitatively with experimental data.

In Chapter 3 the implementation of the crystallographic deformation model (LW) into Finite Element Method (FEM) is described. The goal was to create a new efficient tool, which allows to simulate deformation processes with complex geometry. The ABAQUS/Explicit software was used for FEM software. The LW model was implemented into FEM via the user subroutine VUMAT. This routine allows to define a mechanical

constitutive behaviour of material. The new created model (FEM+LW) was checked using the uniaxial tension test. The resulting crystallographic texture was calculated and compared with experimental data.

In Chapter 4 the influence of asymmetric rolling process on microstructure and texture of polycrystalline aluminium and titanium was examined. Experimental procedures, used for a study of resulting material properties, are described in the first part of this chapter. In order to determine crystallographic texture and microstructure evolution in the considered materials the EBSD technique (mainly) and X-Ray diffraction were used. Aluminium samples were rolled to 36% reduction. In the case of titanium two set of sample were examined: low and medium-deformed samples (20% and 40% reductions) and high-deformed and annealed samples (60%, 70% and 80% reductions). Both materials were symmetrically and asymmetrically rolled, with different degrees of rolling asymmetry. The evolution of textures and microstructural parameters (calculated from EBSD maps), is studied and discussed in the last part of this chapter. Finally, important findings concerning textures, grain and microstructure refinement during asymmetric rolling are presented. An interesting result is that the asymmetric rolling leads to a more intensive microstructure refinement of materials and reduction of the mean grain size in many cases (compared to the symmetrical rolling). This latter effect is particularly pronounced in asymmetrically rolled and recrystallized materials.

Finally, in Chapter 5 the asymmetric rolling process was examined using FEM+LW model. This software is a powerful tool, which enables a study of heterogeneous plastic deformation in processes with more complex geometry (asymmetric rolling in our case), taking into account its crystallographic nature. The FEM+LW model was used for the prediction of texture evolution and internal stress distribution in symmetrically and asymmetrically rolled materials, for different degrees of rolling asymmetry. In all the cases the predicted textures were compared with experimental results and, in general, a good agreement was obtained. It was found that asymmetric rolling modifies texture (compared with symmetric rolling) and, moreover, leads to its uniform distribution of the material volume.

Goal of the thesis

In the last years one can observe a dynamical development of forming techniques of metals, which can change radically their physical properties. Many of them are based on processes involving plastic deformation (or severe plastic deformation). The examples of such methods are: Equal Channel Angular Pressing (ECAP), Accumulative Roll Bonding (ARB), Asymmetric Rolling (AR), High Pressure Torsion (HPT), Cyclic Extrusion Compression (CEC) and others. These forming methods can produce fine or ultra fine grain structures, modify crystallographic texture, change the stored energy distribution, modify plastic anisotropy, etc.

Among methods listed above, the asymmetric rolling is distinguished by the facility of implementing it on existing roll mills and by large volumes of the processed material. This forming method is studied in the present thesis. In order to apply this technique in optimal conditions, it is necessary to understand basic mechanisms of plastic deformation on crystal level and, on the other hand, to characterize deformation heterogeneity in a macro scale as well as technological parameters of the forming process. Therefore, the goal of this thesis is to study and explain the above characteristics and parameters. Two polycrystalline metals, having important practical applications, were studied in this work: aluminum (6061 type) and titanium (Grade 2).

We should focus on material modifications caused by asymmetric rolling, but also technological parameters should be studied in aspect of possible optimization of the forming process. It is evident that in the first step of the outlined research plan - an adequate crystal deformation model has to be created and applied to explain basic crystallographic mechanisms of plastic deformation. The second step, is to join such the model with the macroscopic description of deformation; to this aim the crystal model has to be implemented into the Finite Element Method. And the third step is to collect experimental data concerning asymmetrically rolled materials and to compare it with theoretical predictions. The experimental techniques, adapted to this plan are diffraction techniques (EBSD, X-ray diffraction) and mechanical tests (tension stress-strain tests).

In conclusion, the goal of this thesis is:

- to examine the microstructure deformation mechanisms of two studied metals (aluminum and titanium) using crystal based models,

- to implement the crystal deformation model to the Finite Element Method and to use this software for a study of asymmetric rolling,
- to apply the diffraction methods and mechanical tests in order to determine physical properties of asymmetrically rolled materials,
- to compare the theoretical and experimental results and answer the following question: which kind of microstructure, texture and mechanical properties can be obtained using asymmetric rolling ? Are they advantageous for practical applications ?

In the presented thesis these elements are developed.

Chapter 1

1 Crystallographic Deformation Model

1.1 Introduction

In general, models used to study elasto-plastic deformation can be divided into two groups: macroscopic models, e.g., basing on the Finite Element Method (FEM), and micro-macro crystallographic models. In the first case, in classical approach, the material is treated as a continuous medium with specific properties and the crystallographic structure of material is neglected. FEM is appropriate for a deformation study of samples having complex shapes and subjected to various loads. On the other hand, there exist crystallographic deformation models, which take into account the crystalline structure of materials.

In this chapter the Leffers-Wierzbanowski model (LW model) will be presented and discussed. This is micro-macro model, in which crystallographic deformation mechanisms are taken into account. LW model is based on the original formulation due to Leffers [1] [2] and on further developments done by Wierzbanowski et al. [3][4][5][6][7][8][9]. This model is a very efficient tool. It can be used to predict many characteristics and parameters, which are useful for experimental data analysis, e.g.: crystallographic texture, stress-strain curves (hardening curves), residual stress distributions, dislocation density and stored energy distributions, and many others.

1.2 Mechanisms of plastic deformation

Contrary to elastic deformation, which involves reversible displacements of atoms, plastic deformation undergoes by non-reversible atom displacements. There are two basic mechanisms of plastic deformation: crystallographic slip and mechanical twinning. These mechanisms are non-reversible, which means that after release of external forces some permanent deformation stays in a material. In both mechanisms two parts of crystal (or grain) are sheared one with respect to another. The crystallographic slip is schematically presented in Fig.1.1. Neighbouring blocs of crystal are relatively displaced. Let us take example of slip.

The shearing movement occurs on a slip plane *(hkl)* and along a slip direction *[uvw]*. Consequently, one defines a slip system *(hkl)[uvw]* and also a family of equivalent slip systems *{hkl}<uvw>*. The slip phenomenon occurs due to a movement of a huge number of dislocations on a slip plane. Usually slip takes place on crystal planes with the highest density of atoms (due to the lowest energy necessary to shift atoms from one stable position to another). The slip occurs if the shear stress acting in a slip system exceeds some critical value (Schmid law).

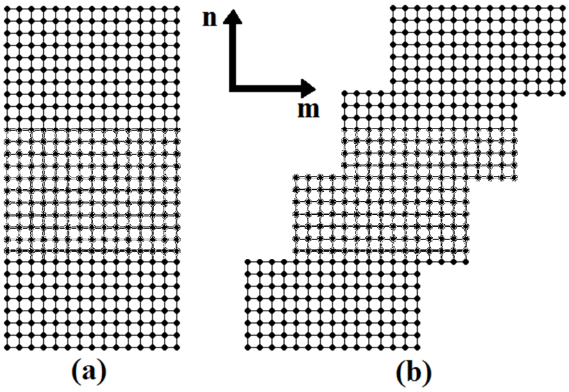

Fig. 1.1. *Slip in a single crystal: a) crystal before slip, b) crystal after slip which occurred on a slip plane (hkl) (with normal* ***n****) and along a slip direction [uvw] (parallel to* ***m*** *vector)*

Mechanical twinning consists of the shearing movements of atomic planes, which lead to the formation of a crystal region with a crystal lattice being a mirror image (with respect to the boundary plane) of the original crystal – Fig. 1.2. This newly created crystal region is called twin. Let us notice that during a twin formation, each subsequent atomic layer is displaced by a shear movement with respect to a neighbouring one. Consequently, the resulting shear deformation γ is high.

It can be shown that at least five independent shear systems (slip and twinning systems) are necessary to produce an imposed deformation. It is also well known that besides deformation also crystal lattice rotation is induced by slip and twinning mechanisms.

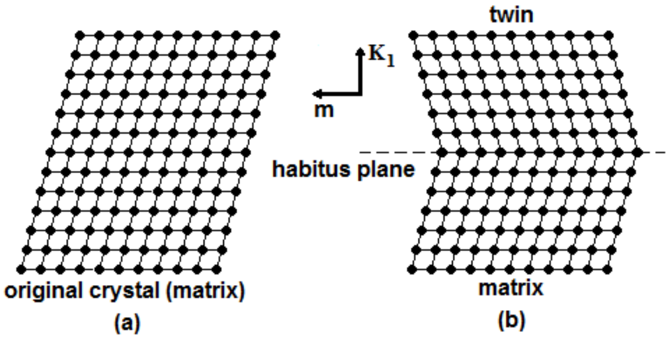

Fig. 1.2. *Twin is created from an original crystal by the shearing movements of consecutive atomic layers along vector* ***m****. The boundary between the matrix and the twin is called habitus plane (with* $\boldsymbol{K_1}$ *normal vector): a) crystal before twinning, b) crystal lattice after twinning.*

As stated above, slip and twinning are two basic crystallographic mechanisms of plastic deformation. Mechanical twinning appears in h.c.p. and in some f.c.c. metals, especially if they are deformed with high strain rates and at low temperatures. However, in f.c.c. metals deformed at room temperature, the crystallographic slip is strongly dominating mechanism.

1.3 Description of the crystallographic model

In order to create a crystallographic deformation model one has to consider the elastic and plastic mechanisms of strain. The aim of such a model is a correct description of the processes occurring during deformation of polycrystalline materials. The elastic deformation is well described by the Hook's law in tensor form. Also the mechanisms of plastic deformation like slip and twinning are well defined and characterized. On the other hand, we dispose of numerical and experimental tools for the verification of the model predictions. They are, e.g., distribution functions of: orientations (texture), misorientations, grain sizes or grain boundary orientations. These functions can be determined by X-ray and neutron diffraction and by Electron Back Scatter Diffraction (EBSD) technique. Also the results of mechanical tests (like tensile, shear or torsion tests) serve for checking the model predictions. Using the above elements and techniques, one can formulate and test deformation models and use them for a study of material characteristics.

The basic question, which has to be answered in any model, is: what is the relation between macroscopic variables of the sample (Σ_{ij}, E_{ij}) and analogical local ones (σ_{ij}, ε_{ij}), characterizing grains (Fig. 1.3). Unfortunately, it is not possible to solve this problem in a general case. It is the reason why we use models.

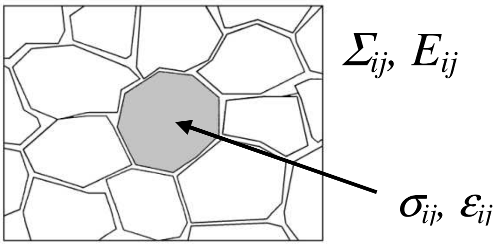

Fig. 1.3. *Macroscopic load Σ_{ij} is applied to a material, while a local stress σ_{ij} appears on a grain level. The sample deformation is E_{ij} and a grain deformation is ε_{ij}.*

It was shown by Hill [10] that a general relation between local and global variables can be written in the form:

$$\dot{\sigma}_{ij} = \dot{\Sigma}_{ij} + L_{ijkl}(\dot{E}_{kl} - \dot{\varepsilon}_{kl}) \tag{1.1}$$

where $\dot{\sigma}_{ij}$, $\dot{\varepsilon}_{ij}$ are local stress and strain rates, $\dot{\Sigma}_{ij}$, $\dot{E}_{ij}$ are their global equivalents, L_{ijkl} is the interaction tensor and the convention of summation on the repeated *lower* indices is applied (it is used in the further text of the present work).

A strict calculation of L_{ijkl} tensor is impossible in a general case, hence some simplifying assumptions have to be done. A considerable progress was done by the self consistent models and many interesting results were found using them[11][12][13][14][15].

Nevertheless, it was found that the assumption of isotropic grain-matrix interaction leads to surprisingly good predictions of many material properties. In such the case the L_{ijkl} tensor is replaced by a scalar L. Moreover, in the cases of practical importance, it can be assumed that the plastic strain rate term$(\dot{E}^p_{ij} - \dot{\varepsilon}^p_{ij})$is much larger than the elastic one $(\dot{E}^e_{ij} - \dot{\varepsilon}^e_{ij})$. Accordingly, Eq.1.1 can be simplified to the following form:

$$\dot{\sigma}_{ij} = \dot{\Sigma}_{ij} + L\,(\dot{E}^p_{ij} - \dot{\varepsilon}^p_{ij}) \tag{1.2}$$

or after integration (assuming that initial stresses and strains are zero) [6]:

$$\sigma_{ij} = \Sigma_{ij} + L(E^p_{ij} - \varepsilon^p_{ij}) \tag{1.3}$$

Some of known models can be reduced to Eq. 1.2 if L takes appropriate values:

- **a)** $L=0$ leads to the Sachs model [16]; it is assumed that no interactions between grains appear and consequently a homogeneous stress state results: $\sigma_{ij} = \Sigma_{ij}$,
- **b)** $L \to \infty$ leads to the Taylor model [17]; the basic assumption of this model is a homogeneous plastic deformation in the sample: $\varepsilon_{ij}^{p} = E_{ij}^{p}$;
- **c)** $L = \frac{2(7-5\nu)}{15(1-\nu)} G$ leads to Kröner model (where ν is the Poisson coefficient and G is the shear modulus; $L \cong G$ for typical value of $\nu \cong 0.3$). This model is derived under the assumption of a purely elastic interaction between a grain and the matrix [18],
- **d)** $L=2G$ leads to Lin model [19]; its basic assumption is: $E_{ij}^{e} + E_{ij}^{p} = \varepsilon_{ij}^{e} + \varepsilon_{ij}^{p}$,
- **e)** $L=\alpha' G$ leads to a compromise description, very close to a real interaction. This is isotropic model with elasto-plastic interaction [11]. The α' parameter is called the elasto-plastic accommodation parameter and it describes a partial shape accommodation between grains, caused by some additional local slip. Values of α' from the [0.1 – 0.001] range lead to a good agreement with experimental data. This kind of interaction was used by M. Berveiller et al. [11] and in the Leffers-Wierzbanowski model (LW model)[6].

The interaction law described by Eq. 1.3 determines the local stress σ_{ij} as a superposition of the applied external stress Σ_{ij} and the interaction term $L(E_{ij}^{p} - \varepsilon_{ij}^{p})$, which acts in order to minimize the difference between a grain shape and that of the sample.

1.4 Basic quantities in deformation models

1.4.1 Crystallographic slip

Slip is the elementary mechanism of plastic deformation. The shearing movement occurs on a crystallographic slip plane *(hkl)* (characterized by its normal unit vector ***n***) and along a slip direction vector *[uvw]* (characterized by ***m*** unit vector). Consequently one defines *(hkl)[uvw]* slip system, which can also be shortly denoted as (***n***, ***m***). The slip geometry is schematically presented in Fig.1.4, where also the slip shear strain increment $\delta\gamma$ is defined. It is useful to introduce the reference frame (g) connected with the slip system:

$x_1^g = \boldsymbol{m}$ and $x_3^g = \boldsymbol{n}$ (Fig. 1.4). The resolved shear stress, decisive for a slip system activation, is easily expressed in this coordinates system: $\sigma_{(hkl)[uvw]} = \sigma_{13}^g$. In a similar way, the glide shear increment $\delta\gamma$ produced by a single slip has only one component of the *plastic displacement gradient*: $\delta e_{13}^{p\,(g)} = \delta\gamma$. (The same tensor expressed in the sample reference frame is: $\delta e_{ij}^p = m_i n_j\,\delta\gamma$, where m_i and n_j are components of $\boldsymbol{m}$ and $\boldsymbol{n}$).

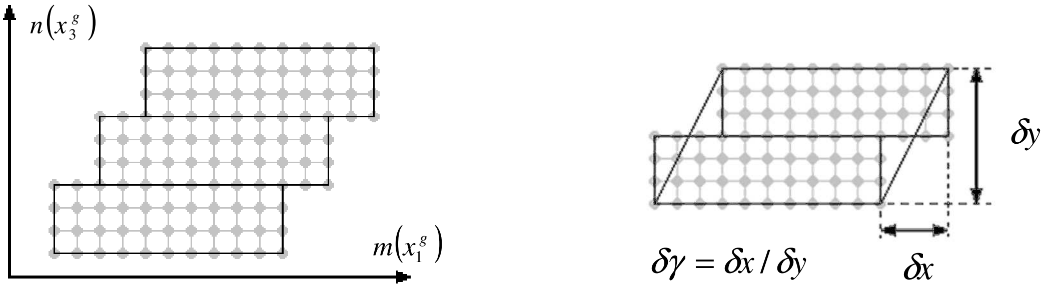

***Fig. 1.4**. Displacement of the material during a single slip event. The first axis of the **g** system is defined by **m** vector and the third axis – by **n** vector (left). Definition of a glide shear increment $\delta\gamma$ caused by a single slip (right).*

If the resolved shear stress in a considered slip system $\sigma_{(hkl)[uvw]} = \sigma_{13}{}^{(g)}$ reaches its critical value τ_c – the slip system becomes active (Schmid law):

$$\sigma_{(hkl)[uvw]} = \tau_c \tag{1.4}$$

The resolved shear stress $\sigma_{(hkl)[uvw]} = \sigma_{13}{}^{(g)}$ on the slip system (***n, m***) is calculated as:

$$\sigma_{(hkl)[uvw]} = m_i n_j \sigma_{ij} \tag{1.5}$$

where σ_{ij} is the local stress tensor. Every elementary act of slip (with $\delta\gamma$ shear) produces strain $\delta\varepsilon_{ij}^p$ and rotation $\delta\omega_{ij}^p$ of a grain, which are calculated as symmetric and anti-symmetric parts of $\delta e_{ij}^p = m_i n_j\,\delta\gamma$:

$$\delta\varepsilon_{ij}^p = \frac{1}{2}(m_i n_j + m_j n_i)\,\delta\gamma \tag{1.6}$$

$$\delta\omega_{ij}^p = \frac{1}{2}(m_i n_j - m_j n_i)\,\delta\gamma \tag{1.7}$$

After each elementary act of slip the grain is rotated (as a rigid body) of $\delta\omega_{ij}^p$ - Fig. 1.5, but the lattice itself does not change its orientation (cf. Figs. 1.5 *a* and 1.5 *b*). If there was not interaction between a sample and a deforming device (or between a grain and the matrix) – *crystal lattice orientation* would not change. However, in general a grain does not rotate as a rigid body, because some constraints are imposed by the neighbouring material and by the deformation device. As a consequence, a compensating rotation occurs ($\delta\omega_{ij}^{latt}$) and it changes the grain lattice orientation.

In the present work two definitions of lattice rotation will be considered. The *classical definition* (*CL*), is based on the assumption that a rigid body rotation has to be compensated by the lattice rotation[12] **[A4][A5][A8]:**

$$\delta\omega_{ij}^{latt} = -\delta\omega_{ij}^{p} \tag{1.8}$$

The other approach is based on the assumption that selected sample and grain planes and/or directions preserve a constant orientation with respect to the sample reference frame (defined by the sample deformation geometry)[1][20] **[A4][A5][A6][A8].** This approach, named by the present author *preservation* (*PR*) condition, was successfully used in modelling the plane strain and axially symmetric deformations (e.g.,[1][5][21]). For example, if we consider the tensile test of a single crystal (Fig. 1.5), the direction defined by a tensile force has to be preserved. This condition imposes a compensating rotation of a crystal, $\Delta\omega_{ij}^{latt}$, which involves a corresponding lattice rotation (cf. Figs.1.5 *b* and *c*). The two rotation definitions are described in Chapter 2. They were also discussed in [20] **[A6].**

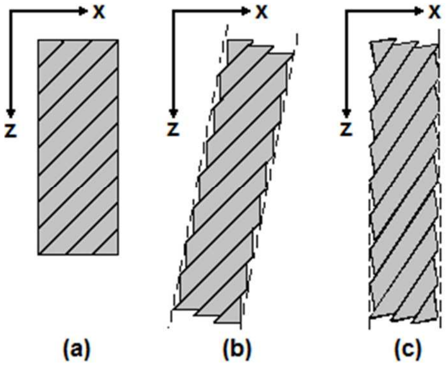

Fig. 1.5. *Tensile test of a crystal along z direction: a) before slip, b) after slip, c) after fulfilment of the condition that a string of material initially parallel to z axis has to preserve this orientation (z axis is parallel to the applied tensile force).*

After each elementary slip event (with a small value of the shear strain $\delta\gamma$), all basic quantities are recalculated (crystal orientation, grain strain and stress, critical stresses for slip systems ...). The resulting plastic strain and lattice rotation of a grain, in a given calculation increment, are superposed during consecutive glides on the most loaded slip systems ($\delta\gamma^s = \delta\gamma$ in our calculations):

$$\Delta\varepsilon_{ij}^{p} = \sum_s \left[\frac{1}{2}\left(m_i^s n_j^s + m_j^s n_i^s \right) \delta\gamma^s \right] \tag{1.9}$$

$$\Delta\omega_{ij}^{latt} = -\sum_s \left[\frac{1}{2}\left(m_i^s n_j^s - m_j^s n_i^s \right) \delta\gamma^s \right] \tag{1.10}$$

where summation is done on consecutive slip events (example of *CL* rotation definition was used). The accumulated lattice rotations of grains lead to a final crystallographic texture.

The plastic strain increment of the sample is the arithmetic average of strain increments of all grains:

$$\Delta E_{ij}^{p} = \sum_n \Delta\varepsilon_{ij}^{p(n)} f^n \tag{1.11}$$

where f^n is the volume fraction of the *n-th* grain.

1.4.2 Hardening of slip systems

Slip systems are hardened during deformation, which is visible in the slope of the stress-strain curves in the plastic range. The hardening is caused by interactions between dislocations, which are intensively multiplied during deformation. Dislocations are necessary for a progress of plastic strain, but being in a huge amount they also block each other. This increases the critical shear stress for slip. The hardening of slip systems is described as:

$$\dot{\tau}_c^r = \sum_s H^{rs} \dot{\gamma}^s \tag{1.12}$$

where: $\dot{\tau}_c^r$ is the rate of the critical shear stress for the *r-th* slip system (the same initial values of critical shear stresses, τ_o, are attributed to slip systems of a given family), $\dot{\gamma}^s$ is the rate of the plastic shear on the *s*-th system and H^{rs} is the work-hardening matrix [22] defined as:

$$H^{rs} = q^{rs} h_o \tag{1.13}$$

In this formula h_o is the amplitude of the hardening matrix and q^{rs} describes its structure; in the simplest approach:

$$q^{rs} = \begin{cases} 1 & if\ r=s \\ d & \text{- } otherwise \end{cases} \tag{1.14}$$

The isotropic hardening occurs for *d=1*; otherwise we deal with anisotropic hardening (e.g., for *d=1.3*). The amplitude of the work hardening matrix, h_0, is assumed constant in the case linear hardening law. In the non-linear case the saturating hardening law was used:

$$H^{rs} = q^{rs} h_{sat} \left(1 - \frac{\tau_c^r}{\tau_{sat}} \right)^a \tag{1.15}$$

where τ_{sat} is the saturation value of the critical shear stress (τ_{sat} has the same value for all slip systems belonging to a given family) and h_{sat} determines amplitude of the hardening matrix. The parameters of hardening law (d, h_{sat}, τ_{sat}, τ_o) can be approximately determined by fitting predicted and experimental stress-strain curves.

1.4.3 Twinning mechanism

Another crystallographic deformation mechanism, besides of slip, is twinning. During twinning a part of crystal or its whole volume is transformed into a twin, which has a characteristic lattice orientation with respect to the matrix crystal. Twinning is an important deformation mechanisms in h.c.p. metals. The possible role of volume twinning in deformation of f.c.c. metals (and derived textures) was discussed by many authors (e.g.,[23][24][25][26][27]). Twins of the first kind were considered in the present work and, consequently, the habitus plane (characterized by the normal unit vector $\mathbf{K_1}$) and twinning direction $\boldsymbol{\eta_1}$ were used to identify a twin system. The following orientation relation between a twin and the matrix is defined[28]:

$$\begin{bmatrix} v_1 \\ v_2 \\ v_3 \end{bmatrix} = \begin{bmatrix} (2\cdot t_1^2 - 1) & 2\cdot t_1 \cdot t_2 & 2\cdot t_1 \cdot t_3 \\ 2\cdot t_2 \cdot t_1 & (2\cdot t_2^2 - 1) & 2\cdot t_2 \cdot t_3 \\ 2\cdot t_3 \cdot t_1 & 2\cdot t_3 \cdot t_2 & (2\cdot t_3^2 - 1) \end{bmatrix} \begin{bmatrix} p_1 \\ p_2 \\ p_3 \end{bmatrix} \tag{1.16}$$

where v_i and p_i are components of a given vector expressed in the twin and the crystal reference frames, respectively, and t_i are components of the $\boldsymbol{K_1}$ vector, expressed in the crystal reference frame. The geometry of twinning is shown in Fig.1.6.

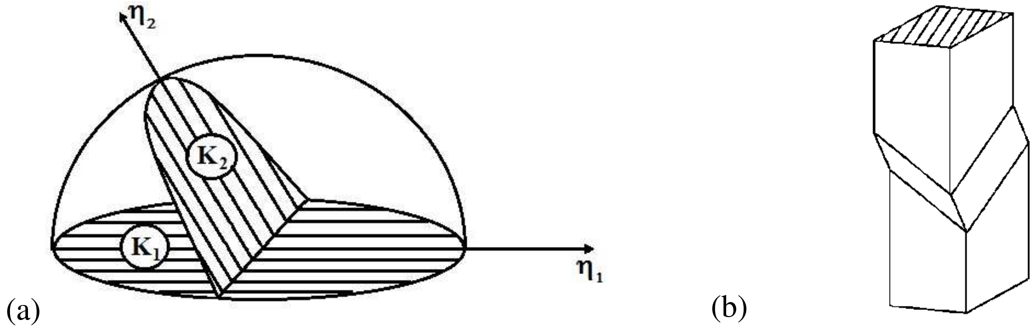

Fig. 1.6. Geometry of mechanical twinning: a) habitus plane $\boldsymbol{K_1}$ *and twinning direction* $\boldsymbol{\eta_1}$ *(twins of the first kind) ; the second undistorted plane* $\boldsymbol{K_2}$ *and direction* $\boldsymbol{\eta_2}$ *(twins of the second kind)*[28], *b) morphological change of a crystal shape after twinning.*

The twinning mechanism has been incorporated into the model according to the approach proposed by Tome et al.[26]. In each deformation step the increment of the twinned volume fraction in the *n*-th grain associated with the twinning system β is:

$$\delta g^{n,\beta} = \frac{\delta\gamma^{n,\beta}}{\gamma^{\beta}} \tag{1.17}$$

where $\delta\gamma^{n,\beta}$ is the shear increment realized on the twinning system β in the *n-th* grain and γ^{β} is the characteristic total shear of the twin (constant). After a deformation increment (containing a number of elementary deformation steps), the accumulated twinned fraction due to the twinning system β is:

$$g^{n,\beta} = \sum_{steps} \delta g^{n,\beta} \tag{1.18}$$

A summation over all twinning systems and all grains gives the 'real' volume fractions F_R of twins in the polycrystalline material:

$$F_R = \sum_n f^n \sum_\beta g^{n,\beta} \tag{1.19}$$

where f^n is the volume fraction of the *n-th* grain with respect to the sample volume.

Next, the 'effective' twinned volume of the sample is calculated; for this purpose the following sum over grains that have already changed their orientation due to twinning is calculated:

$$F_E = \sum_m f^m \tag{1.20}$$

Using the above factors we define a threshold value:

$$F_T = A_1 + A_2 \frac{F_E}{F_R} \tag{1.21}$$

In each deformation step the twinned volume fraction due to each system β in the *n-th* grain, i.e., $g^{n,\beta}$, is compared with the threshold value F_T. If $g^{n,\beta} > F_T$, then the orientation of the grain is transformed to the orientation of the twin. This reorientation occurs on the twinning system with the highest activity throughout the deformation process. Such the procedure is self controlling and both F_E and F_T tend to remain approximately equal during deformation. For example, if F_E grows faster than F_R, the threshold F_T rises and the number of reoriented grains slows down. The value of $A_1=A_2=0.25$ were used in calculations, as proposed in[26].

The method of Tome is simplified, because the final twin reorientation applies to the whole grain volume and is based on predominant twinning system. The advantage of this approach is that one avoids grain multiplications, and consequently avoids an increase of computer time and memory. This approach is also recommended for 'heavy duty' calculations (for example, if one implements the deformation model into FEM).

1.5 Calculation mode using LW model

The calculations are carried out incrementally in LW model. One calculation increment corresponds to the increase of external load, i.e., of the amplitude of applied stress tensor. During each increment all grains are deformed (on slip systems and twinning systems) till a moment when no more slip and twinning systems are active. Then, a consecutive increment of the applied stress tensor amplitude is done, and so on. The logical diagram of LW model is shown in Fig. 1.7.

In the beginning of calculations the initial parameters are read and grains are created (initialized). The starting orientation distribution of grains can be generated at random or according to a given initial texture. In the first increment of calculations the external stress tensor amplitude Σ has a value close to that necessary for activation of the best oriented slip systems: $\Sigma = \Sigma^0$. Next, the amplitude of the applied stress tensor is increased of $\Delta\Sigma$:

$$\Sigma = \Sigma^0 + (k-1)\Delta\Sigma \tag{1.22}$$

where *k* numbers the increments.

The applied stress tensor Σ_{ij} is defined as: $\Sigma_{ij} = \Sigma \cdot \Sigma_{ij}^{def}$, where Σ is its amplitude and Σ_{ij}^{def} is the 'shape tensor' defined for a given type of deformation. For example, in the case of tensile test deformation along z axis, the applied stress tensor, Σ_{ij}, is:

$$\Sigma_{ij} = \Sigma \cdot \Sigma_{ij}^{def} = \Sigma \begin{bmatrix} 0 & 0 & 0 \\ 0 & 0 & 0 \\ 0 & 0 & 1 \end{bmatrix} \tag{1.23}$$

Let us describe now which operations are done during one deformation increment.

The applied stress tensor is transformed to slip system reference frame of the first grain (the number of slip system depends on crystal structure, e.g., there are 12 basic slip systems in f.c.c. metals). The local stress in this grain is calculated according to Eq. 1.3. It is checked next, whether the shear stress on each slip systems reaches the critical value $\sigma_{(hkl)[uvw]} = \tau_c$ (Schmid law). The most loaded slip system (and fulfilling the Schmid law) is selected as active one in a given moment and the glide shear strain $\delta\gamma$ is imposed on it. After this elementary slip event (with a small $\delta\gamma$ value) the grain deformation and lattice orientation are updated (the increments $\delta\varepsilon_{ij}^{p}$ and $\delta\omega_{ij}^{latt}$ are calculated). The local stress is also updated according to Eq.1.3. Next, a new active slip system is selected, and so on. Hence, a series of consecutive slips on different systems occurs in a grain, as long as the Schmid law is fulfilled. However, with progressing deformation, the critical stress values are increasing according to the hardening law. If we reach the situation when no more slip (and twinning) systems are active in a given grain, we repeat the same calculations for the next grain, and so on, until the last grain. At the end of the calculation increment we determine the sample strain increment ΔE_{ij}^{p} (Eq. 1.11) and we pass to the next load increment (increasing the amplitude of applied external stress of $\Delta\Sigma$). In the following increments we repeat the same procedure as that described above. The calculations are continued until the final sample deformation is reached.

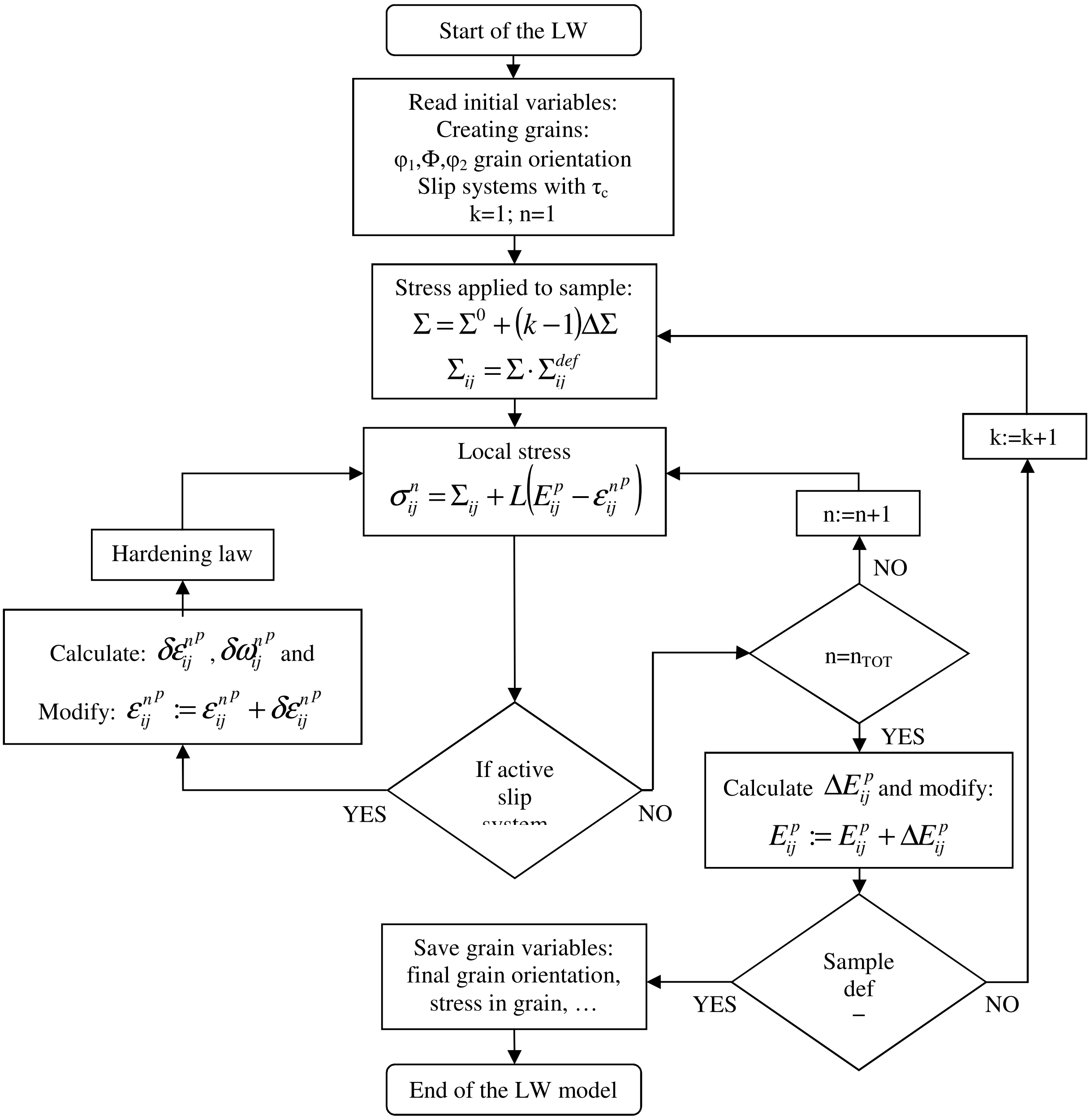

Fig. 1.7. *Flowchart of LW model.*

1.6 Calculations for hexagonal crystal structure

In the present work the deformation of metals with cubic (f.c.c.) and hexagonal (h.c.p.) crystal structures is considered. In the case of cubic crystal structure the choice of orthogonal crystal reference frame is obvious - it is defined by three translation vectors of the elementary cell.

In the case of h.c.p. structure the situation is more difficult. The elementary cell is defined by two vectors of equal length, $\boldsymbol{a_1}$ and $\boldsymbol{a_2}$, with the angle of 120^0 between them, and by the third vector **c** perpendicular to the above vectors (Fig. 1.8a). Generally, the Bravais-Miller indices of planes and directions are expressed in this non-orthogonal reference frame and are defined by four numbers: (*hkil)* and *[prst]*, respectively. These numbers correspond to four translation vectors (a_1, a_2, a_3, and *c*), shown in Fig.1.8a. It can be shown that the indices '*i*' and '*s*' are redundant and:

$$i = -(h+k) \qquad (1.24)$$
$$s = -(p+r)$$

Therefore, in the present calculations the artificial orthogonal reference frame was used to represent a crystallographic cell. Two unit vectors of the new coordinates system ($\boldsymbol{X_2}$ and $\boldsymbol{X_3}$) are parallel to the vectors of the elementary cell ($\boldsymbol{a_2}$ and ***c***) and $\boldsymbol{X_1}$ is perpendicular to them, as shown in Fig. 1.8b.

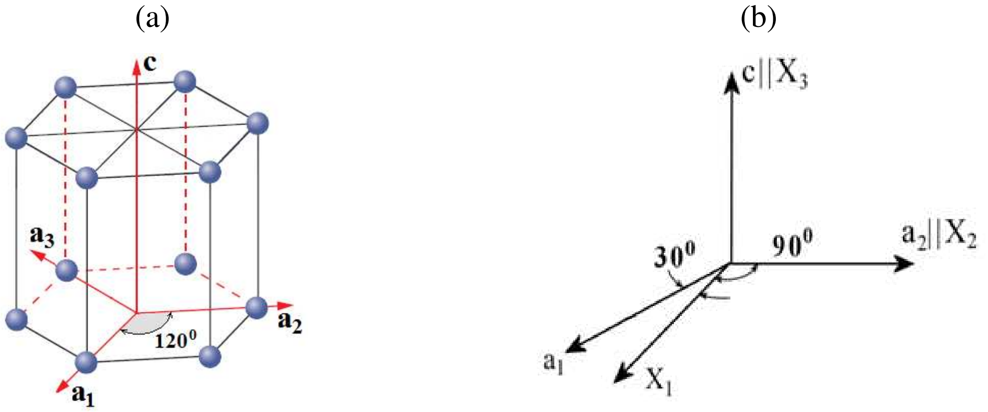

Fig. 1.8. *(a) Hexagonal elementary cell defined by {$\boldsymbol{a_1}$, $\boldsymbol{a_2}$, $\boldsymbol{a_3}$, **c**} and (b) orthogonal reference frame represented by { $\boldsymbol{X_1}$, $\boldsymbol{X_2}$, $\boldsymbol{X_3}$}.*

In order to express crystal planes and directions in this orthogonal reference frame, the following transformation, derived in[3], were used:

for plane:
$$(hkil) \rightarrow (h'k'l') = \left(\frac{2h+k}{\sqrt{3}}, k, l, \frac{a}{c} \right)$$

for direction:
$$[prst] \rightarrow [u'v'w'] = \left[\frac{\sqrt{3}}{2}(p-s), -\frac{3}{2}(p+s), t\frac{c}{a} \right] \qquad (1.25)$$

where: *h'k'l'* and *u'v'w'* are new indices of planes and direction in the orthogonal reference frame defined above; *c* and *a* – are lattice parameters of hexagonal cell. Using this transformation, the model calculations for hexagonal structure are done similarly like for the cubic crystal structure.

Chapter 2

2 Problem of crystal lattice rotation and rolling texture transition in f.c.c. metals

2.1 Introduction

The well known problem of the appearance of two types of rolling textures of f.c.c. polycrystalline metals is studied in this chapter. One of two materials studied in this thesis is polycrystalline aluminium, in which the copper-type rolling texture develops. It is the reason why we tried to explain which specific mechanisms are decisive for the formation of one or another type of f.c.c. rolling texture.

The existing theories and assumptions, which explain the copper - brass texture transition were examined in the frame of LW deformation model. Different combinations of slip and twinning systems, low and high levels of grain-matrix interaction as well as two definitions of crystal lattice rotation were taken. The predicted textures were analyzed and quantitatively compared with experimental data. The formation of the copper-type texture can be easily explained taking into account a high level of interaction and classical {110}<111> slip. The problem arises with explaining the brass-type texture formation. After analysis of theoretical results and their comparison with experimental data, the most convincing explanation of the copper-brass texture transition was proposed.

2.2 Historical background

Already in 1929 Göhler and Sachs [29] argued that there are two different types of rolling texture in f.c.c. metals and alloys, and scattered evidence supporting this idea appeared in the following decades. In 1952 it was formally confirmed by Hu et al. [30] with quantitative pole figures: Pure f.c.c. metals except silver develop one type of rolling texture, now referred to as the copper-type texture, whereas silver and Cu-Zn alloys develop another type of rolling texture, now referred to as the brass-type texture. In the nineteen sixties the empirical conditions for the development of the two types of texture were established as recently recapitulated in [23]: The development of the copper-type texture is favoured by high stacking fault energy, high rolling temperature and low strain rate while the development of the brass-type texture is favoured by the opposite set of conditions.

The establishment of the empirical conditions for the texture development in the nineteen sixties triggered a number of theories for the development of the two types of texture. They were all simple 1-point models, i.e. they do not consider the interaction between the specific grains and their specific neighbours. Later 2-point models have appeared which consider the interaction between two specific neighbouring grains, e.g. [31], or the interaction between two specific families of bands into which the single grains may split up, e.g. [32][33]. The ultimate models for the plastic deformation of polycrystals – and hence for the formation of deformation texture – are n-site models, full-field models, which consider the multiple interaction between the specific grains, e.g, [34][35]. By now there is general agreement that the formation of the copper-type texture can be simulated/modelled by {111}<110> slip within various schemes ranging from simple 1-point model to full-field models. As described in [23] there is not a corresponding general agreement about the formation of the brass-type texture. It may be simulated by a combination of {111}<110> slip and a volume effect of deformation twinning or by {111}<110> slip only with a special pattern of slip and lattice rotation.

The discussions of the various schemes for the formation of the two types of texture have been based on qualitative/semi-quantitative comparisons of the simulated/modelled textures with the experimental textures, on theoretical considerations and on microstructural observations. In the present chapter we are going to do strictly quantitative comparisons of the textures simulated/modelled for the various schemes (with continuous variation from the Sachs version to the Taylor version) and the experimental textures with a procedure based on linear regression, developed by Tarasiuk and Wierzbanowski [36]. And we are going to do the comparisons at a reduction of 60% whereas comparisons between simulated and experimental textures have traditionally been made at substantially higher reductions. Our justification for this is that the formation of the brass-type texture at higher reductions includes processes which are not very well understood: the intermediate formation of a texture component with {111} parallel to the rolling plane and the formation of shear bands, e.g. [23][37]. This procedure requires that we do all the simulations with the software available to us which sets a practical limit to the level of complication of the models that we can include. The calculations were done with our 1-site LW model.

In agreement with the earlier description of the mechanisms leading to the respective types of texture, our emphasis is on the {111}<110> slip and on the {111}<110> slip together with a volume effect of deformation twinning. However, for the sake of completeness we also consider the early suggestions of added non-octahedral slip [38] and slip by partials [39].

2.3 Mechanisms leading to copper-brass texture transition

The mechanisms which can produce a transition between the two types of f.c.c. rolling textures are presented below. Some of them are obvious, others are more hypothetical. Therefore, the probability of their occurrence based on a comparison with experimental results will be evaluated. A similarity of predicted and measured textures is estimated using the correlation factor R. $R = 1$ means that the two textures are identical, and decreasing R values reflect decreasing degree of similarity. R will be calculated comparing a pair of Orientation Distribution Functions (ODFs) – with a linear-regression procedure developed in [36]. In the present work was assumed that two textures are classified as similar if $R \geq 0.8$ and as different if $R < 0.8$ For $R \sim 0.9$ (or higher) there is a really good agreement. Also, the fractions of main texture component were estimated.

There are two main variables, which decide on a type of texture, are: the level of grain-matrix interaction L (cf. Eq.1.2 and Eq.1.3) and the type of lattice rotation definition (described in section 2.5.1). Their effects are coupled and, therefore, they have to be discussed together.

The following crystallographic mechanisms were considered and examined in the present work (cf.[40]):

- the case of {111}<110> slip,
- dissociation of <110> perfect dislocations into <112> partials on the {111} planes, leading to {111}<112> slip (in addition to {111}<110> slip),
- {111}<112> deformation twinning in addition to {110}<110> slip,
- possible activity of non-octahedral slip systems: {110}<110> and {100}<110>,
- {111}<110> slip with cross-slip.

2.4 Initial model parameters

The LW model of polycrystalline plastic deformation, described in Chapter 1, was used to study f.c.c. rolling textures. A model sample containing 5000 grains of the same volumes, with an initial random orientation distribution, was deformed until the rolling reduction of 60%. The linear hardening was used; it is characterized by the parameters: h_0, τ_0, d (cf. Eqs. 1.12 - 1.14). Typical values of these parameters for f.c.c. materials were used - Table 2.1. Strong and weak levels of grain-matrix interaction (L) were considered for different combination of slip (and twinning) systems. The experimentally verified range of variation of L for polycrystalline metals is generally contained between $0.001 \cdot G$ and $0.1 \cdot G$, where G is the shear modulus. In the case of copper this gives values of L between 80 MPa and 8000 MPa, while in the case of brass this range is approximately between 30 MPa and 3000 MPa. Therefore, the calculations were done for the following values of L: 10, 30, 100, 300, 1000, 3000 and 5000 MPa.

The textures were calculated using two different lattice rotation definitions, which are discussed in the next section.

***Table 2.1**. The hardening parameters used in calculations.*

τ_0 (MPa)	h_0 (MPa)	d
100	60	1.0

2.5 Results for f.c.c. rolling textures predictions

2.5.1 {111}<110> slip and two definitions of lattice rotation

Two different definitions of lattice rotation and various levels of the interaction parameter L are considered in this section. The resulting textures, predicted with {111}<110> slip, are discussed and compared with experimental data.

Classical definition (CL) of lattice rotation

Let us assume that the total sample rotation as well as the resulting rotation of each grain is zero. Hence, a compensating rotation of a grain lattice ($\delta\omega_{ij}^{latt(CL)}$) has to be added in order to compensate the plastic rotation (rigid body rotation):

$$\delta\omega_{ij}^{latt(CL)} = -\delta\omega_{ij}^{p} = -\frac{1}{2}(m_i n_j - m_j n_i)\,\delta\gamma \tag{2.1}$$

CL is the classical lattice-rotation scheme used in solid mechanics as described in textbooks like [41].

Lattice rotation based on Preservation Condition (PR)

The possibility of another definition of crystal lattice rotation, based on the orientation preservation of selected sample directions and planes, was discussed for the first time by Hosford [20]. Developing this idea Leffers and Lebensohn [42][43] and Wierzbanowski et al. **[A3][A4][A5][A8]** showed that in the case of rolling such approach can give new and interesting results. If the orientations of the specified sample directions and/or planes are assumed to be preserved in the sample reference frame, then the specified shear components (*kl*) of the plastic displacement gradient tensor have to be zero:

$$\delta e_{kl} = 0 \tag{2.2}$$

This involves an auxiliary rotation (lattice rotation), which has to be added to compensate these components:

$$\delta\omega_{kl}^{latt\,(PR)} = -\,\delta e_{kl}^{p} = -\,m_k n_l\,\delta\gamma \tag{2.3}$$

We denote this lattice rotation definition, based on the preservation condition, as *PR*.

During rolling process grains being initially equiaxed become flattened parallel to the rolling plane and elongated along the rolling direction. Hence, a string of material being initially parallel to the rolling direction (x_1) preserves its orientation in the laboratory reference frame. Similarly, a plate of material being initially parallel to the rolling plane (x_1 x_2) – stays parallel to this plane. Consequently, δe_{31}^{p} , δe_{21}^{p} and δe_{32}^{p} components of the displacement gradient tensor have to be compensated by the lattice rotation components:

$$\begin{aligned}\delta\omega_{21}^{latt(PR)} &= -\delta e_{21}^{p} = -m_2 n_1 \delta\gamma \\ \delta\omega_{31}^{latt(PR)} &= -\delta e_{31}^{p} = -m_3 n_1 \delta\gamma \\ \delta\omega_{32}^{latt(PR)} &= -\delta e_{32}^{p} = -m_3 n_2 \delta\gamma\end{aligned} \qquad (2.4)$$

with: $\delta\omega_{ij}^{latt(PR)} = -\delta\omega_{ji}^{latt(PR)}$

The difference between two definitions of rotation is shown in Fig. 2.1, using a simple example. A crystal in the form of a square plate is sheared on the marked slip system. In the case of *PR* definition, it is assumed that a string of material primarily parallel to x_1 sample axis, has to preserve its orientation in the sample coordinates reference frame. The case of *CL* rotation is also shown. It is visible that two definitions lead to different lattice rotations.

Let us also note that the difference between *CL* and *PR* lattice rotations ($\Delta\delta\omega_{31}^{latt}$) in Fig.1 is: $\Delta\delta\omega_{31}^{latt} = \delta\omega_{31}^{latt(CL)} - \delta\omega_{31}^{latt(PR)} = \delta\varepsilon_{31}$. If the same preservation conditions were defined with respect to two other axes (x_2 and x_3), one would obtain:

$$\Delta\delta\omega_{21}^{latt} = \delta\varepsilon_{21}, \quad \Delta\delta\omega_{31}^{latt} = \delta\varepsilon_{31}, \quad \Delta\delta\omega_{32}^{latt} = \delta\varepsilon_{32} \qquad (2.5)$$

Hence, if the shear components of plastic deformation are zero ($\delta\varepsilon_{21}^{p} = \delta\varepsilon_{31}^{p} = \delta\varepsilon_{32}^{p} = 0$), the both definitions lead to the same lattice rotations (cf. [A4]) and consequently to the same textures. Such the condition is verified in the case of a deformation with orthorhombic sample symmetry, e.g., in channel die test and approximately during rolling. In modelling of this type of deformation, i.e., lack of shear components, a high level of interaction, *L*, has to be applied (more precisely L_{21}, L_{31} and L_{32} components of *L* should have high values).

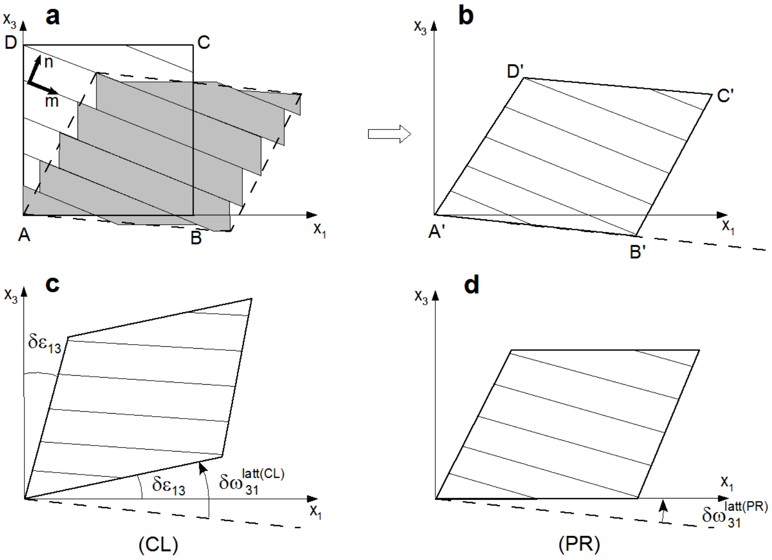

Fig. 2.1*. Deformation of a crystal in a form of a square plate ABCD (with edges parallel to the laboratory reference frame): a) shear occurred on the slip system (****n****,* ***m****), b) shape and position of the grain (A'B'C'D') after slip only, c) position after slip and CL lattice rotation, d) position after slip and PR lattice rotation (a string of initial material parallel to* x_1 *preserved its orientation).*

The predicted ODFs obtained with L=10 MPa (weak interactions) and L=1000 MPa (high interactions) for both rotation definitions are compared with experimental rolling textures of copper and α-brass and in Figs. 2.2 and 2.3. For each predicted ODF we calculated a correlation factor estimating its similarity to experimental ODF of α-brass (R_B) and of copper (R_C).

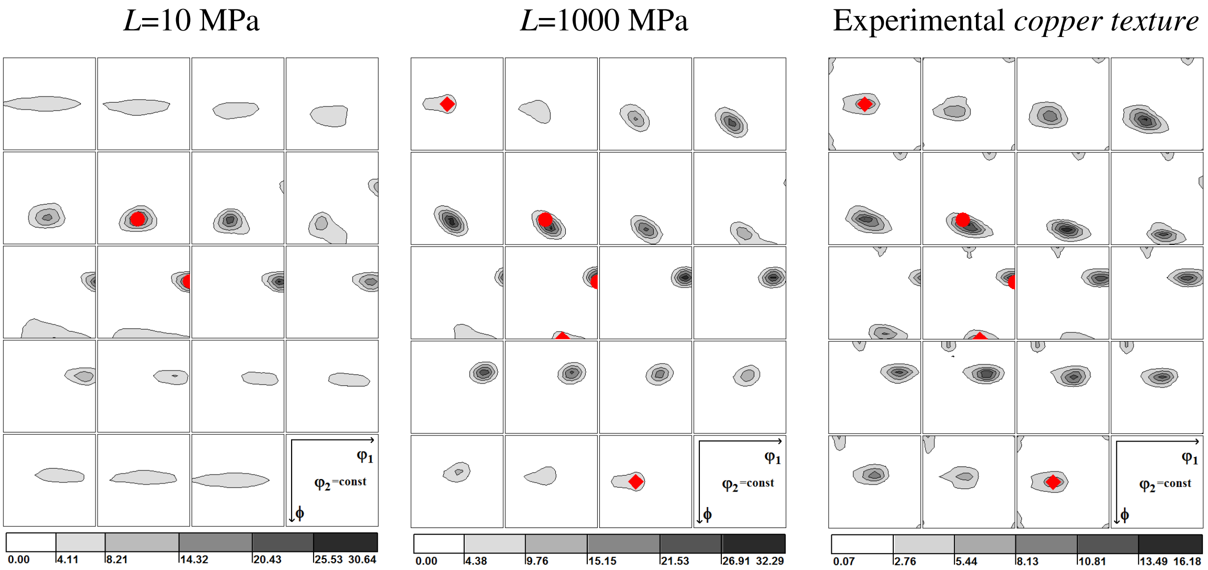

Fig. 2.2. *Textures predicted with **CL lattice rotation** and {111}<110> slip mode, for L=10 MPa and L=1000 MPa, compared with experimental copper rolling texture. The copper component C (●) and brass component B (♦) are marked.*

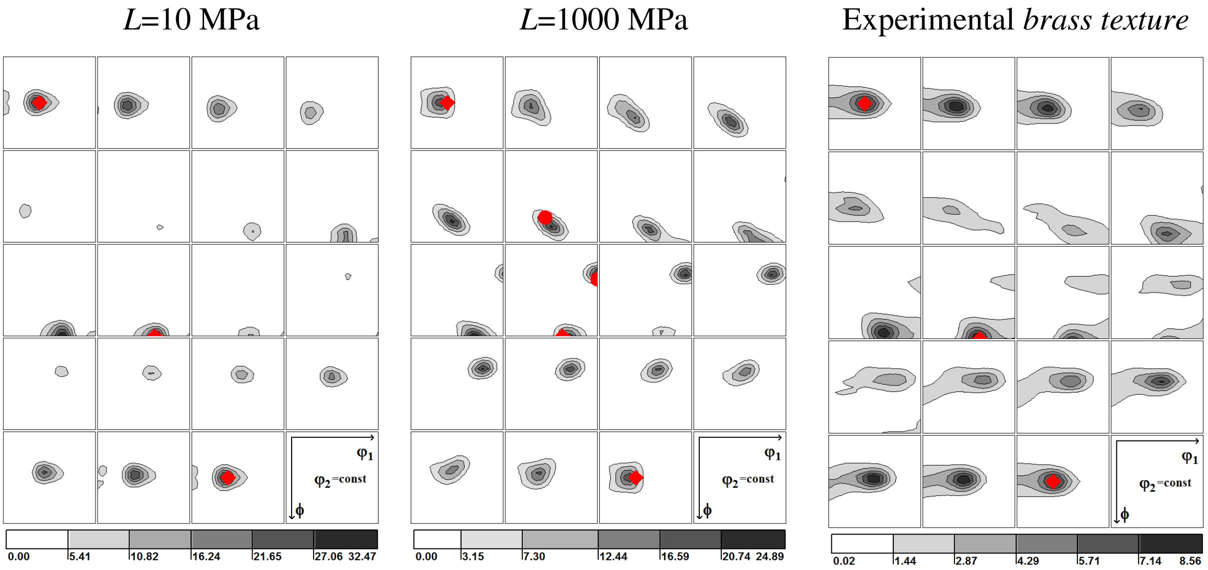

Fig. 2.3. *Textures predicted with **PR lattice rotation** and {111}<110> slip mode, for L=10 MPa and L=1000 MPa, compared with experimental brass rolling texture. The copper component C (●) and brass component B (♦) are marked.*

Also, the volume fractions (in per cents) of selected ideal orientations in the model predicted textures were determined (for a given ideal orientation g_A, its fraction is calculated as a proportion of model crystallites, whose orientations are distant from g_A less than 15°).

Four f.c.c. rolling textures the following components were examined:

- C (copper) component: $\{112\} < \bar{1}\bar{1}1 >$ ($\varphi_1=90°$, $\phi=35°$, $\varphi_2=45°$),
- B (brass) component: $\{011\} < 2\bar{1}1 >$ ($\varphi_1=35°$, $\phi=45°$, $\varphi_2=0°$),
- S component: $\{213\} < \bar{3}\bar{6}4 >$ ($\varphi_1=59°$, $\phi=37°$, $\varphi_2=63°$),
- G (Goss) component: $\{011\} < 100 >$ ($\varphi_1=0°$, $\phi=45°$, $\varphi_2=0°$).

Variations of R_C, R_B and of fractions of the ideal orientations versus L are shown in Figs. 2.4 and 2.5. R_C is clearly higher than R_B in the whole range of L for *CL* definition (Fig. 2.4). We also observe that the copper component (*C*) is strongly dominant over the brass component (*B*) in this approach (Fig. 2.5). Hence, in the frame of *CL* definition only the copper-type texture can be predicted, independently of L value.

In contrast, *PR* definition leads to a more complex behaviour. For $L \leq 100$ MPa we obtain the brass-type texture: R_B is evidently higher than R_C and also *B* component is predominant over *C* one in this range - Figs. 2.4 and 2.5. On the other hand, for $L \geq 1000$ MPa the predicted texture becomes close to the copper-type one ($R_C > R_B$) with an increasing participation of *C* orientation - Fig. 2.5. Therefore, we can conclude that if *PR* lattice rotation definition is used, one observes the transition from the brass-type to the copper-type texture in the range of L between 100 MPa and 1000 MPa.

It should be noted that *S* component is quite strong in textures predicted for both rotation definitions. An interesting observation is that for a very high interaction level (L=5000 MPa), the predicted textures for *CL* and *PR* definitions are practically the same and close to the copper-type texture. This is confirmed by the same values of R_C and R_B correlation factors (Fig. 2.4) and nearly the same fractions of ideal texture components (Fig. 2.5). It is a consequence of the relation: $\delta\varepsilon_{32} \cong \delta\varepsilon_{32} \cong \delta\varepsilon_{32} \cong 0$ occurring in the case of plane strain deformation, if strong interaction level is applied (cf. Eq.2.5).

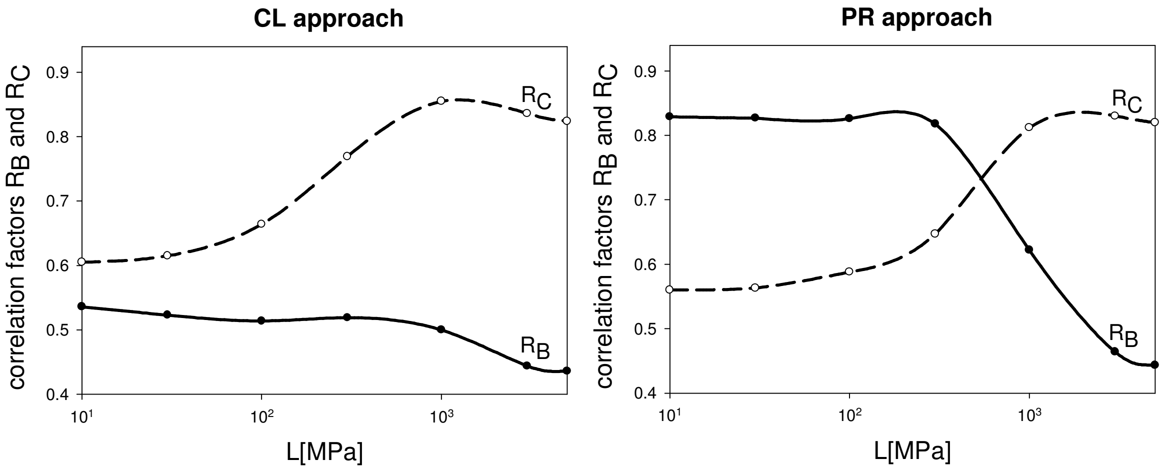

Fig. 2.4. Correlation factors R_B and R_C versus L for CL and PR lattice rotation; {111}<110> slip mode was assumed.

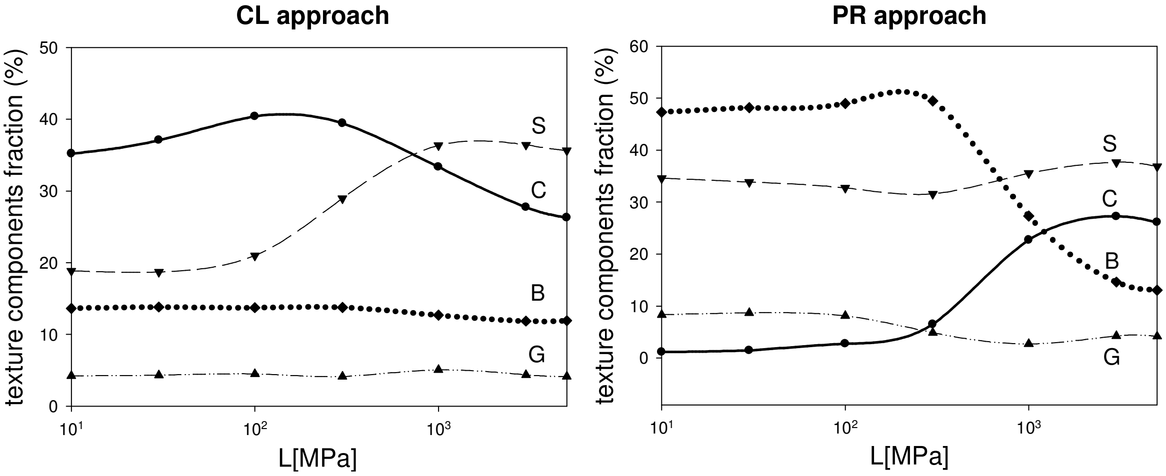

Fig. 2.5. Fractions of various texture components (in per cents) within 15° from the ideal orientations versus L for CL and PR lattice rotation; {111}<110> slip mode was assumed.

In Table 2.2 we compare the fractions of texture components derived from Fig. 2.5 for the conditions corresponding to the highest values of R_C and R_B in Fig. 2.4, i.e., L = 1000 MPa combined with *CL* and L=10 MPa combined with *PR*, respectively, with the experimental fractions for copper and brass rolled to 60% reduction.[1] The fractions of the main components of both types of texture (i.e., *C* for copper-type texture and *B* for brass-type texture), derived from the simulations, are clearly higher than those from experimental

---

[1] Orientations fractions in experimental textures were calculated in the same way as in the case of simulated textures. Each experimental texture was discretized into 5000 hypothetical eqi-volume grains, with the orientation distribution according to the experimental ODF. Next, the same procedure as for simulated textures was applied.

textures. It means that the simulated textures are much sharper than the experimental ones – a conclusion which is also confirmed in Figs. 2.2 and 2.3.

Table 2.2 *Fractions of the main texture components (volume percents within 15° from the ideal orientations) for the simulation conditions corresponding to the highest values of* R_C *and* R_B *together with the fractions for the copper and brass textures.*

	L = 1000 MPa, *CL*	Copper texture	*L* = 10 MPa, *PR*	Brass texture
Copper component	33	15	1	6
Brass component	13	12	47	16
S component	36	27	35	20
Goss Component	5	3	8	5

The main conclusion is that for *CL* definition, independently of *L* value, it is not possible to predict the brass-type texture, if the *{111}<110>* slip is the sole deformation mechanism. Only the copper type-texture can be obtained in this approach.

On the other hand, *PR* definition enables to predict both types of f.c.c rolling texture. For a weak interaction intensity (*L* between 0 and 100 MPa), one obtains the brass-type texture, while for higher *L* values (*L* > 1000 MPa) – the copper-type texture is predicted. A continuous transition between two types of f.c.c rolling textures is observed in function of *L* parameter. However, it should be noted that a better copper-type texture prediction for *L*=1000 MPa is obtained with *CL* rotation definition (R_C=0,86) than for *PR* definition (R_C=0,83). The above results confirm the importance of the level of grain-matrix interaction, *L*, as well as of the lattice rotation definition. The latter has to be defined for a given geometry of deformation.

Therefore, we conclude that the best prediction of the copper-type texture is obtained for CL rotation definition combined with L=1000 MPa, while of the brass-type texture - for PR rotation definition with L=10 MPa.

The main deficiency of the predicted textures, presented above, is their higher intensity compared to experimental ones. To improve this situation, the so called 'random stresses' were introduced. Corresponding results are presented in the next section.

2.5.2 Inclusion of 'random stresses' with {111}<110> slip

The notion of 'random' stresses was introduced by Leffers in his pioneer work on rolling texture prediction[1]. The introduction of random stresses may look like a mathematical trick, but they were introduced with the specific purpose of mimicking the interaction with individual neighbouring grains which, in 1-point models, is a random effect. The random stresses, σ_{ij}^{random}, are added to those from Eq. 1.3:

$$\sigma_{ij} = \Sigma_{ij} + L(E_{ij}^{p} - \varepsilon_{ij}^{p}) + \sigma_{ij}^{random} \tag{2.6}$$

Each component of random stresses is allowed to operate in a number of steps randomly selected between zero and 30% of the average number of steps needed to reach 60% reduction. The amplitude of these stresses was selected as a random value between ± 0.35 Σ_{11} (i.e., ±35% of the main component of the applied stress). These parameters for the random stresses were selected by a trial-and-error procedure aiming at the maximum agreement with the experimental brass texture, highest value of R_B. Their presence makes the predicted textures 'smoother' and of lower intensity.

The correlation factors R_C and R_B versus L for *CL* and *PR* rotation definitions, calculated for {111}<110> slip with random stresses added are shown in Fig. 2.6. The overall picture is similar to that in Fig. 2.4, but the actual values of R_C and R_B have changed somewhat. It can be seen that for low L values with the presence of random stresses, a better brass texture is predicted in the frame of *PR* definition (correlation factor R_B of 0.92 instead of 0.83). Also the agreement of the predicted copper-type texture (*CL* rotation definition, L=1000 MPa) with the experimental copper texture was slightly improved with random stresses (R_C raised from 0.86 to 0.87).

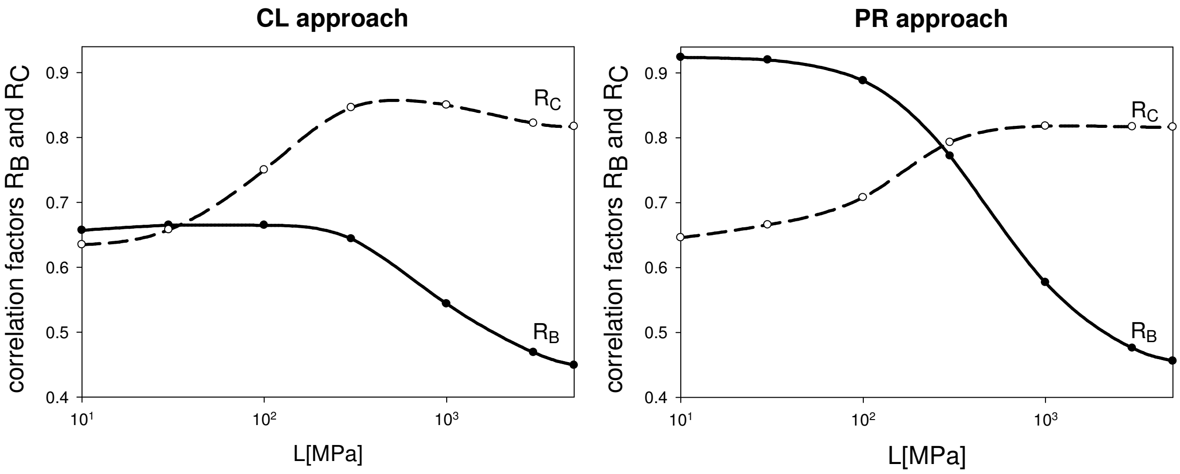

Fig. 2.6. Correlation factors R_B and R_C versus L for CL and PR lattice rotation; {111}<110> slip mode was assumed in the presence of random stresses.

The simulated textures for two definitions of lattice rotation together with experimental ODFs are shown in the figure below. As compared with Figs. 2.2 and 2.3 there are certain changes, e.g., the simulated ODFs in Figs. 2.7 and 2.8 have lower intensities, closer to experimental textures. As shown in Fig. 2.6 there is a really good agreement between simulated and experimental textures (high correlation factors).

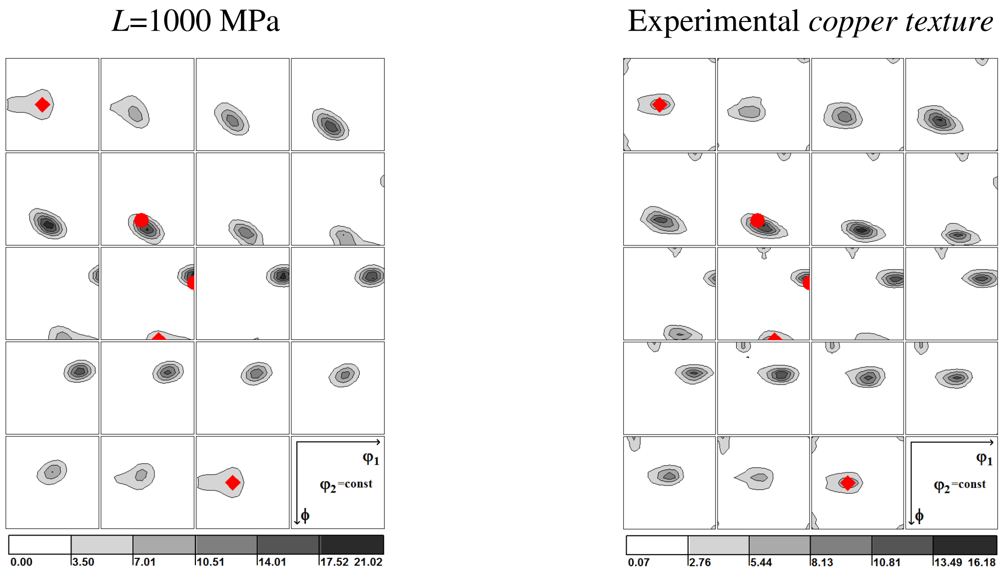
L=1000 MPa

Experimental *copper texture*

*Fig. 2.7. Texture predicted with **CL lattice rotation** and {111}<110> slip mode for L=1000 MPa with the presence of **random stresses**, compared with experimental rolling texture of copper. The copper component C (●) and brass component B (♦) are marked.*

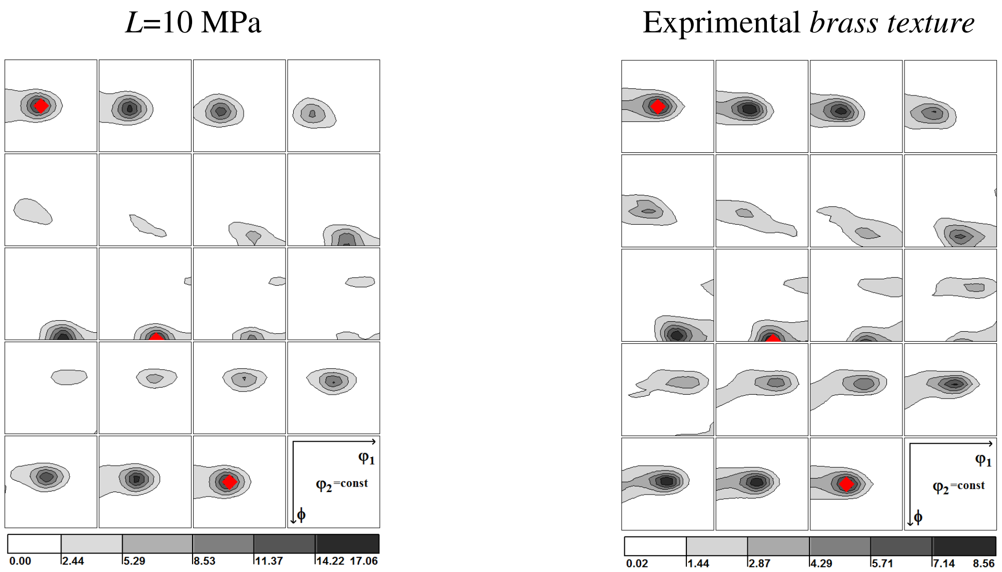
L=10 MPa

Exprimental *brass texture*

Fig. 2.8. *Texture predicted with* ***PR lattice rotation*** *and {111}<110> slip mode for L=10 MPa with the presence of* ***random stresses****, compared with experimental rolling texture of α-brass. The brass component B (♦) is marked.*

In the figure below the fractions of texture components calculated for *CL* and *PR* definitions, assuming {111}<110> slip and random stresses added, are shown. Similarly, Table 2.3 corresponds to Table 2.2, but with addition of random stresses. Comparison of Fig. 2.9 and Table 2.3 with Fig. 2.5 and Table 2.2 confirms that the addition of random stresses does lead to a decreased sharpness of the simulated textures - to a level closer to that of the experimental textures.

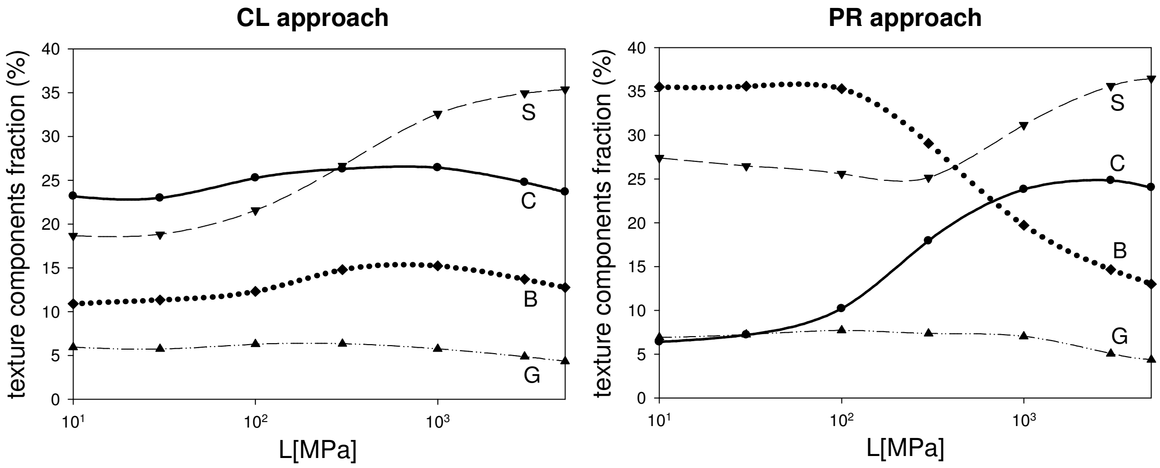

Fig. 2.9*. Fractions of the various texture components within 15° from the ideal orientations versus L for CL and PR lattice rotation definitions; {111}<110> slip and random stresses mode was assumed.*

Table 2.3. *The equivalent of Table 2.2 but now with random stresses added.*

	L = 1000 MPa, *CL*	Copper texture	L = 10 MPa, *PR*	Brass texture
Copper component	26	15	6	6
Brass component	15	12	36	16
S component	33	27	27	20
Goss Component	6	3	7	5

It is well known that a low interaction level (L) leads to the Sachs type deformation, i.e., homogeneous stress state, in which single and duplex slip are operating. Such deformation pattern leads to the brass-type texture. This fact was explained by Leffers [23], who observed the formation of thin twin lamella in the rolled polycrystalline brass. The surfaces of these lamella are roughly parallel to the planes of main active slip systems. In consequence, they block dislocation movements from primary slip systems to other ones and, finally, one or two slip systems operate during deformation. Such microstructure geometry is shown schematically in Fig. 2.10. On the other hand it is obvious that grains deforming by single or duplex slip do not deform in a 'Taylor type' way'. Therefore a remaining material has to deform in a way assuring the material continuity. This effect can explain the appearance of 'random stresses'.

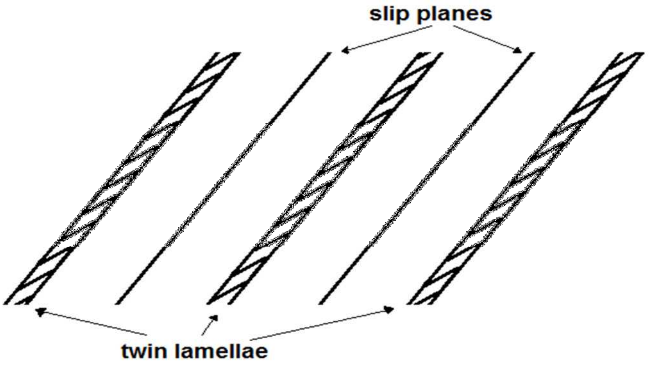

Fig. 2.10. *Scheme of microstructure, which favours an extended activity of primary slip systems during deformation.*

As shown in this section, very satisfactory predictions of the copper and brass-type textures were obtained. Nevertheless, in the sake of completeness, also other mechanisms indicated in literature were considered in our calculations. They are presented in the following sections.

2.5.3 Dissociation of <110> perfect dislocations into <112> partials on {111} planes

In f.c.c. metals and alloys perfect dislocations with *a/2 <110>* Burgers vector may dissociate into two Shockley partial dislocations with *a/6 <211>* Burgers vectors - with a distance between the partials which increases with decreasing stacking fault energy. For a dislocation in the $(1\bar{1}1)$ plane for instance:

$$\frac{a}{2}[110] \rightarrow \frac{a}{6}[121] + \frac{a}{6}[21\bar{1}] \tag{2.7}$$

The mechanism of partial dislocations formation is shown in Fig. 2.11.

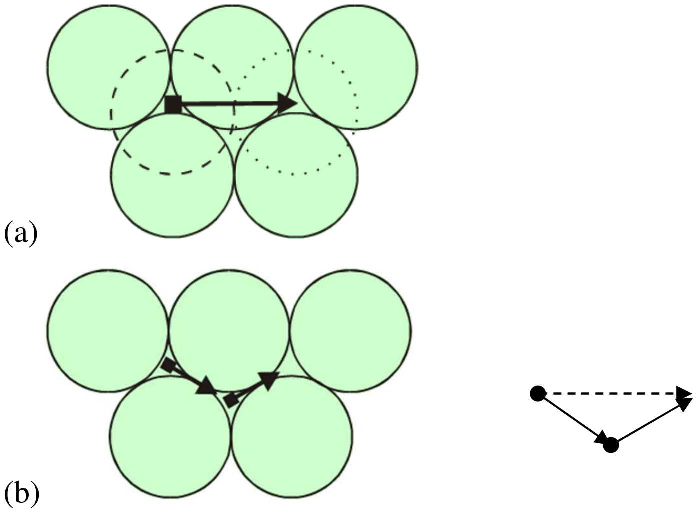

***Fig. 2.11** Formation of two partial dislocations in a material with f.c.c. crystal structure: (a) ideal dislocation, (b) two partial dislocations.*

Hu et al. [39] suggested that {111}<211> slip together with normal {111}<110> slip leads to the brass-type texture whereas {111}<110> alone leads to the copper-type texture. The original suggestion was not supported by quantitative simulations. Wierzbanowski [40] and Leffers and Ray [23] have argued that any significant fraction of uncoordinated slip by partials would lead to an unrealistically high concentration of stacking faults.

Nevertheless we have made simulations with slip by partials – 50% slip by partials and 50% normal slip. The resulting correlation factors are shown in Fig 2.12. Comparison with Figs. 2.4 and 2.6 shows that the addition of slip by partial dislocations leads to a very significant reduction of the agreement with the experimental brass texture, reduction of R_B, for the conditions where the agreement is best without the addition – low L values combined with *PR*. And we remember that slip by partial dislocations was suggested in order to explain the formation of the brass-type texture [39]. Slip by partial dislocations is not expected under the conditions leading to the copper-type texture, and therefore it is irrelevant that it leads to a decreased agreement with the experimental copper texture, decreased values of R_C.

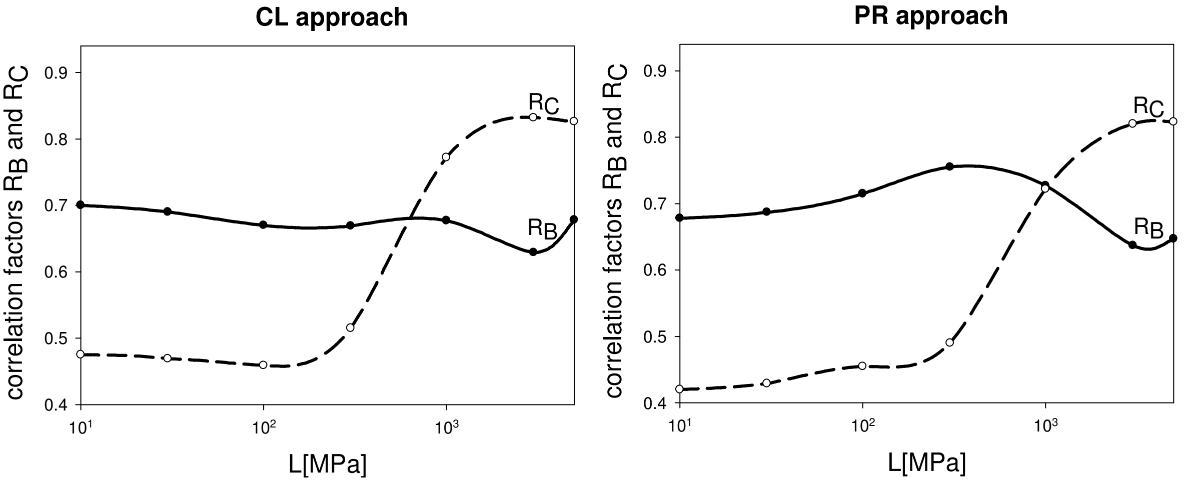

Fig. 2.12. *Correlation factors R_C and R_B versus L for CL and PR lattice rotation with 50% {111}<211> slip and 50% {111}<110> slip.*

2.5.4 Occurrence of {111}<112> deformation twinning in addition to {110}<110> slip

According to the literature there are many evidences that the deviation of the brass-type texture from the copper-type texture is caused by a volume effect of deformation twins: the copper-type texture was supposed to be formed by {111}<110> slip while the brass-type texture was supposed to be formed by {111}<110> slip together with a volume effect of deformation twins. In the present section the influence of twinning on the formation of brass-type texture is checked. It is obvious that a possible volume effect of deformation twins on the formation of the brass-type texture must be seen together with the experimentally observed volume fraction of deformation twins in materials developing a brass-type texture. According to [23] there are only two series of observations: In brass with 15% zinc rolled to reductions of about 40% the volume fraction of deformation twins is only few percents, and in brass with 30% zinc rolled to 76% reduction the volume fraction of deformation twins is less than 25%. By interpolation a volume fraction of deformation twins for reduction 60%, is chosen (in this case ~15%). This is basically the volume fraction that was considered in simulations. Deformation twinning is introduced in our simulations according to the procedure suggested by Tomé et al.[26] which was described in section 1.4.3. Only the twinning in the matrix material was considered. We did not consider re-twinning in the twins. This procedure is simple because the final twinning reorientation applies to whole grain volume based on the predominant twinning system. Thus one avoids grain multiplication with the extensive computer calculations involved. The ratio between the critical resolved shear stress for slip and for twinning determines the amount of twins, but we cannot predetermine the volume fraction of twins by selection of a specific ratio. In order to get a specific fraction of twins we must vary the ratio in a trial-and-error procedure.

The correlation factors versus *L* for *CL* and *PR* with a 15% volume fraction of deformation twins are shown in Fig. 2.13. Comparison with Fig. 2.4 shows that the addition of 15% twins has practically no effect on the correlation factors (and hence on the textures). For *CL* (which is not the lattice-rotation mode leading to brass-type textures anyway) the addition of 15% twins produces a marginal increase of R_B. The main conclusion is that the simulated texture is very close to that without any twinning, and they are not to be shown.

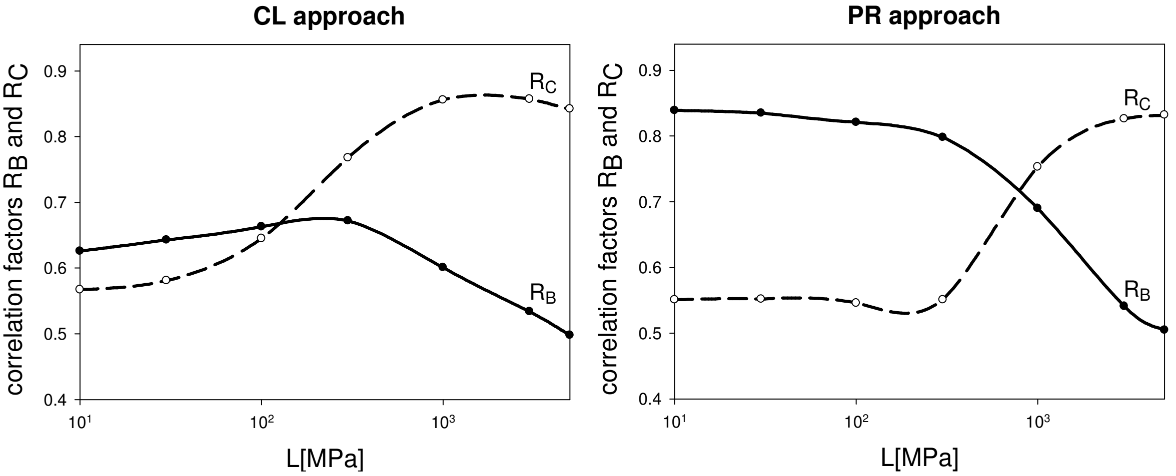

Fig. 2.13. *Correlation factors R_B and R_C versus L for CL and PR lattice rotation with 15% volume fraction of deformation twins; {111}<112> twinning was added to {111}<110> slip.*

Because there are small differences between textures predicted with 15% of volume fraction of twins and textures predicted without twinning so the unrealistically high twin volume fraction of 50% was considered. The predicted ODFs taking into account the

{111}<110> slip and the {111}<112> twinning, with a 50% of volume fraction of deformation twins, are shown in Fig. 2.14 (*CL* definition) and in Fig. 2.15 (*PR* definition). In both cases (*CL* and *PR* definitions) we obtain textures with $R_B > R_C$ for *L* values up to 1000 MPa, but R_B does not exceeds in most cases the value of 0.8 - Fig. 2.16. The two exceptions where $\mathrm{R_B}$ attains 0.8 are: the case of *PR* for low *L* (where the brass-type texture is obtained without twinning anyway - compare Fig. 2.4), and the case of *CL* for *L* between 800 and 1000 MPa (analogous result is reported by some authors). In all predicted textures we observe a strong predominance of *B* orientation over *C* in the whole examined range of *L* value - Fig. 2.17.

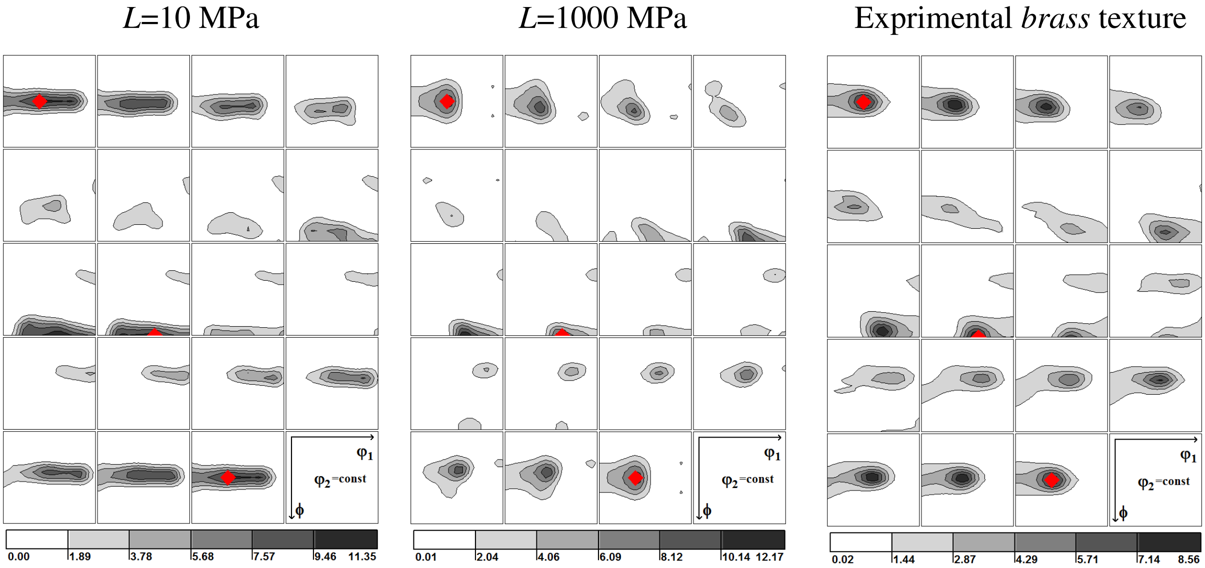

L=10 MPa

L=1000 MPa

Exprimental *brass* texture

Fig. 2.14. *Textures predicted with* ***CL lattice rotation*** *and {111}<112> twinning in addition to {111}<110> slip mode with 50% volume fraction of deformation twins, for L=10 MPa and L=1000 MPa, compared with experimental brass rolling texture. The brass B (♦) component is marked.*

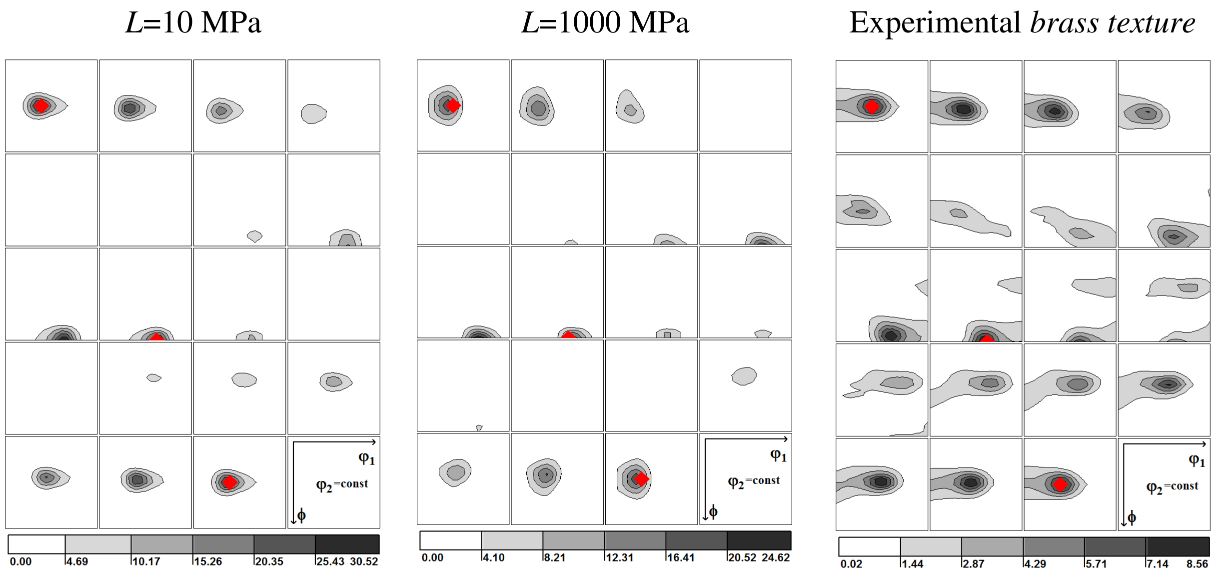

Fig. 2.15. *Textures predicted with **PR lattice rotation** and {111}<112> twinning in addition to {111}<110> slip mode with 50% volume fraction of deformation twins, for L=10 MPa and L=1000 MPa, compared with experimental brass rolling texture. The brass B (♦) component is marked.*

Hence, we can conclude that if an exaggerated volume twinning (in our case 50%) is added to the classical {111}<110> slip – the brass-type texture can be obtained also in the case of *CL* rotation definition for higher *L* values. The similar results were obtained by other authors, for example [25][26][27]. However, the problem is that an intense volume twinning (in this case of 50%) is not observed in α-brass at room temperature. On the other hand, what is really observed are thin twin lamella, and as pointed in Section 2.5.2, their presence favours the glide on principal slip systems. Such the behaviour is simulated by a weak interaction level and if the {111}<110> slip is taken into account as the sole deformation mechanism - the brass-type texture is predicted, as discussed in Section 2.5.1 and 2.5.2.

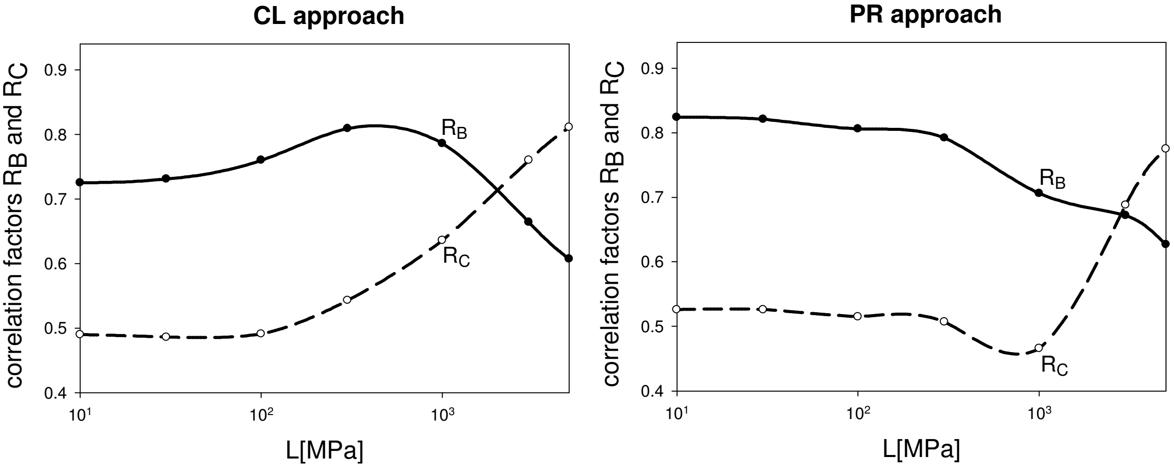

Fig. 2.16. Correlation factors R_B and R_C versus L for CL and PR lattice rotation with 50% volume fraction of deformation twins; {111}<112> twinning was added to {111}<110> slip.

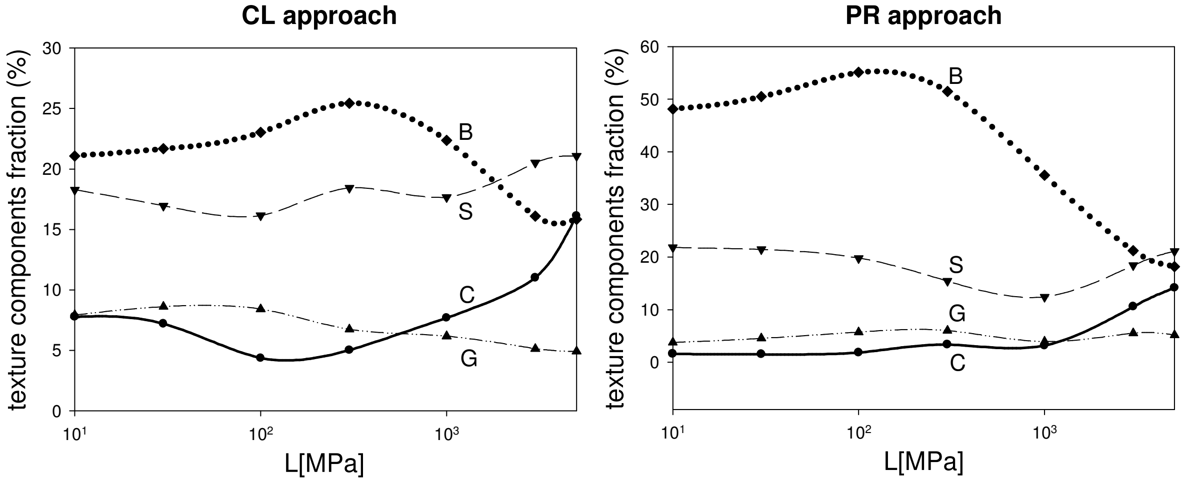

Fig. 2.17. Fractions of texture components versus L for CL and PR lattice rotation with 50% volume fraction of deformation twins; {111}<112> twinning was added to {111}<110> slip.

2.5.5 Slip on non-octahedral slip systems {110}<110> and {100}<110> in addition to {111}<110> slip

The {110}<110> and {100}<110> slip systems, i.e., non-octahedral systems, can be activated in f.c.c. metals at higher temperatures. Their role in brass-copper transition was examined in some works (e.g., [44][45][46]). Haessner [44] suggested that the copper-type texture is formed by slip on {100} and {110} planes together with normal (octahedral) {111} slip while the brass-type texture is formed by normal {111} slip only. This suggestion was not supported by quantitative simulations.

We have made simulations for combined <110>{001}, <110>{110} and <110>{111} slip with the same critical resolved shear stress for the three types of slip systems. Fig. 2.18 shows the resulting correlation factors versus *L* for *CL* and *PR*. Comparison with Fig. 2.4 clearly shows that the addition of non-octahedral slip does not improve the agreement with the experimental copper-type texture. On the contrary R_C does not for any of the conditions represented in Fig. 2.18 approach the highest value in Fig. 2.4, i.e., 0.86. On the other hand, we note that the plots of correlation factors for *PR* and *CL* are very similar in Fig, 2.18 and we do not observe any brass-copper transition vs. *L*, which occurred for *PR* rotation definition in the case of simple <110>{111} slip - cf. Fig. 2.4.

Other quantitative simulations including non-octahedral slip[46] [47][48] confirm our conclusion from Fig. 2.18, viz. that the addition of non-octahedral slip does not contribute to a better agreement with the experimental copper texture. Actually the addition of non-octahedral slip in these works was not motivated by an attempt to produce a copper-type texture as suggested by Haessner, but by an attempt to simulate the textures resulting from rolling at elevated temperatures of materials which develop copper-type textures by room-temperature rolling.

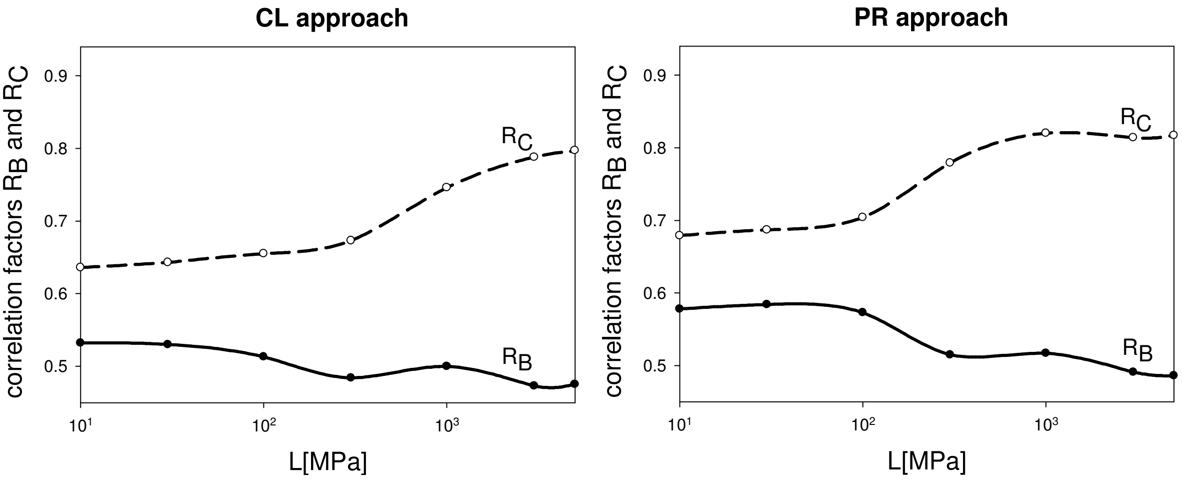

Fig. 2.18. Correlation factors R_B and R_C versus L for CL and PR lattice rotation; {110}<110>+ {100}<110>+ {111}<110> slip mode was assumed.

2.5.6 Activation of cross-slip with {111}<110> slip mode

Cross-slip appears in high stacking fault energy metals, like copper or aluminium. Smallman and Green [49] and Dillamore and Roberts [50] suggested that the brass-type texture is formed by simple {111}<110> slip whereas the copper-type texture is formed by {111}<110> slip with added slip on the cross-slip systems (the cross-slip system has the same slip direction as the primary system but a different slip plane - see Fig. 2.19). Their suggestions were not supported, however, by quantitative arguments.

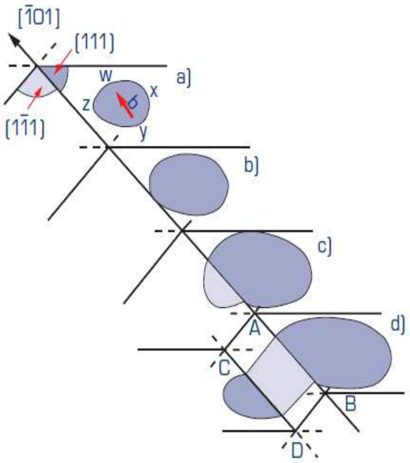

Fig. 2.19. *Cross slip of dislocation loop in f.c.c. structure. The following stages of cross-slip (a-c) and the double cross-slip(d) (after* [51]).

In the simulations presented in this subsection we, after the activation of a <110>{111} slip system, add slip on the corresponding cross-related system – with a shear of 40% of the primary shear. The derived correlation factors are shown in Fig. 2.20. As mentioned, the addition of cross slip was introduced in order to favour the development of the copper-type texture. Comparison of the R_C values from Fig. 2.20 with the R_C values in Figs. 2.4 and 2.6 (without additional cross slip) shows that additional cross slip has practically no effect on the degree of similarity between the simulated and the experimental copper-type texture (the maximum value of R_C in Fig. 2.20 is 0.87 as compared to 0.86 in Figs. 2.4 and 0.87 in Fig. 2.6).

Gangli and Arato [52] made quantitative simulations of texture development for <110>{111} slip with additional cross-slip. They started with conditions corresponding to our *PR* with low *L* (resulting in a brass-type simulated texture), and they then added increasing fractions of cross-slip. With the addition of moderate fractions of cross-slip they claimed to see a texture change in the direction of the copper-type, but they certainly did not reach a proper copper-type texture. With fractions of cross slip of the order of our 40% they got a “super copper” simulated texture quite different from the copper-type texture. This may correspond to the very low R_C values for *PR* combined with low *L* in Fig. 2.20.

Finally, we can conclude that the appearance of the cross-slip in addition to the classical {111}<110> does not increase a degree of similarity between predicted textures and the experimental copper texture.

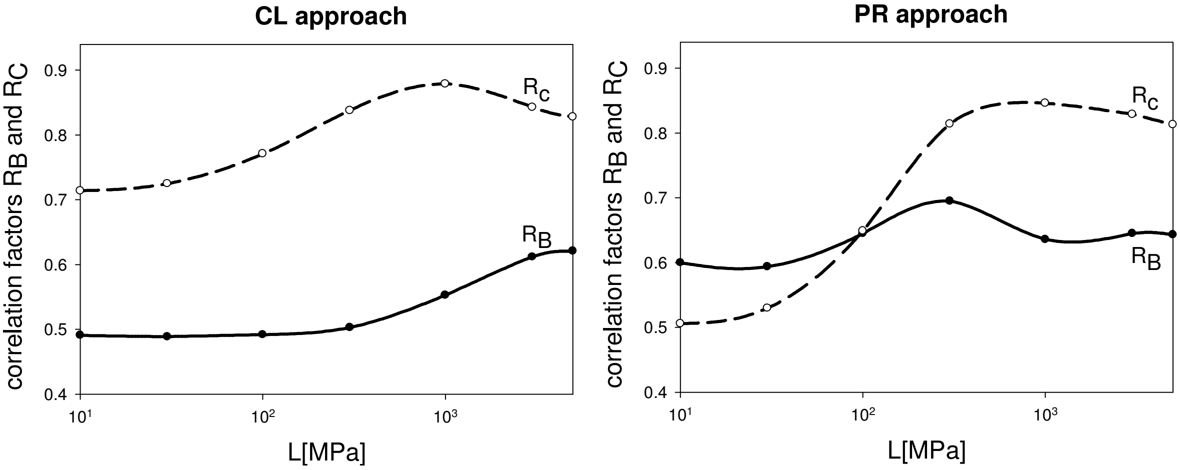

Fig. 2.20. Correlation factors R_B and R_C versus L for CL and PR lattice rotation; {110}<110> slip and associated cross slip.

2.5.2 Remarks about two experimental reference textures used for comparison with predicted textures

Obviously it is absolutely essential that our reference textures, e.g., from Figs. 3b and 4b, are proper representatives for the experimental textures in copper and brass rolled to 60% reduction. This is the reason why the used textures were measured by neutron diffraction, giving information from a huge part of material (the whole sample volume in our case). Our ODFs were synthesized from symmetrised {111}, {200} and {220} pole figures using the PopLA WIMV calculation method [53]. The pole figures were measured by neutron diffraction with a four-circle diffractometer at the High Flux Reactor in Petten, Holland. The materials were commercially pure copper and brass with 30% zinc, rolled to 60% reduction starting with almost random texture.

2.6 Conclusions

There is a long discussion in the literature about mechanisms, which can explain the formation of the brass-type texture and possible transition from the copper-type texture to the brass-type texture. Accordingly, there were many trials to predict the copper and brass-type textures using deformation models.

As shown in this work, the formation of the **brass-type texture** can be predicted using the {111}<110> slip in the frame of a weak interaction model (low *L* values) with PR lattice rotation definition. This model leads to a single and duplex slip deformation pattern in grains. According to experimental observations of Leffers [23], such the behaviour is favoured in α-brass by the formation of thin twin lamella. They confine the dislocation movement to principal slip systems, hence they impose a single and duplex slip. The formation of thin twin lamella should not to be confused with the volume twinning; the latter does not appears in α-brass in sufficient quantity at room temperature. Moreover, we can add random stresses, which reflect the interactions of grains having such limited slip pattern with the neighbouring material. With these additional stresses we obtain still better agreement of the predicted brass-type texture with the experimental brass texture.

Our calculations showed that adding {111}<112> slip (movement of partial dislocations) to the classical {111}<110> slip mode does not explain the formation of the brass-type texture. As to a possible volume effect of {111}<112> deformation twins on the formation of the brass-type texture, our quantitative simulations confirm that a realistic volume fraction of twins, ~15% at 60% reduction, cannot have any significant effect on the texture. The simulation with an exaggerated twin volume fraction of 50% confirms that a sufficiently high volume fraction of deformation twins added to conditions which would otherwise lead to a copper-type texture - changes the predicted texture in the direction of the brass-type texture. However, apart from the fact that it is unrealistic twinned volume fraction, also the correlation factor derived does not reflect a satisfactory agreement with the experimental brass texture.

In contrast to the above, the **copper-type texture** is much easier to explain. It is predicted assuming a strong interaction level (high *L* values) and the {111}<110> slip. The best agreement with experimental copper texture is obtained for CL definition of rotation.

Therefore, finally we can state that:

- the simplest explanation of the **brass-type texture** formation involves the following model variables :
- {111}<110> slip,
- *PR* lattice rotation definition,
- low interaction level (i.e., low values of *L*); it leads to a dominating single or duplex slip deformation pattern, which is favoured in real polycrystalline α-brass sample by the formation of thin twin lamella,
- adding of random stresses.

- the simplest explanation of the **copper-type texture** formation involves:
- {111}<110> slip,
- *CL* lattice rotation definition (PR definition also leads to an acceptable result),
- high interaction level, i.e., high values of *L*, which leads to a multi-slip deformation pattern.

Chapter 3

3 Implementation of Crystallographic Model into Finite Element Method

3.1 Introduction

One of goals of this work was to implement the crystallographic deformation model to the Finite Element Method (FEM). The LW crystallographic model was implemented into ABAQUS/Explicit finite element code using subroutine VUMAT. The LW model was selected because it is quick and relatively simple in its formulation. As a result, the FEM+LW model was obtained. In order to check this software, the uniaxial tension test was simulated and predicted texture was compared with experimental data

The FEM+LW model is an efficient tool which enables to study heterogeneous elasto-plastic deformation processes, taking into account its crystallographic nature. The FEM+LW model was applied in the present work for a study of asymmetric rolling (AR) process, but it can be also applied to other deformation processes, with complex geometry, like deep drawing, extrusion or stamping.

3.2 Description of the program ABAQUS

The FEM computer software used in this work is ABAQUS - the package of programs used to solve complex engineering problems. This software is designed to analyze problems of solid mechanics, structure, heat transfer, electromagnetic field, etc. It is commonly used in automotive engineering, metallurgy and mining, shipbuilding and in the air industry. It is especially useful to assess the strength of machine elements and of constructions. ABAQUS was created and developed by the American company Hibbitt, Karlsson & Sorensen. The main advantage of this package is a modular design.

ABAQUS program includes the three basic modules:

- **ABAQUS/CAE** (Complete ABAQUS Environment) - interactive pre-and postprocessor.

CAE is a graphical user interface, which allows an easy modelling, design, editing, diagnosing. It also allows the visualization of results obtained from ABAQUS/Standard and ABAQUS/Explicit simulations. ABAQUS/CAE is divided into functional units called modules, each module defines a logical aspect of the modelling process (e.g., a sample geometry, definition of material properties and meshing ...). This allows a combination of any of these elements. One can create any combination of parts, finite elements, materials, procedures and sequence analysis of the loads. In order to build a model one has to move from module to module, after that ABAQUS/CAE generates an input file that one submits to the ABAQUS/Standard or ABAQUS/Explicit analysis product. The input file is a text file (*.inp), the syntax of which is based on keywords. If it is needed one can modify the project using any text editor e.g. Notepad. The calculation results are saved in a database file *.odb, which can be viewed and analyzed in the visualization module: ABAQUS/Viewer (which is incorporated into ABAQUS/CAE).

- **ABAQUS/Standard** - is the finite elements analysis program, which is ideal for static and low-speed dynamic events and it gives highly accurate stress solutions appropriate to this environment. One of the advantages of ABAQUS/Standard is that the user can analyze a model both in the frequency and time domains.
- **ABAQUS/Explicit** - module designed especially to solve problems of dynamics (very fast processes) and used in the calculation of ballistic impacts, collisions of cars, collisions of objects, interaction models. ABAQUS/Explicit is very effective at handling severely nonlinear behaviour, examples being forging and the slow crushing of energy absorbing devices.

Both methods: ABAQUS/standard and ABAQUS/Explicit can be combined. The result obtained from one of these methods in any moment can be used as the initial condition for the other method. This flexibility provided by the combination between ABAQUS/Explicit and ABAQUS/Standard allows the relevant parts of the simulation to be done in ABAQUS/Standard and ABAQUS/Explicit. An example of this is that a part of analysis can be done in steady state while other parts of the model are highly transient.

The library of models of materials allows for modelling isotropic and anisotropic metals in the adiabatic and isothermal processes, for small and large strain rate. The library also contains material models for analysis of rubbers, plastics, composites, reinforced concrete, foam materials and geotechnical media such as land or rocks.

Library analysis procedures offers the following analysis:

- Linear and nonlinear statics,
- Linear analysis of dynamic loads,
- Thermal conductivity and thermal stress analysis,
- Analysis of coupled thermal and electrical phenomena,
- Analysis of fluid flow through porous materials,
- Analysis of diffusion processes of the masses,
- Acoustic analysis,
- Analysis of piezoelectricity,
- Analysis of shock waves in the liquid,
- Mechanics of cracks.

These analyses can be performed independently, sequentially or as completely coupled, i.e. with the stress analysis.

ABAQUS/Standard and ABAQUS/Explicit have interfaces that allow the user to implement general constitutive equations.

- In ABAQUS/Standard the user-defined material model is implemented in user subroutine UMAT.
- In ABAQUS/Explicit the user-defined material model is implemented in user subroutine VUMAT.

These procedures enable to define any constitutive model of arbitrary complexity. The subroutines work in parallel with the main program by downloading from it the necessary variables. Values calculated by a subroutine are stored in relevant tables and saved in *.odb file, which allows the subsequent use of ABAQUS/Viewer and ABAQUS/CAE environment for data analysis. In the present work the calculations using the ABAQUS package version 6.7.1 was carried out in the Academic Computer Centre CYFRONET, Kraków, and some parts of calculations were made also in Laboratoire des Sciences des Procédés et des Matériaux (LSPM) in University Paris 13.

3.3 ABAQUS/Explicit and quasi-static analysis

In order to implement the crystallographic model into the finite element code the user subroutine VUMAT was used. This subroutine is used by ABAQUS/Explicit module. VUMAT is used to define the mechanical constitutive behaviour of a material. It is called for a set of calculation points for which the material property is defined in a user subroutine. The subroutine VUMAT has two sets of variables, one - only for 'read' (not modifiable variables) and the other - only for 'write' (modifiable variables). At the end of each increment, for which VUMAT is called, it has to update the stresses and solution-dependent state variables. A detailed description of the subroutine VUMAT can be found in the Manual[54].

The applied user subroutine interface is:

```
 subroutine vumat(
C Read only (unmodifiable)variables -
 1 nblock, ndir, nshr, nstatev, nfieldv, nprops, lanneal,
 2 stepTime, totalTime, dt, cmname, coordMp, charLength,
 3 props, density, strainInc, relSpinInc,
 4 tempOld, stretchOld, defgradOld, fieldOld,
 5 stressOld, stateOld, enerInternOld, enerInelasOld,
 6 tempNew, stretchNew, defgradNew, fieldNew,
C Write only (modifiable) variables -
 7 stressNew, stateNew, enerInternNew, enerInelasNew )
C
 include 'vaba_param.inc'
C
 dimension props(nprops), density(nblock), coordMp(nblock,*),
 1 charLength(nblock), strainInc(nblock,ndir+nshr),
 2 relSpinInc(nblock,nshr), tempOld(nblock),
 3 stretchOld(nblock,ndir+nshr),
 4 defgradOld(nblock,ndir+nshr+nshr),
 5 fieldOld(nblock,nfieldv), stressOld(nblock,ndir+nshr),
 6 stateOld(nblock,nstatev), enerInternOld(nblock),
 7 enerInelasOld(nblock), tempNew(nblock),
 8 stretchNew(nblock,ndir+nshr),
 8 defgradNew(nblock,ndir+nshr+nshr),
 9 fieldNew(nblock,nfieldv),
 1 stressNew(nblock,ndir+nshr), stateNew(nblock,nstatev),
 2 enerInternNew(nblock), enerInelasNew(nblock),
C
 character*80 cmname
C

 do 100 km = 1,nblock
 'user coding - in our case LW model'
 100 continue
 return
 end
```

In general, the module ABAQUS/Explicit is used for solving dynamic problems but also it can be used for solving a certain class of nonlinear problems that are essentially static. The newly created FEM+LW model was used to simulate the process of AR, which can be classified as a nonlinear quasi-static problem. The studied AR deformation was realized using two identical rolls, driven by independent motors, rotating with different angular velocities. In this process a complex contact friction appears between a sample and rolling mills. Therefore, ABAQUS/Standard (implicit solver), used to simulate this problem, can encounter some convergence problems; this is the reason why the explicit method was used.

Calculations in Explicit procedure are made in time domain and in general they are used to study very fast processes (total simulation time is small). On the other hand a quasi-static process is, by definition, a long-time process. The total simulation time is divided into small time increment. In each time increment and for each finite element the subroutine VUMAT, where LW model is incorporated, was called. In fact, it is impractical to make the calculation in a natural time scale, which requires a huge number of small time increments. Obviously, the computation time is increased with increasing number of the time increments. In order to reduce the number of time increments the process has to be accelerated, e.g. we can increase the rate of deformation, which reduces the total simulation time. It should be noted that when the process is accelerated, inertial forces become more dominant and the process is no longer quasi-static. In order to obtain stable solutions by ABAQUS/Explicit solver, the kinetic energy has to be controlled during calculations. For quasi-static process the kinetic energy of the deformed material should not exceed a small fraction (typically 10%) of the internal energy during whole deformation[54]. The loading rates inferior than 1% of the acoustic wave velocity u in a material were used in the calculations, which is recommended in the ABAQUS manual. The numerical stability restricts the time increment of simulations in the explicit approach to:

$$\Delta t \leq \frac{h}{u} \quad \text{with:} \quad u = \sqrt{\frac{E}{\rho}} \tag{3.1}$$

where h is a characteristics length associated with an element, ρ is the density of a material, E is Young modulus and the minimum Δt is selected over all elements in the mesh[55]. In general, the time increment has to be equal or shorter than the time required for the acoustic wave propagation across the smallest element, hence usually it is very small.

3.4 Implementation of LW crystallographic deformation model into FEM code

The implementation of crystallographic model (LW) into FEM code is an important issue for the description of anisotropic behaviour of metals during industrial processing. LW model was implemented into ABAQUS/Explicit FEM and, as a result, the FEM+LW model was created. It was assumed that the whole deformed sample, consisted of many smaller representative polycrystalline samples with appropriate number of grains, existing at each Gauss integration point. Calculations in ABAQUS were carried out incrementally in the time domain. The complete macroscopic solution is then obtained by dividing the deformation process into thousands small time increments, and in each increment the new properties (i.e. grain orientations, state of hardening, grains stress and strain, ...) of each individual sample are calculated and uploaded. We deal with two kinds of variables: global ones (concerning a local polycrystalline sample in a given Gauss point) and local ones (concerning individual grains). The calculation sequence in VUMAT subroutine (where LW model is implemented), in each Gauss point is as follows:

- in the beginning of each calculation step the ABAQUS/Explicit program transfers to the VUMAT procedure a total strain increment ΔE_{ij} to be attained in this step. (It is calculated according to the formula: $\Delta E_{ij} = \Delta t \dot{E}_{ij}$, where $\dot{E}_{ij}$ is the strain rate tensor, assumed to be constant during a time increment).
- LW model performs the calculation of the elastic and plastic parts of the strain increment and determines a new resulting stress state Σ_{ij}^{new} using the elastic constitutive relation (Hooke's law in our case). This stress state is transferred to ABAQUS and it becomes Σ_{ij}^{old} in the beginning of the following step.

The VUMAT subroutine has to treat the evolution of internal (or state) variables of the problem. In the case of micromechanical modelling, the number of these variables is very important. The following list summarizes the variables introduced in our case:

- global elastic and plastic strain tensors
- local elastic and plastic strain tensors,
- local stress tensor,
- crystallographic orientations of grains,
- slip systems and their critical shear stresses,

- twinning systems and their critical shear stresses,
- plastic shears of slip and twinning systems,
- parameters characterizing the hardening law,
- twinned volume fractions.

The schematic representation of this explicit strain method is illustrated in Fig. 3.1.
The schematic representation of the implementation of LW model into FEM is shown in Fig. 3.1.

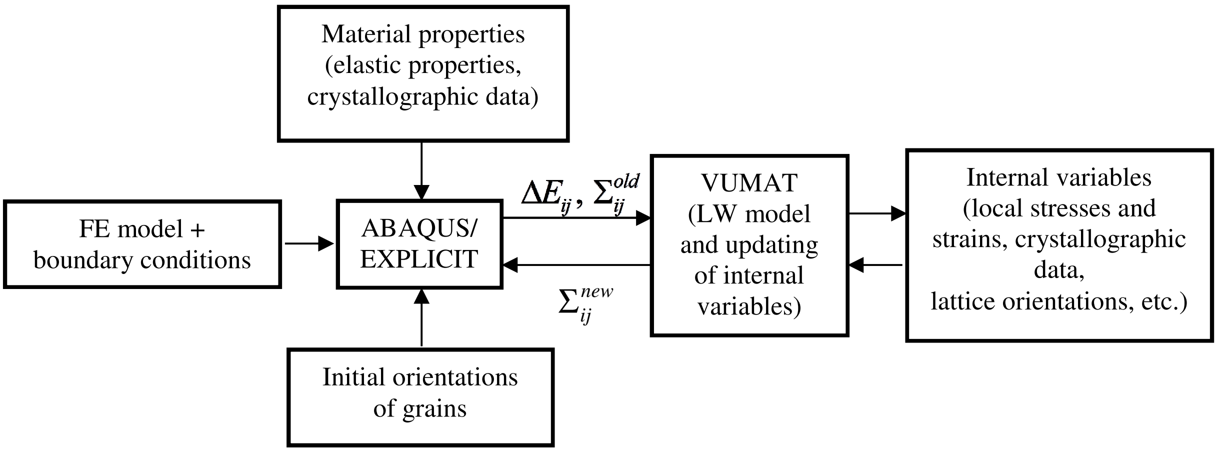

Fig. 3.1. *General principle of implementation of constitutive law (LW model) in ABAQUS/Explicit program (via VUMAT subroutine).*

A more detailed description of the interaction between ABAQUS and LW model is shown in Fig. 3.2. In the first step of calculation, a trial value of stress is calculated assuming a purely elastic material response ($\Delta E_{ij} = \Delta E_{ij}^{e}$) and, consequently, $\Sigma_{ij}^{trial} = \Sigma_{ij}^{old} + D_{ijkl}\Delta E_{kl}^{e}$ (where ***D*** is the elasticity constant tensor). Next, it is checked whether any slip system is activated with the Σ_{ij}^{trial} stress state in any grain of a sample belonging to the considered Gauss point. If not, then the whole imposed deformation increment is considered as elastic one, and: $\Sigma_{ij}^{new} = \Sigma_{ij}^{trial}$. In the opposite case, i.e., if at least one slip system is activated in a model sample, the plastic strain increment is calculated for a given Gauss point, ΔE_{ij}^{p}, using LW model. To perform this calculation, the current state variables associated with a treated Gauss point have to be identified. Their evolution must be done in parallel with the calculation of ΔE_{ij}^{p}. The increment of elastic strain is calculated assuming the additive decomposition of the total strain increment into elastic and plastic parts: $\Delta E_{ij}^{e} = \Delta E_{ij} - \Delta E_{ij}^{p}$. Finally, Σ_{ij}^{new} is calculated using the expression: $\Sigma_{ij}^{new} = \Sigma_{ij}^{LW(end)} + D_{ijkl}\Delta E_{kl}^{e}$. Before closing the VUMAT subroutine, the values of the updated state variables have to be saved (more details about calculations inside LW model are given in the further text). The above operations have to be repeated for all Gauss points of a given element and for all elements of the FE model. The ABAQUS increments are repeated until the final deformation of the examined material is attained.

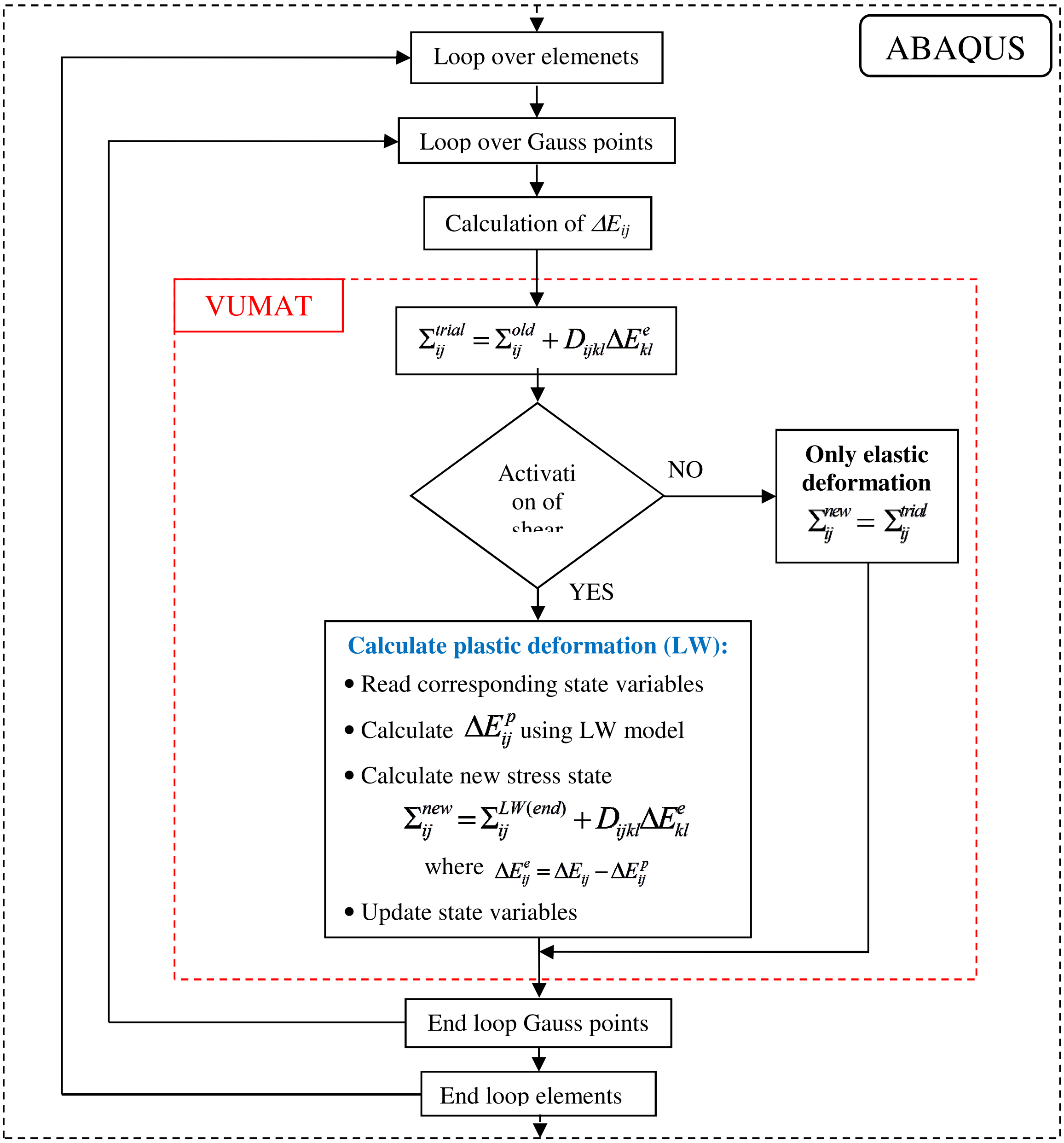

Fig. 3.2. *Flowchart of typical ABAQUS increment with implemented LW model.*

The detailed action of the box “Calculate plastic deformation (LW)” is explained in Fig. 3.3. LW model starts with $\Sigma_{ij}^{0} = \Sigma_{ij}^{old}$. The ‘external’ stress tensor Σ_{ij}^{LW} ’seen’ in the sample belonging to a given Gauss point corresponds to the tensor Σ_{ij} from Eq. 1.3. This stress tensor (Σ_{ij}^{LW}) is being incrementally increased according to the following formula: $\Sigma_{ij}^{LW} = \Sigma_{ij}^{0} + \Delta\Sigma \left\| \Delta E_{ij} \right\|$, where: $\Delta\Sigma$ is a magnitude increment of the applied stress tensor and $\left\| \Delta E_{ij} \right\|$ is the normalized tensor of strain increment (its maximum element equals to 1). In the above equation the isotropic relation between macroscopic stress and strain was assumed. The stress incrementation is continued until the current magnitude of plastic strain in LW model, ΔE_{ij}^{p}, equals to the magnitude of strain increment ΔE_{ij} imposed by ABAQUS program (von Mises measure is used to calculate the strain magnitude). If this condition is fulfilled, the action of LW model is stopped (at this moment: $\Sigma_{ij}^{LW} = \Sigma_{ij}^{LW(end)}$) and the remaining elastic deformation is calculated: $\Delta E_{ij}^{e} = \Delta E_{ij} - \Delta E_{ij}^{p}$. Consequently, the new stress state is calculated as: $\Sigma_{ij}^{new} = \Sigma_{ij}^{LW(end)} + D_{ijkl} \Delta E_{kl}^{e}$, and is transferred to ABAQUS program.

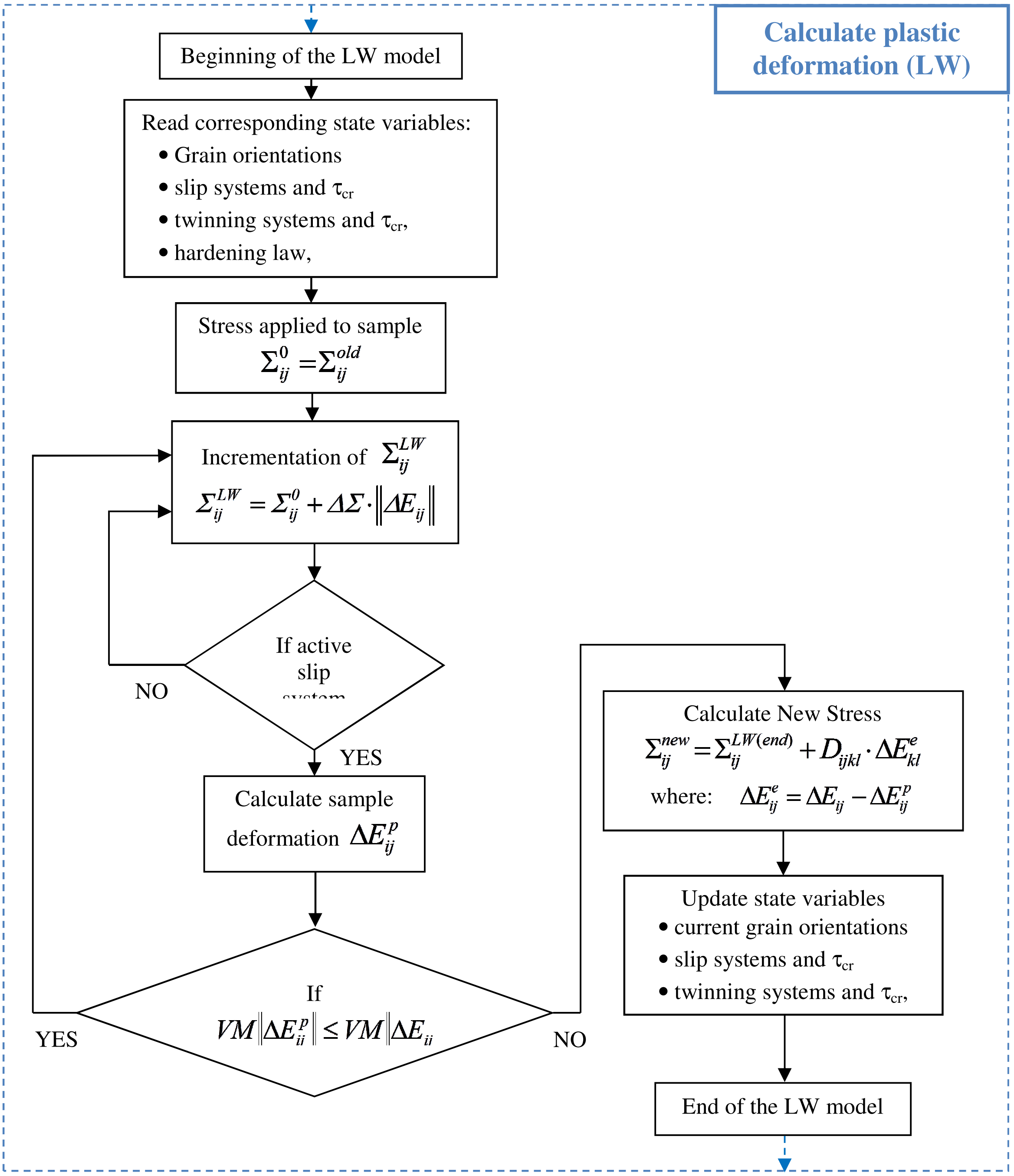

***Fig. 3.3**. Action of LW model marked by the box: "Calculate plastic deformation (LW)" from the previous figure.*

3.5 Calculation for tensile deformation of α-brass with random initial texture

To make a simple test, the tensile deformation of α-brass with random texture was simulated (Fig. 3.4). The deformation of 40% was considered along x_3 axis. Displacement boundary condition was applied on one end of sample, which was pulled, and the second end was fixed. In order to reduce computation time a moderate number of grain orientations was used to represent the initial crystallographic texture. One FEM element (C3D8R type element with one Gauss point) was considered, which contained a polycrystalline sample of 500 grains with a random crystallographic texture. The total simulation time was set as 0.5 s.

In order to obtain stable solutions by ABAQUS/Explicit solver, the kinetic energy was controlled during calculations. As mentioned in Section 3.3, in a quasi-static process the kinetic energy of the deformed material should not exceed a small fraction (typically 10%) of the internal energy during the whole deformation. The obtained result confirms a very good proportion: the kinetic energy is $10^3 \div 10^7$ times smaller than internal energy (Fig. 3.5). Low values of kinetic energy confirm that the choice of time step and of the simulation time for Explicit solver was correct.

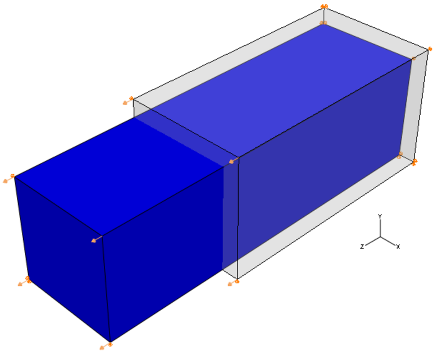

Fig. 3.4. *Geometry of uniaxial tension test.*

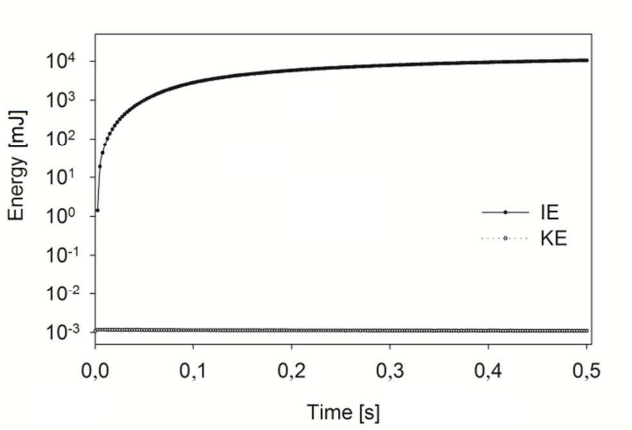

Fig. 3.5. *Variation of* ***internal*** *and* ***kinetic*** *energy vs. calculation time (proportional to deformation). The total simulation time was 0.5 s.*

The tensile f.c.c. textures predicted by FEM+LW model and solely by LW model are compared with experimental texture for α-brass in Fig. 3.6. We observe a good agreement between textures corresponding to two calculation modes as well as between them and experimental data. Two principal texture components, i.e., <111> and <100> fibre orientations, appear in the presented cases.

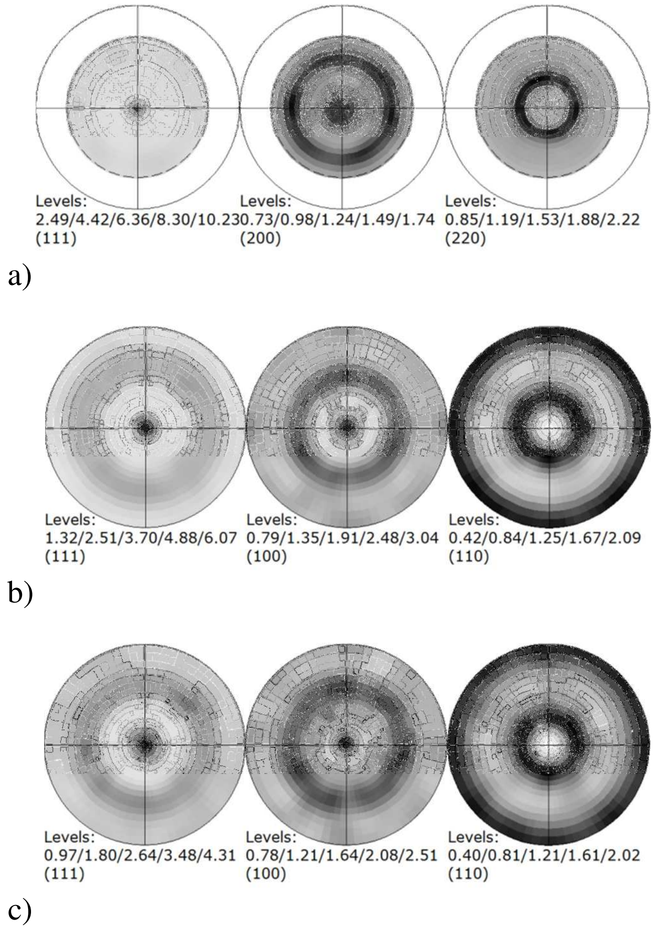

Fig. 3.6. *Experimental and predicted tension textures:*

a) experimental tension test texture of α-brass (30% Zn),

b) tension texture predicted by LW model,

c) *tension texture predicted by FEM coupled with LW model.*

The parameters of ABAQUS and LW model, used in the calculation for polycrystalline α-brass, are listed in Table 3.1.

Table 3.1. *FEM and LW model parameters used in the simulation of the tension deformation of polycrystalline α-brass.*

E [GPa]	ν	ρ [kg/m^3]	slip systems	τ_0 [MPa]	h_{sat} [MPa]	d	τ_{sat} [MPa]	a	L [MPa]
70	0.34	2700	{111}<110>	70	100	1	300	2	270

3.6 Conclusions

The calculation tool basing on FEM, taking into account the crystallographic nature of materials was created (FEM+LW model). Using an example of tension deformation (process with simple geometry) the FEM+LW model was checked. After this positive test the FEM+LW model was used to study a more complex process of AR, for which it is not possible to obtain exact solutions using LW model solely.

Chapter 4

4 Experimental study of microstructure of asymmetrically rolled aluminium and titanium

4.1 Introduction

In this chapter we describe, both qualitatively and quantitatively, the influence of AR process on microstructure evolution in polycrystalline materials. One can find in the literature many evidences (e.g., [56]) that AR can be used as an efficient technique for obtaining fine grain or even ultra-fine grain (UFG) materials. In this sense AR could be considered as some alternative for ECAP[57]. The both methods can be used to deform metals in the severe plastic deformation (SPD) range, but AR process has a higher economic efficiency, can provide large volumes of deformed material and is easy to implement on existing industrial rolling mills. ECAP method is treated as a laboratory method, not useful in the industrial scale. Therefore, our aim was to investigate potential application of AR for the modification of microstructure and resulting properties of materials. We would like to examine whether AR increases the microstructure fragmentation - compared with SR (even if it does not produce UFG microstructure, i.e., a structure with grain sizes between 250 nm and 1 μm). Two polycrystalline materials were chosen in our study: **aluminium (Al 6061 type)** and **titanium (Ti Grade 2).** These two metals, with deferent crystallographic structures (Al: f.c.c. and Ti: h.c.p.) have numerous technological applications, for example in the aerospace and automotive industry (Al, Ti) and in the medical implantology (Ti). In order to check the influence of AR process on the resulting microstructure, several orientation maps were determined using EBSD technique. Grain size, texture, misorientation angle distribution, Kernel average misorientation and average grain orientation spread - were determined by this technique and analysed. X-ray diffraction was also used and it was applied to study crystallographic textures of aluminium after SR and AR processes.

4.2 Geometry of asymmetric rolling process and internal stress distribution

AR is a rolling process in which outer velocities of the upper and lower rolls are different[58][59]. This can be achieved either by selecting different diameters of the rolls rotating with the same angular velocity, or by maintaining the same diameter of both rolls and varying the angular velocity of one of the rolls[60]. Still another possibility consists in imposing different friction coefficients between rolls and a rolled material.

In this work AR was realized using two identical rolls, driven by independent motors and rotating with different angular velocities ω_1 and ω_2. This ensured a wide range of rolling asymmetry. Asymmetry of the process is described by *A* factor (asymmetry ratio), and is defined as the ratio of angular velocities:

$$A = \frac{\omega_1}{\omega_2} \tag{4.1}$$

The scheme of applied asymmetric rolling is shown in Fig. 4.1. The following values of *A* were applied in our experiments: *A*=1.0 in SR, and *A* values between 1.0 and 1.5 - in AR.

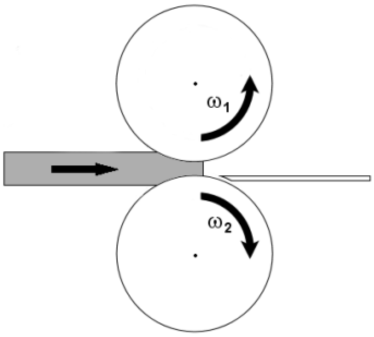

Fig. 4.1. *Scheme of studied asymmetric rolling process: two identical rolls turn with different angular velocities.*

A part of the experimental work, namely AR operations and EBSD measurements, was done in LSPM laboratory, University Paris 13. The experimental laboratory rolling mill (dedicated to AR) developed by J. Gracio and co-workers was used; its detailed description can be found in [61]. The used experimental laboratory mill is shown in Fig. 4.2.

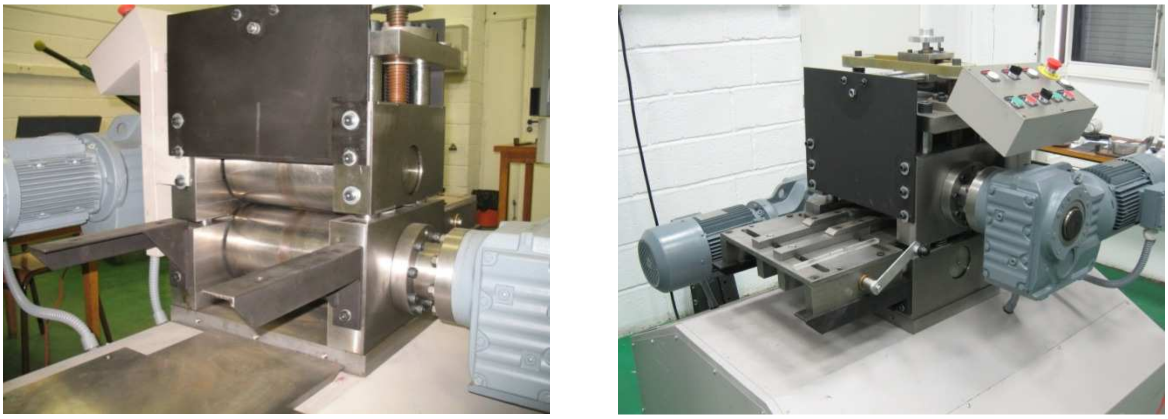

Fig. 4.2. *Experimental laboratory rolling mill used in our experiments (LSPM laboratory, University Paris 13).*

Generally, during AR a strong shear strain is induced inside the material, which can lead to a fragmentation of grain and sub-grain structure. In general, a more fragmented microstructure improves the mechanical strength of materials. AR modifies also crystallographic texture. This rolling technique is also of potential interest for industrial applications, because it reduces the applied rolling forces and torques, and modifies the rolled plate shape[62] and microstructure[63]. Some problems can arise from mill vibrations, wrinkles on the plate surface and from a possible heterogeneity of the product.

The principal difference between SR (A=1.0) and AR (A>1.0) can be expressed by internal stress distribution (i.e., the stress applied during rolling) along the rolling gap. The selected results of the calculated internal stress distribution in the rolling gap for A=1.0, A=1.04 and A=1.15 are shown in Fig. 4.3. This stress distribution was calculated with ABAQUS program for a homogeneous material [A1][A2] (LW model was not included in this case). A characteristic variation of the Σ_{13} shear stress component, occurring in the plane defined by the rolling and normal directions, appears on both surfaces of the asymmetrically rolled sample. Let us consider the top surface (Fig. 4.3a). For the angular velocity ratio A=1.0 the sign of the shear component Σ_{13} is mainly positive. When the angular velocity ratio increases, the negative part of the shear component becomes smaller, and for the velocity ratio of A=1.15 - this shear stress component is solely positive. Similarly, in the bottom surface layer, the Σ_{13} component tends to have a predominantly positive value, with an increasing ratio of angular velocity A (Fig. 4.3b). In the central sample layer (Fig. 4.3c), the behaviour of this component is different for the two types of rolling. During SR, namely A=1.0, Σ_{13} is practically zero throughout the rolling pass, while during AR a small variation of this component exists. It should be mentioned that the Σ_{13} stress component is mainly responsible for *sample bending* and *texture rotation*, which will be described in the further text.

The distributions of normal stress components, in other words, Σ_{33}, Σ_{11} and Σ_{22}, differ slightly between SR and AR and also between two surface layers (Figs. 4.3 a and b). Contrary to this, a more characteristic difference between SR and AR appears in the central layer. We note a decrease of the absolute value of the normal stress component, Σ_{33}, in the central layer for $A = 1.15$, as compared with $A=1.0$ and $A=1.04$ (Fig. 4.3 c). This reduction of the normal stress component during AR (and, consequently of the normal force) is advantageous for the rolling mill durability.

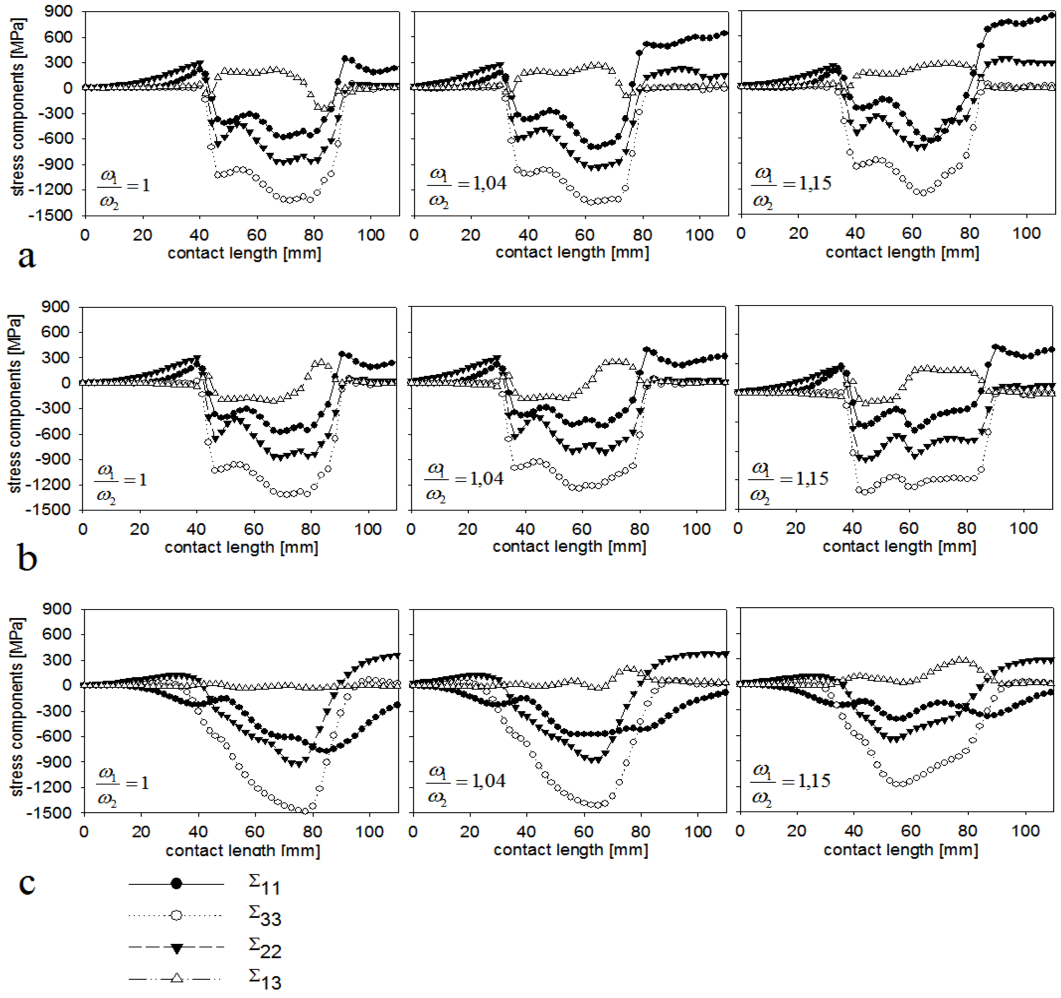

Fig. 4.3. *Stress components for symmetric and asymmetric rolling along the contact length: a) top surface, b) bottom surface, c) centre of the sample. Results for A= 1.0, A= 1.04 and A=1.15 are shown. Calculation was done with ABAQUS program for isotropic material for rolling reduction of 25% (*[A1][A2]*).*

A more complete approach to the problem of stress distribution in a rolled material was done using ABAQUS with implemented LW crystallographic model (MES+LW model) and it is presented in Chapter 5.

4.3 EBSD analysis

The EBSD technique was applied to study the influence of AR process on resulting microstructure. Full crystallographic orientation data were obtained from automatically indexed EBSD patterns collected on Cambridge S360 (W-GUN) equipment and on Zeiss Supra 40VP Scanning Electron Microscope (in LSPM laboratory) – Fig. 4.4. All analysis were performed with OIM (Orientation Imaging Map) TSL software. The following analyses were performed using EBSD technique: topological maps (they give information about topology and orientations of grains), average grain size, average grain orientation spread (it gives information about a typical spread of orientations inside grains), Kernel Average Misorientation - KAM (it characterizes structure of sub-grains), misorientation angle distribution (very useful to analyze twin boundaries and their fractions) and texture characterisation (textures were recalculated from the measured orientation maps).

Fig. 4.4 *Scanning Electron Microscope (SEM) equipped with EBSD system: (a) Cambridge S360 (W-GUN) and (b) Zeiss Supra 40VP used in our experiments (LSPM laboratory, University Paris 13).*

The grain size was expressed in the present work as the *grain area*. We prefer this measure than *grain diameter*, because very often grain shapes are irregular. The *grain definition* was based on two assumptions: a) misorientation angle characteristic for a grain boundary is equal at least to 15^0 and, b) a grain contain at least 5 measurement points. Two definitions of the average grain area were considered. In the first approach (named *number*) the average grain area is calculated as the arithmetic average:

$$\langle S \rangle_{number} = \frac{1}{N} \sum_{i=1}^{N} S_i \tag{4.2}$$

where: S_i is the area of the *i-th* grain and N is the number of grains in a map. In the second definition (named *area*) the grain areas are weighted with their fractions in a map. According to the OIM TSL software documentation it is calculated as:

$$\langle S \rangle_{area} = \sum_{i=1}^{N} v_i \, S_i \tag{4.3}$$

where: v_i is the area fraction of the *i-th* grain in a measured map: $v_i = S_i / S_{total}$.

In order to study grain and twin boundaries the *misorientation angle,* characterizing the distribution of grain boundary misorientations, was analysed. Misorientation angles, between neighbouring points were grouped into low angle boundaries (with misorientations between 2^0 and 15°) and high angle boundaries (with misorientations higher than 15°). The analysis of high angle boundaries was useful in the examination of twin boundary fractions.

An important parameter is the *average grain orientation spread* (AGOS); it characterizes the internal grain structure. According to the OIM TSL software documentation it is calculated as follows. For each grain its average orientation (*O*) and next the average misorientation (*M*) between all its points and the orientation *O* is calculated. Finally, the average grain orientation spread is calculated as the average value of *M* over all grains.

The internal sub-grain structure can be characterized using KAM. For a given point, the average misorientation with all its nearest neighbours is calculated, under the condition that these misorientations do not exceed a given value, usually set at 15^0. Next this misorientation is averaged over all measurement points. Consequently, the misorientations associated with grain boundaries are excluded in this averaging procedure. It was shown that KAM parameter is a good tool for determining the degree of deformation [64] and even more efficient for determining the degree of recrystallization during interrupted annealing treatments [65].

The above two parameters (AGOS and KAM) characterize the internal grain and sub-grain structure (and their fragmentation). There is, however, a principal difference between them. AGOS tells us about the average level of misorientation inside grains with respect to their average orientations. In contrast, KAM characterizes the average level of local misorientations.

4.4 Properties of asymmetrically rolled aluminium

4.4.1 Experimental procedure

The selected material was the 6061 type Al alloy (containing 2.4% Mg). The initial size of the samples was 60x30x2.9 mm^3. Rolling was performed in one pass till the thickness reduction of 36%. The diameter of both rolls was 180 mm. In the reported experiments, the rotation rate of the bottom roll was kept constant at 10 rpm and that of the top roll was imposed to be 10, 11, 13 and 15 rpm. Under these conditions, the asymmetry ratio A was equal to 1.0, 1.1, 1.3 and 1.5, respectively. No lubrication was applied to the rolls, but the surfaces of rolls were rubbed with a silicon carbide paper along the rolling direction in order to increase friction between a sample and the rolls. Two sets of samples were examined: samples after deformation (rolled to 36% reduction) and samples after deformation and annealing in the air atmosphere at 450°C during 15 min (the temperature and time were chosen basing on experimental curves of hardness vs. annealing time at constant temperatures). The examination of crystallographic texture and of microstructure was performed for two near-surface layers of the thickness about 20 μm (i.e., for the top surface and the bottom surface layers) and also for the centre layer of the rolled bar. Before examination the samples were mechanically polished with silicon carbide paper down to grade 4000 and then electro-polished in the solution A2 produced by Struers. The evolution of the crystallographic texture for deformed sample was examined using X-ray diffraction. On the other hand, EBSD technique was used to determine the microstructure in SR an AR samples and also the crystallographic texture in the annealed samples. In the case of deformed aluminium samples the Cambridge S360 (W-GUN) scanning electron microscope was used. For each sample a map of 700x400 μm size was measured with the step of 1 μm. For the samples annealed after deformation the Zeiss Supra 40VP scanning electron microscope was used and the maps of the size of 650x650 μm^2 with the step of 1.2 μm were determined. No cleanup procedure was applied in the obtained maps. The sole applied filtering procedure consisted in excluding grains containing less than 5 points.

4.4.2 Texture evolution

The determined ODFs were presented as plots at constant φ_2 sections in the Euler angles space defined by three angles: φ_1, Φ, and φ_2 [66]. Taking into account the crystal and sample symmetries, the following ranges of Euler angles were used: $\varphi_1 \in [0^0, 360°]$, $\Phi \in [0^0, 90°]$ and $\varphi_2 \in [0^0, 90°]$, respectively. Three characteristic sections were selected to represent the main features of the measured textures, namely the $\varphi_2=0^0$, $\varphi_2=45^0$ and $\varphi_2=65^0$ sections. The principal f.c.c. rolling textures components, defined by Euler angles and Miller indices are shown in Fig. 4.5 a.

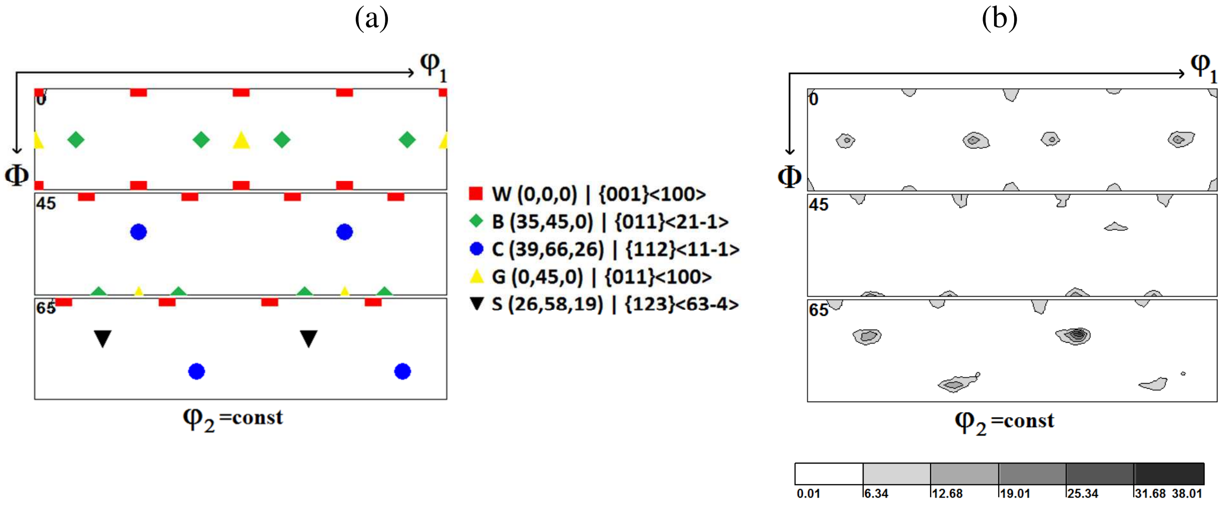

Fig. 4.5. *(a) Ideal orientations of f.c.c. rolling textures, (b) initial crystallographic texture of 6061 aluminium sample;* φ_2 *sections are shown.*

The measured crystallographic texture of the initial material (aluminium 6061) is shown in Fig. 4.5 b. It is very sharp and contains Brass (*B*), Cubic (*W*), *S* and *C* orientations. This material was next rolled symmetrically and asymmetrically, applying the following degrees of asymmetry: A=1.0, A=1.1 and A=1.5. The measured pole figures were determined in three regions of the rolled samples: in the top, bottom and central layers, using X-ray diffraction (measurements were done in LSPM laboratory, University Paris 13). Starting from the measured poles figures the three-dimensional ODFs were calculated with WIMV method using popLA calculation package [53]; they are shown in Fig. 4.6.

The texture of SR sample (A=1.0, Fig. 4.6 a) contains the following components: Cubic - *W* (dominating one), *B*, *C* (weak) and traces of *S* and *G* orientations. Characteristic effects appearing during SR and AR can be followed examining *B* (Brass) component and they are visible in the $\varphi_2=0^0$ ODF section. In can be noted that in the central layer of SR material all equivalent Brass component maxima lie on the horizontal red line, drawn at $\Phi=45^0$ (Fig 4.6 a - centre). In the surface layers of SR material one observes delicate shifts of these maxima. In the top layer the first two maxima (corresponding to lower φ_1 values), which belong to *B* orientation, are shifted up and the next two maxima - are shifted down (Fig. 4.6 a - top surface). The opposite shifts appear in the bottom layer of the material (Fig. 4.6 a - bottom surface).

The opposite behaviour is observed in AR materials. In the cases of A=1.1 and A=1.5 (Fig. 4.6 b and c) the sequence of shifts of *B* maxima is the same in three examined layers (the first two maxima are shifted up and the two following ones - are shifted down). The shifts are small for A=1.1 and are more pronounced for A=1.5. Therefore, we conclude that a character of texture modification is the same in three layers and, consequently, that texture becomes homogeneous after AR process.

The observed shifts of texture maxima result from respective rotations of texture around the transverse direction (TD), and are caused by the action of internal stress component Σ_{13} (these rotations are discussed in more details in Chapter 5). The signs of shifts and of corresponding texture rotations can be explained by the variation of the Σ_{13} stress component across the sample thickness, shown in Fig. 5.4 in Chapter 5 (the quoted stress distribution was calculated with FEM+LW model for aluminium sample). During SR the sequence of positive and negative values of Σ_{13} component has opposite character on the top and bottom surface (Fig. 5.4, case of A=1.0), while with increasing the degree of asymmetry (A=1.3) the stress distribution becomes nearly homogeneous across the sample thickness. This explains the same sign of the shift of texture maxima in three material layers after AR. One can also note that after AR, with A=1.5, *B* (Brass) component, as well as *C* (Copper) and *S* components are distinctly reinforced at the expense of the Cube (*W*) component, which practically disappeared.

The main conclusion from texture examination is that textures become homogeneous (across the sample thickness) after AR, which is not the case of SR !

(a) *A*=1

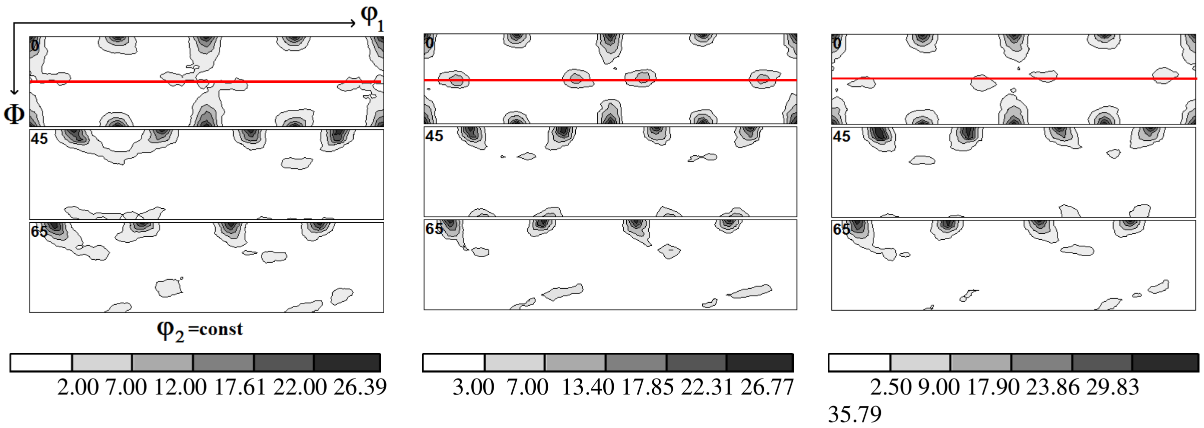

(b) *A*=1.1

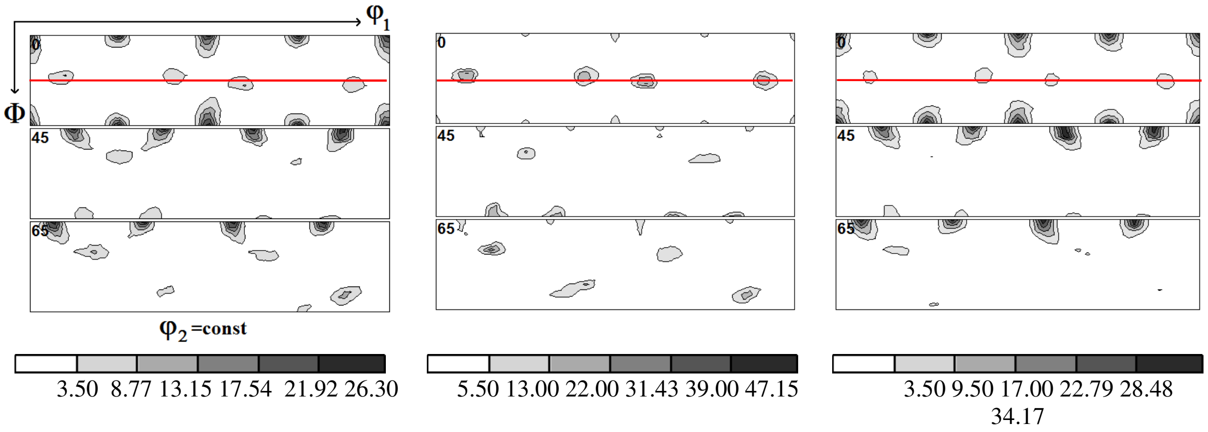

(c) *A*=1.5

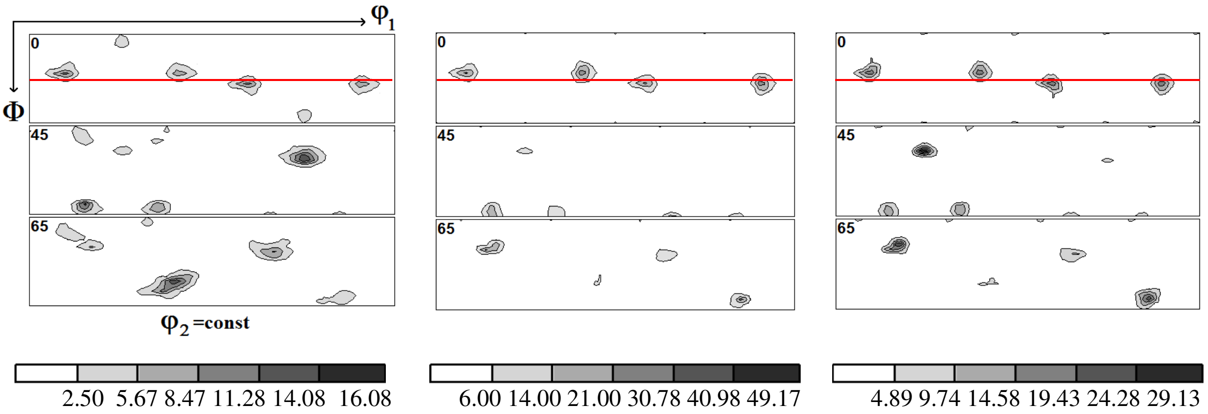

Fig. 4.6. *Measured textures for the rolled aluminium samples. ODFs of the top, centre and bottom surface layers of the sample are shown. Results for the rolling reduction of 36 % and for three values of the asymmetry ratio A: (a) A=1.0; (b) A=1.1; (c) A=1.5, are shown.*

Some of the rolled aluminium samples were next annealed (recrystallized). The annealing textures from the centre layer, corresponding to three degree of rolling asymmetry

A: 1.0, 1.3 and 1.5, are shown in Fig. 4.7. Texture of each sample was represented by ODF calculated basing on crystal orientations from EBSD maps. In the smoothing procedure the Gaussian functions with half-widths of 5^0 were attributed to all crystal orientation and the resulting ODF was calculated as the sum of these functions. The final ODF was obtained using the series expansion method up to the range of 22, according to Bunge formulation [66]. The ODFs of the annealing textures were represented in the same cross-sections as previously. The main ideal orientation in these textures is Cube component (W); it appears for three considered values of *A* ratio - Fig. 4.7. Some dispersed secondary orientations also appear, especially in the textures for *A*=1 and *A*=1.5. However, we do not observe any systematic influence of rolling asymmetry ratio, *A*, on the annealing textures.

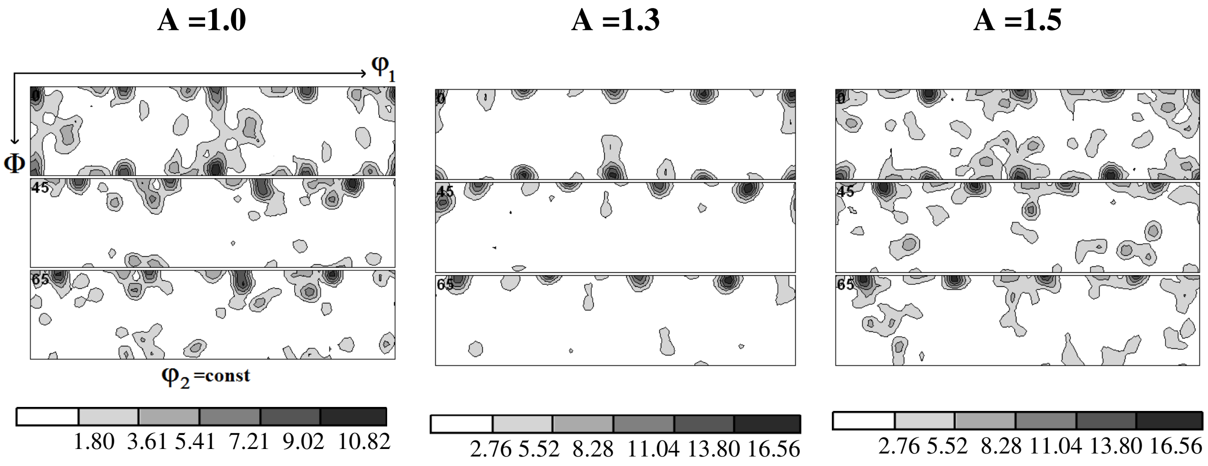
A =1.0

A =1.3

A =1.5

Fig. 4.7. *Measured ODFs for centre layers of aluminium samples rolled to 36% reduction and then annealed at 450 ^{0}C during 15 min. Results for three values of the asymmetry ratio are shown: A=1.0, A=1.1 and A=1.5*

4.4.3 Microstructure characteristics

All EBSD maps presented in this thesis show the topology of orientation distribution of the normal direction, ND, in the crystal reference frame (i.e., the [001] inverse pole figure is used). Different orientations are visualized by a conventional attribution of colours inside the basic triangle of the inverse pole figure (this basic triangle is attached to EBSD maps).

The EBSD maps measured for the initial material and for the rolled aluminium samples (with the rolling asymmetries: *A*=1, *A*=1.1, *A*=1.5) are presented in Figs. 4.8 and 4.9.

The presented maps correspond to the centre layer of the material, as it represents a major part of the material volume. Therefore, all results presented in this section correspond to the centre material layer. The maps were measured on the RD-ND surface of the sample (RD - rolling direction). With increasing the degree of asymmetry a significant change of the microstructure was observed. Compared to SR, AR leads to a notable refinement of the microstructure consisting of the appearance of elongated grains (or bands) with the extended sub-grain structure (compare maps for *A*=1.5 and *A*=1.0 in Fig. 4.9).

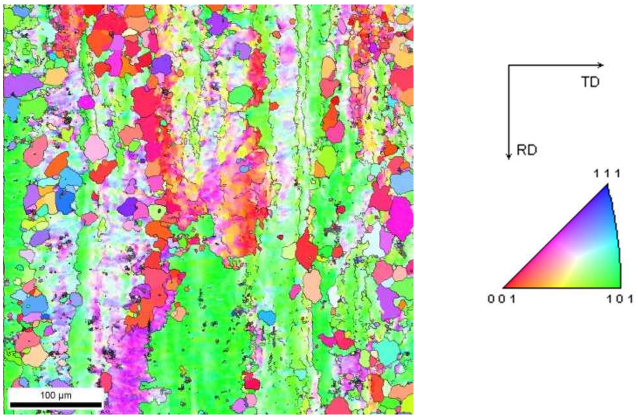

Fig. 4.8. *EBSD map for the centre layer of the initial aluminium sample. Size of the map is: 450x450 μm^2.*

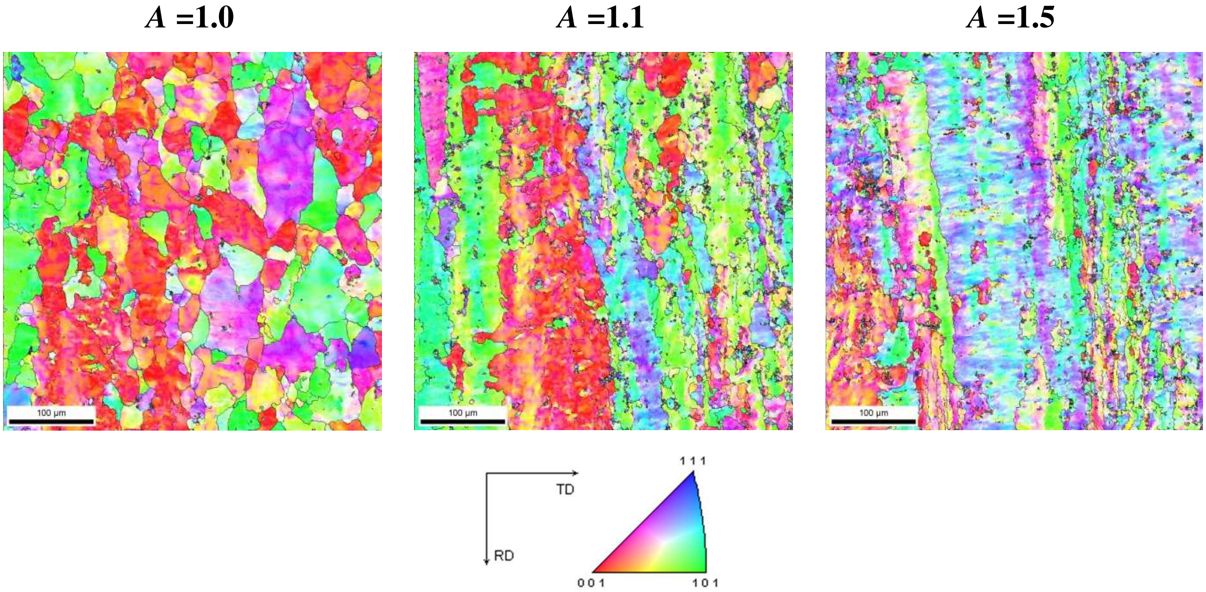

Fig. 4.9. *EBSD maps centre layers of aluminium samples rolled symmetrically (A =1.0) and asymmetrically (A=1.1, A=1.5); rolling reduction was 36 %, Size of the maps is: 450x450 μm^2.*

Basing on the measured EBSD maps and using OIM TSL software the statistic analyses were made. The microstructure parameters like: average grain size, AGOS and KAM were calculated and are presented in Fig. 4.10. The average grain area versus *A*, calculated using two averaging methods: *number* and *area*, is presented in Fig.4.10a. For the *number* definition (arithmetic average) we observe a radical decrease of the average grain area versus *A*, especially when passing from *A*=1 to *A*=1.1. Contrary to this, the second averaging definition (*area*) gives an increasing relation of the average grain area versus *A*. This result can be interpreted as follows: AR produces important number of small grains (this is confirmed by the *number* average), but overall *weighted* grain area becomes larger (and this is reflected in the *area* average). Basing on this result, it is difficult to conclude that AR leads to a grain refinement for this deformation. However, we note that with increasing the degree of asymmetry (*A*) the internal grain structure becomes more fragmented (e.g., by an intensive sub-grain formation). This effect is confirmed by a visible increase of KAM versus *A* - Fig. 4.10 c (also a very delicate increase of AGOS versus *A* appears - Fig. 4.10 b).

It should be recalled that the present EBSD were determined on the RD-TD sample surface. It is less favourable than ND-RD surface for measurements in the case of rolled materials. In the future, systematic measurements should be also done on the ND-RD sample surface, where much better statistics of grain distribution is available.

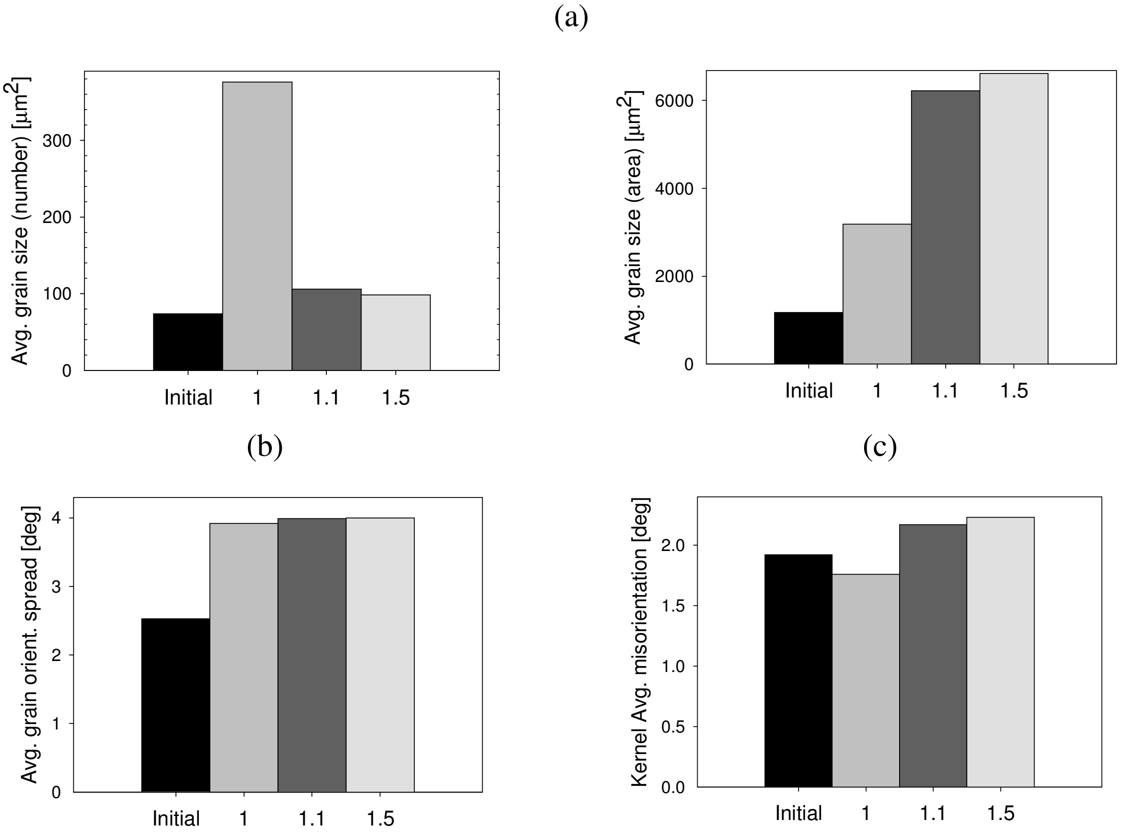

Fig. 4.10. *Influence of the rolling asymmetry (A=1.0, A=1.1 and A=1.5) on microstructure parameters for aluminium sample: a) average grain area (μm^2) obtained with two averaging methods ('number' and 'area'), b) average grain orientation spread, c) Kernel average misorientation. Results for centre layers of aluminium samples rolled to 36% reduction are shown.*

As already mentioned, selected aluminium samples rolled to 36% reduction were next annealed at 450 ^{0}C during 15 min. Corresponding EBSD maps determined in centre layers of the samples corresponding to A=1, A=1.3 and A=1.5 are shown in Fig. 4.11.

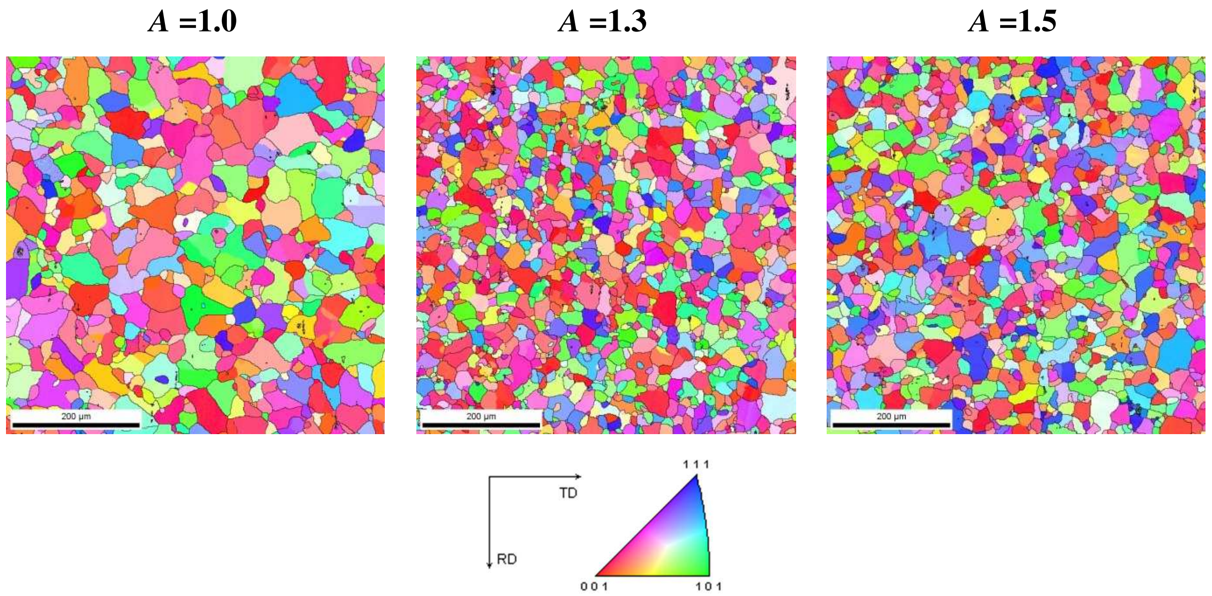

A =1.0 **A =1.3** **A =1.5**

Fig. 4.11. *EBSD maps for centre layers of aluminium samples rolled to 36 % reduction and annealed at 450 ^{0}C during 15 min. Maps for symmetrically rolled (A =1.0) and asymmetrically rolled (A=1.3, A=1.5) samples are shown. Size of the maps is: 600x600 μm^2.*

Already a visual inspection shows that *AR annealed* samples have *finer grain structure* than SR ones. This is confirmed by a comparison of the average grain area for SR and AR samples presented in Fig. 4.12. We observe much smaller grain size after AR than after SR. This results is obtained using both averaging methods: *number* and *area*.

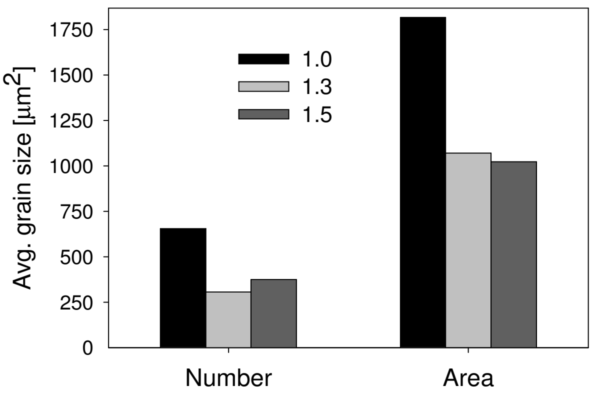

Fig.4.12*. Influence of the rolling asymmetry (A=1, A=1.3 and A=1.5) on the average grain area (μm^2) obtained with two averaging methods ('number' and 'area') for aluminium rolled to 36% reduction and annealed at 450 ^{0}C during 15min. EBSD measurements were done in centre material layers.*

4.5 Properties of asymmetrically rolled titanium

4.5.1 Experimental procedure

The second examined material was commercially pure titanium (Ti Grade 2). The initial samples of the size 60x30x8 mm^3 were prepared for rolling. The same laboratory rolling mill was used as in the case of aluminium (available in LSPM laboratory, University Paris 13). No lubrication was applied to the rolls. The surfaces of the rolls were modified by rubbing them with a silicon carbide paper along the rolling direction in order to increase the friction between the rolls and a material.

Two sets of samples were examined: after low and medium deformations (rolling reduction of 20% and 40%) and after higher deformation and annealing in the air atmosphere at 550°C during 1 hour (rolling reductions of 60%, 70% and 80%). The recrystallization time was estimated by measuring hardness vs. annealing time (at constant temperatures). The aim of annealing was to achieve the recrystallized state.

Table. 4.1 *Number of passes in which appropriate rolling reduction were reached.*

Rolling reduction	Number of passes
20%	4
40%	8
60%	11
70%	13
80%	15

The final rolling reductions were obtained in several number of passes (Table 4.1). It was not possible to reach a required reduction in one rolling pass due to a high hardness of titanium and an insufficient power of the laboratory rolling mill. The rotation rate of the bottom roll was kept constant at 10 rpm and that of the top roll was imposed to 10, 13, 15 rpm (15 rpm was a maximum angular velocity of the laboratory rolling mill). Consequently, three degrees of rolling asymmetry (A=1.0, A=1.3, A=1.5) were available.

The EBSD technique was used for microstructure and crystallographic texture measurements in SR and AR samples. Before examination the samples were mechanically polished with silicon carbide paper down to grade 4000 and then electro-polished using the

A3 Struers solution. The EBSD measurements for low and medium deformation materials (20% and 40% rolling reductions) were done using Scanning Electron Microscope Zeiss Supra 40VP. For these samples the maps of the size of 350x300 μm^2 with the step of 0.3 μm were determined. For highly deformed (60%, 70% and 80% rolling reductions) and annealed samples the Cambridge S360 (W-GUN) scanning electron microscope was used. For these samples maps of the size of 400x200 μm^2 with the step of 0.5 μm were determined. The sole applied filtering procedure consisted in excluding grains containing less than 5 points.

4.5.2 Texture evolution

The initial texture of the examined titanium sample is shown in Fig. 4.13, where the $\varphi_1=0^0$ ODF section is presented (in the case of h.c.p. materials it is convenient to use this cross-section; Φ and φ_2 vary in the ranges [0^0, 90^0] and [0^0, 60^0], respectively).

Texture modifications of titanium are discussed on the example of the material rolled to 40% reduction with two degrees of asymmetry: A=1.0 and A=1.3. The presented ODFs were calculated from crystal orientations (determined by EBSD technique) in the same way as it was described for the annealed aluminium samples (section 4.4.2).

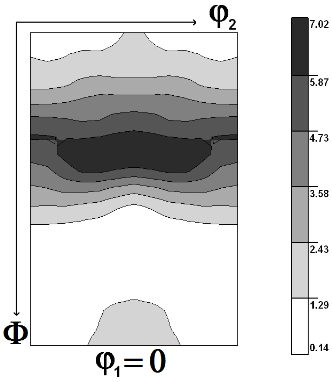

Fig. 4.13. *Initial crystallographic texture of the examined polycrystalline titanium; $\varphi_1=0^0$ ODF section is shown.*

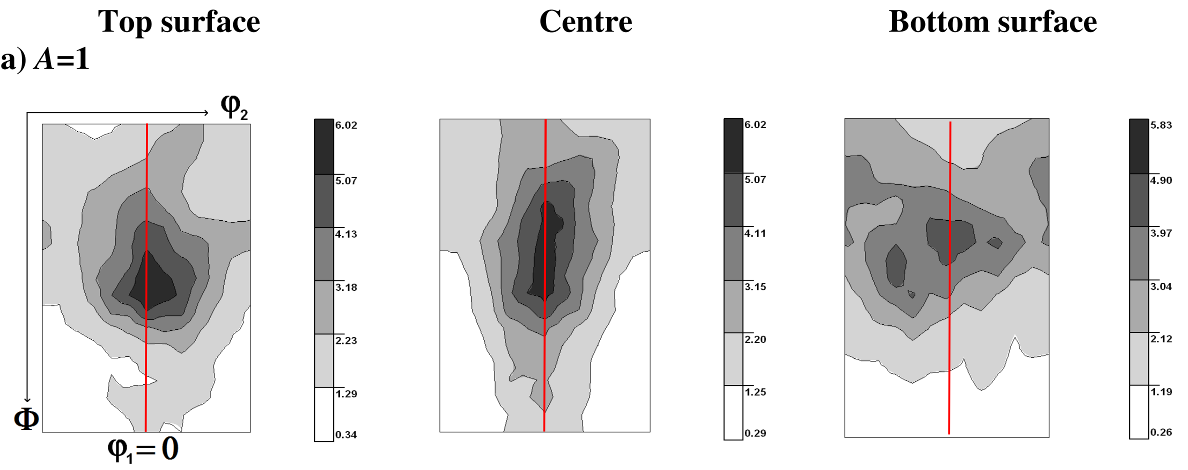

(a) A=1

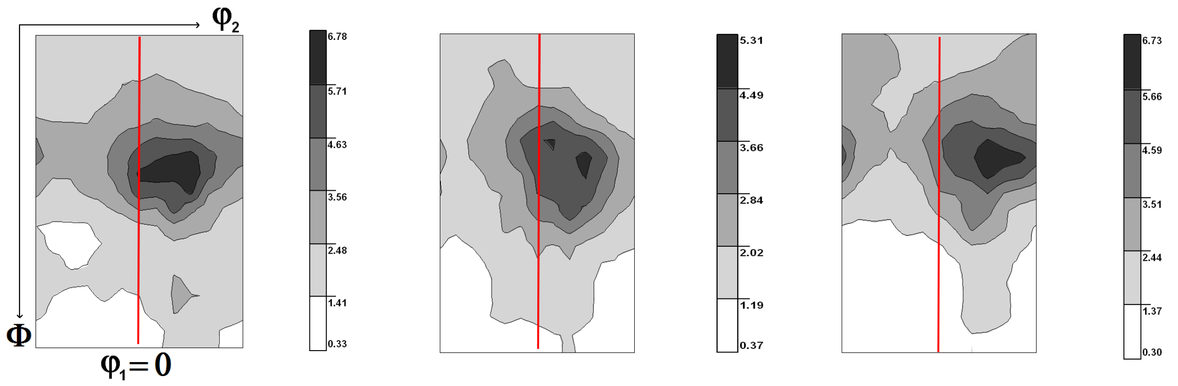

(b) A=1.3

Fig. 4.14. *Textures of titanium rolled to 40% reduction in three sample layers (top, centre, bottom) for: (a) A=1.0, (b) A=1.3. The* $\varphi_1=0^0$ *ODF sections are shown.*

The measured textures for the top, centre and bottom layers after SR (A=1.0) are shown in Fig. 4.14 a. In the centre layer the texture maximum is located at $\varphi_2=30^0$, similarly like in the initial sample (i.e., in the centre of section with respect to φ_2 coordinate). In contrast, textures of the surface layers show characteristic shifts of the 'centre of gravity' of the main maximum: in the top surface the maximum is shifted towards a higher φ_2 angle ($\varphi_2 > 30^0$), but in the bottom surface layer it is shifted towards a lower φ_2 angle ($\varphi_2 < 30^0$).

The experimental textures after AR for A=1.3 (Fig.4.14 b), show a different behaviour than those after SR: in the three considered layers the rolling texture maxima are shifted towards higher φ_2 angles ($\varphi_2 > 30^0$). The observed shifts of rolling texture maximum in three considered layers can be explained by the distribution of Σ_{13} internal stress component (Fig. 5.25 in Chapter 5). During SR the sequence of positive and negative values of Σ_{13} component is opposite in the top and bottom surface layers (Fig. 5.25 - A=1.0), while with increasing degree of asymmetry (Fig. 5.25 - A=1.5) - the stress distribution becomes nearly homogeneous across the sample thickness. This explains the same sign of shifts of texture maximum in three material layers after AR (Fig. 4.14 b).

Besides of rolling textures, also the annealing textures were measured. The crystallographic textures of the sample rolled to 40% reduction and annealed at 550 ^{0}C during 1 h, in three examined sample layers (for A=1.3) - are shown in Fig. 4.15. It is visible that the discussed shift of texture maxima in AR sample persisted after annealing. Therefore, we conclude that AR modifies both rolling and recrystallization textures.

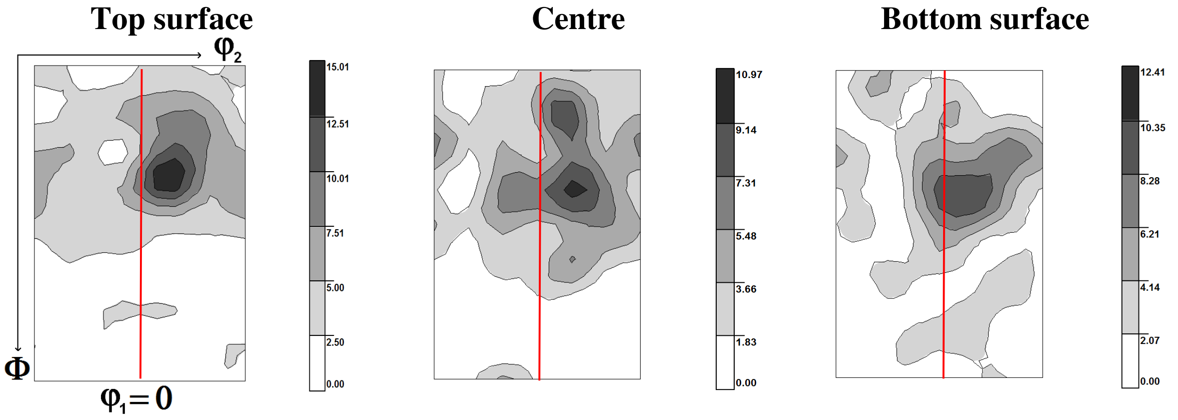

Fig. 4.15. *Textures of titanium rolled to 40% reduction and annealed during 1 h at 550 ^{0}C in three sample layers (top, centre, bottom) for A=1.3. The $\varphi_1=0^0$ ODF sections are shown.*

Finally, we can conclude that AR leads to texture homogenisation across the thickness of the titanium samples. The same effect was found in the case of the rolled aluminium samples, as discussed in Chapter 4.

4.5.3 Microstructure characteristics

The microstructure characteristics of rolled and annealed titanium samples were determined using EBSD technique. The statistical analyses were made and microstructure parameters like: average grain size, AGOS, KAM and misorientation angle distributions were determined. All maps were measured on the RD-ND surface of the sample (differently than in the case of aluminium, where the RD-TD surface was examined). In this section we present EBSD maps and related microstructure parameters for centre sample layers (they are representative for a huge part of the material volume). The EBSD orientation maps represent distributions of ND, or [001] sample direction, in the crystal reference frame (inverse pole figure). The measurements were done for titanium samples rolled to 20% and 40% reductions and for the samples deformed to higher deformations (60%, 70%, 80% rolling reductions) and then annealed.

A regular equiaxed microstructure is characteristic for the initial material as shown in Fig. 4.16. The EBSD maps for rolled titanium (20% and 40% reductions), corresponding to three degrees of asymmetry: *A*=1.0, *A*=1.3 and *A*=1.5, are shown in Fig. 4.17 and 4.18.

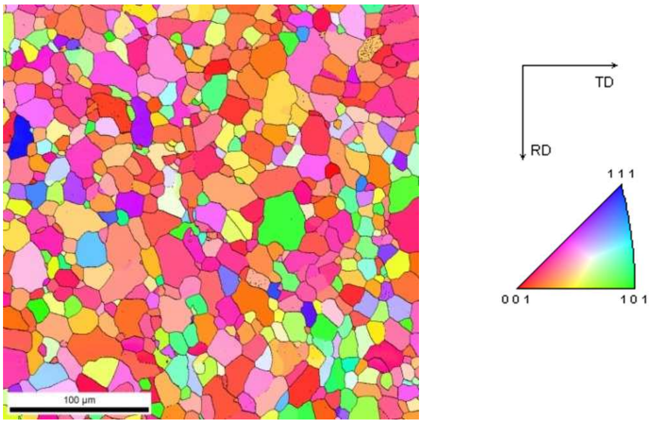

Fig. 4.16. *EBSD map for the centre layer of the initial material (polycrystalline titanium - grade 2). Size of the map is: 300x300 µm^2*

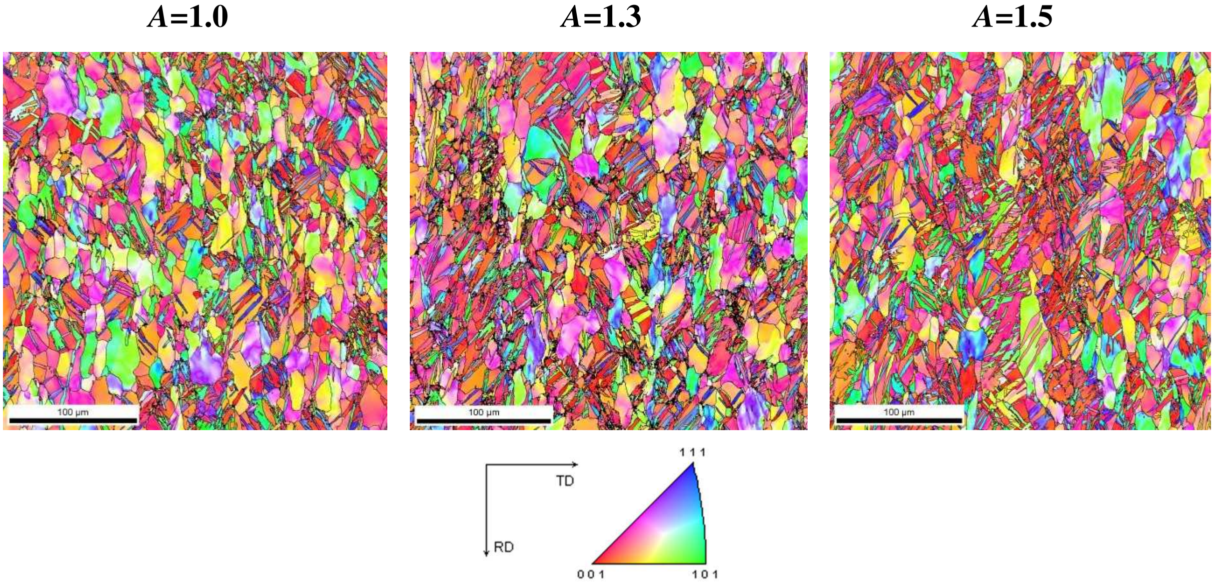

Fig. 4.17. *EBSD maps for centre layers of titanium samples. Material was rolled to* ***20 %*** *reduction with three degrees of asymmetry: A=1.0, A=1.3 and A=1.5. Size of the maps is: 300x300 µm^2.*

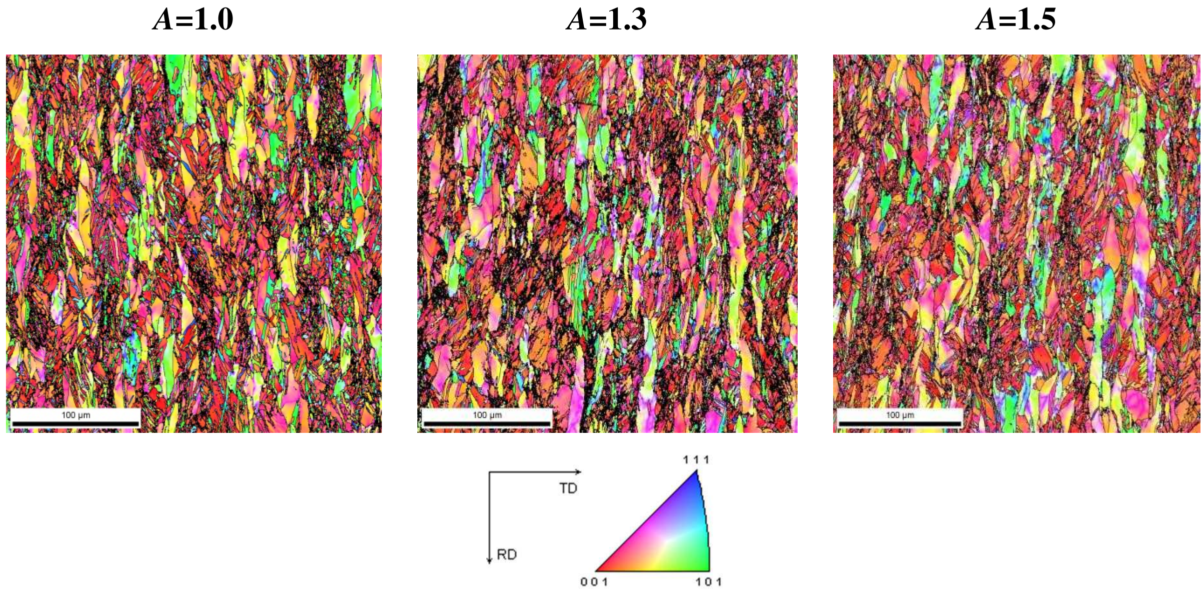

Fig. 4.18. *EBSD maps for centre layers of titanium samples. Material was rolled to* ***40 %*** *reduction with three degrees of asymmetry: A=1.0, A=1.3 and A=1.5. Size of the maps is: 300x300 μm^2.*

The rolling deformation of low and medium levels (20% and 40%) produced heterogeneous microstructures. We observe elongation of majority of grains along RD (vertical direction on the map) and fragmentation of some grains as a result of twinning. The occurrence of twins was observed, especially in the sample rolled to 20% reduction - Figs. 4.17 and 4.19. Grains with and without deformation twins can be clearly identified in this material. In the range of medium deformations (40% rolling reduction) - Fig. 4.18 - the grain structure is still more distorted and a lower fraction of twins is observed compared with the material rolled to 20% reduction.

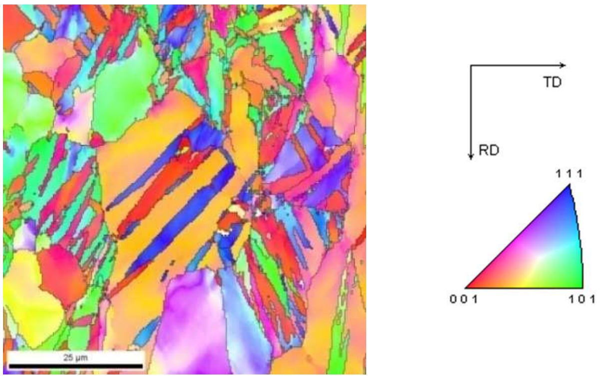

Fig. 4.19. *EBSD map for the centre layer of titanium sample rolled symmetrically to 20 % reduction. The twinned parts of grains are blue. Size of the map is: 70x70 μm^2*

In order to identify twinning systems, which were activated during deformation, the misorientation angle distributions were examined (for high angles, i.e., for $\omega > 15^0$). Such the distributions, calculated from EBSD data, for titanium symmetrically rolled to the reductions of 20% and 40% are shown in Fig. 4.20. In this figure, for comparison, also the misorientation distribution corresponding to a random texture is shown; this is so called MacKenzie plot. Three misorientation angle peaks for the rolled titanium samples are observed in the positions: ~42, ~65^0, and ~85^0. Two of them are associated with twin boundaries. It can be seen from Table 4.2 that the boundary with 64.62^0 misorientation around $\langle 10\bar{1}0\rangle$ axis corresponds to $\{11\bar{2}2\}\langle\bar{1}\bar{1}23\rangle$ twins (called ***compressive twins***) and the boundary with 84.78^0 misorientation around $\langle 2\bar{1}\bar{1}0\rangle$ axis corresponds to $\{10\bar{1}2\}\langle\bar{1}011\rangle$ twins (called ***tensile twins***). Other types of twins reported in the literature for h.c.p. structure were not observed in the studied material.

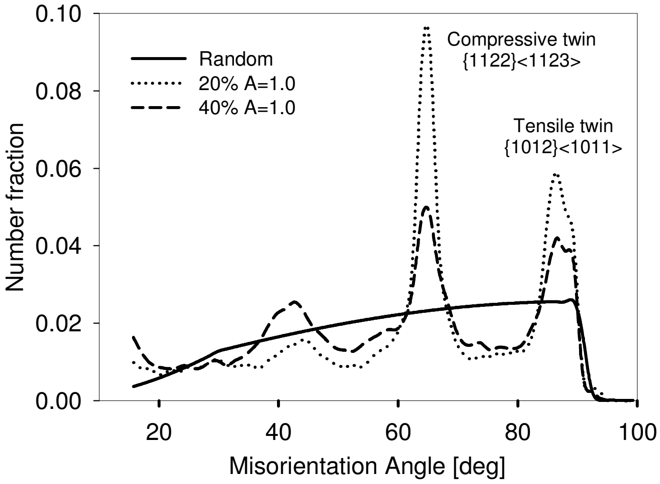

Fig. 4.20*. Distribution of misorientation angle for titanium samples rolled symmetrically (A=1.0) to the reductions 20% and 40%. Also the misorientation distribution corresponding to a random texture is shown.*

We note that the peak corresponding to compressive twins is almost two times higher than the peak for tensile twins in the case of 20% rolled sample. This indicates that compressive twins are dominating in the range of low level deformation (20% rolling reduction). In contrast, for 40% reduction the two twin peaks (of tensile and compressive twins) have comparable heights and they are distinctly lower than for 20% . Therefore, we conclude that a fraction of twinned volume decreases with the degree of deformation. The same effect is reported in [67]. In the quoted work the two following conclusions are presented: a) for low to intermediate rolling reductions (≤40%) the predominant mechanisms are slip and twinning; for higher deformation (>40%) the main mechanism is slip.

Table.4.2. *Misorientation angles θ and directions associated with two twin families; data taken from* [68]**.**

Misorientation angle θ around $\langle uvtw \rangle$	**Twin system**
64.62^0 $\langle 10\bar{1}0 \rangle$	Compressive $\{11\bar{2}2\}\langle \bar{1}\bar{1}23 \rangle$
84.78^0 $\langle 2\bar{1}\bar{1}0 \rangle$	Tensile $\{10\bar{1}2\}\langle \bar{1}011 \rangle$

The influence of rolling asymmetry (A) on misorientation angle distribution was also examined. The distributions for SR (A=1.0) and AR (A=1.3, A=1.5) samples, deformed to 20% and 40%, are shown in Fig. 4.21. We analysed again the peaks in positions of ~65^0, and ~85^0, corresponding to the compressive and tensile twins. In both cases (20% and 40%) we do not observe a significant effect of the rolling asymmetry on the intensity of characteristic peaks. The only small effect is that in the case of 20% deformation AR slightly increases the fraction of tensile twin, while in the case of 40% deformation AR slightly decreases the fraction of compressive twins. Otherwise, it is hard to find a distinct relation between the degree of rolling asymmetry and the level of twinning activity. In contrast, as already stated above, the fraction of twins distinctly decreases with increasing deformation.

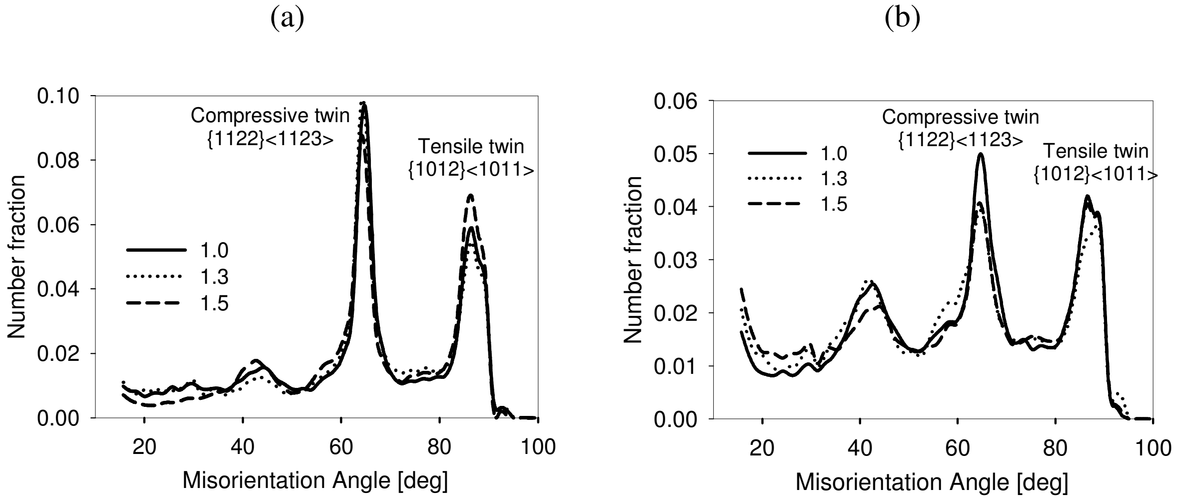
(a) (b)

***Fig. 4.21**. Distribution of misorientation angle for titanium samples rolled to the reductions of 20% (a) and 40% (b). Results for three degrees of rolling asymmetry: A= 1.0, A= 1.3, A= 1.5, are presented.*

In order to describe quantitatively the impact of SR and AR on material properties, the basic microstructure parameters were calculated using OIM TSL software. The average grain size for the initial and SR material (20% and 40%), calculated with two averaging procedures (*number* and *area*), is shown in Fig. 4.22. In both cases a distinct grain refinement is observed with increasing deformation.

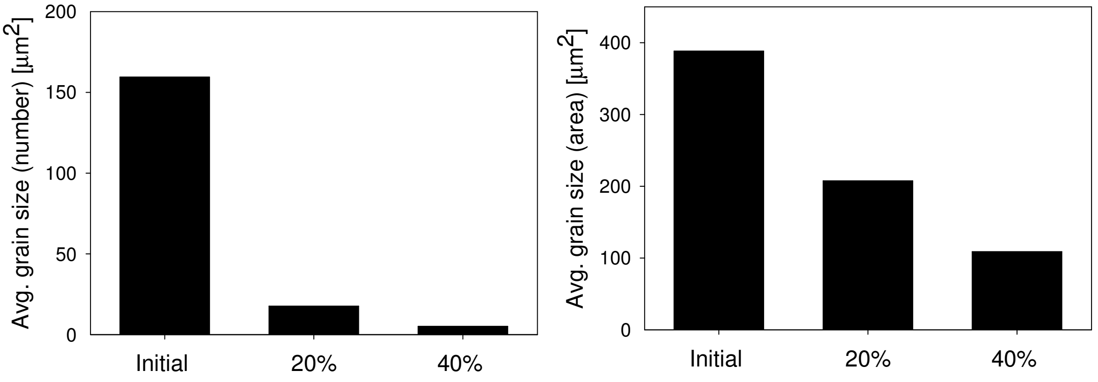

***Fig. 4.22**. Grain area expressed in μm^2 for the initial sample and for 20% and 40% symmetrically rolled samples (A=1.0) calculated using two averaging procedures:' number' and 'area'. Results for the centre sample layers are shown.*

On the other hand, in some examined cases a grain refinement was observed with increasing rolling asymmetry. A good example is shown in Fig. 4.23 for titanium rolled to

20% reduction. However, we do not observe this effect for 40% rolled sample. Another important effect is the fragmentation inside grains. It is more intensive after AR than after SR, which is expressed by the increase of AGOS and KAM parameters - Fig. 4.24. In the case of 40% reduction this effect is visible when passing from *A*=1.3 to *A*=1.5.

As stated above, for the samples deformed to the rolling reduction of 40% we did not observe a systematic decrease of grain area versus rolling asymmetry (*A*), contrary to the samples deformed to reduction 20%. It should be noted that already for medium deformation (40% reduction) the grain structure is strongly distorted (fragmented) - compare Fig. 4.18 with Fig. 4.17. Hence, the average grain area calculated from the EBSD maps for 40% (and higher rolling reductions) is a less reliable parameter.

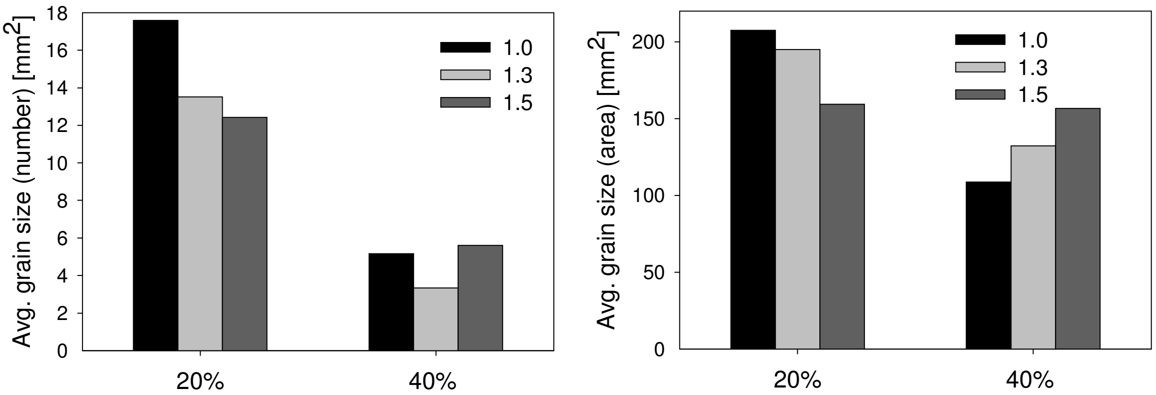

Fig.4.23. *Influence of rolling reduction (20% and 40%) and rolling asymmetry (A:1.0, 1.3 and 1.5) on grain area (μm^2) calculated using two averaging procedures: 'number' and 'area'. Results for centre layers are shown.*

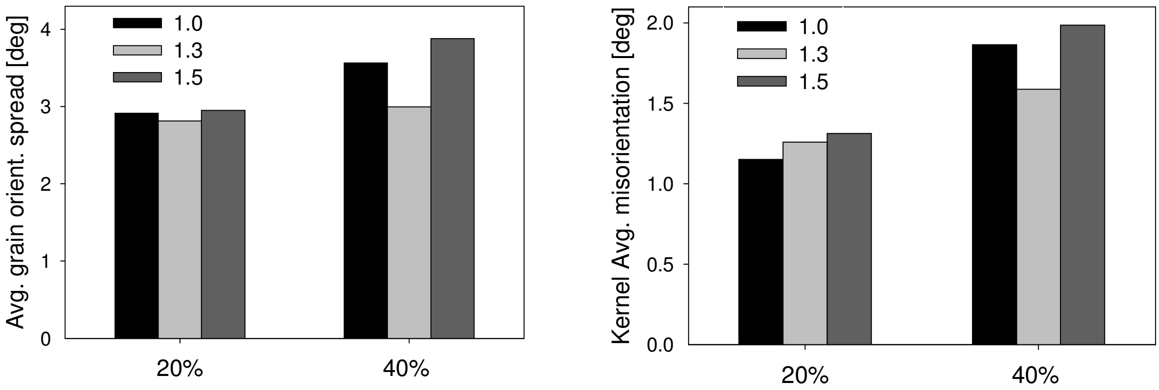

***Fig.4.24**. Influence of rolling reduction (20% and 40%) and rolling asymmetry (A:1.0, 1.3 and 1.5) on: (a) average grain orientation spread, (b) Kernel average misorientation. Results for centre layers are shown.*

Hence, the next step was to examine microstructure of the rolled and annealed titanium samples. The average grain area was examined for highly deformed samples and then annealed (recrystallized) in order to recover a regular grain structure. The EBSD maps measured for the samples symmetrically rolled (*A*=1) to 60%, 70% and 80% reductions and annealed at 550 °C during 1 h are shown in Fig. 4.25.

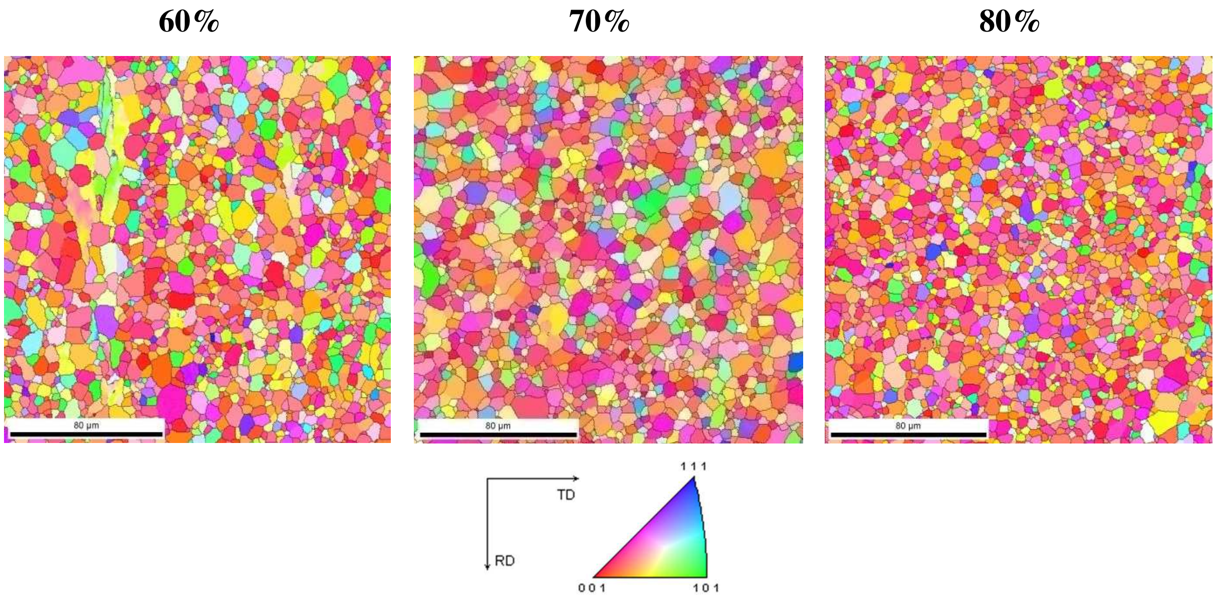
60% **70%** **80%**

***Fig. 4.25.** EBSD maps for centre layers of titanium samples symmetrically rolled (A=1) to 60%, 70% and 80% reductions and then annealed at 550 °C during 1 h. Size of the maps is: 200x200 μm^2.*

Already visually we note a distinct grain refinement with increasing rolling reduction in annealed titanium samples - Fig. 4.25. This is confirmed by bar charts of the average grain area shown in Fig. 4.26.

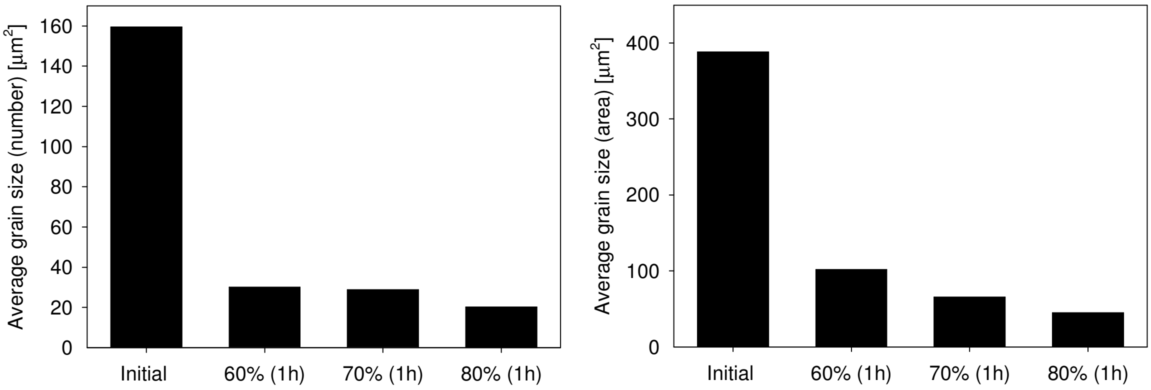

Fig. 4.26*. Grain area (µm^2) for the initial sample and for highly deformed and annealed samples. Samples were symmetrically rolled to 60%, 70% and 80% reductions. Results for centre layers are shown.*

Finally, the influence of the rolling asymmetry (*A*) was examined. The grain refinement with increasing rolling asymmetry is observed in titanium rolled to 60% reduction and annealed during 1 h at 550 ^{0}C – Fig. 4.27. In the materials rolled to 70% and 80% reduction and annealed during 1 h, the grain refinement is observed when passing from *A*=1.3 to *A*=1.5.

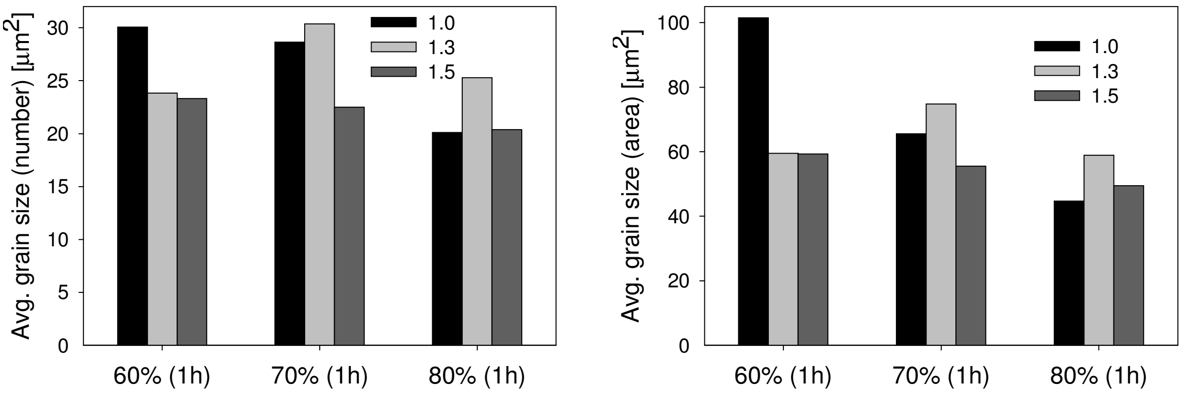

***Fig.4.27**. Influence of rolling asymmetry (A=1, A=1.3 and A=1.5) on the average grain area (μm^2) for titanium rolled to 60%, 70% and 80% reduction and annealed at 550 ^{0}C during 1h.*

In general, we can summarize that in highly deformed and annealed titanium samples one observes a systematic grain refinement with increasing deformation and a predominant grain refinement with increasing rolling asymmetry (*A*).

4.6 Conclusions

The crystallographic textures and microstructures after AR and SR processes were studied in aluminium (Al 6061) and titanium (Grade 2) samples using EBSD and X-ray diffraction techniques. AR, in which the angular velocities of rolls are different, imposes the shear stress and strain, which in turn induce modification of textures (rotation around TD) and microstructure (grain refinement and grain fragmentation).

In the case of AR **aluminium**, for higher degrees of asymmetry (*A*=1.5), the homogeneously rotated textures in three considered layers were observed, i.e., a texture homogenization occurred. This effect is caused by the occurrence of the predominant Σ_{13} internal stress component in the whole sample volume. Moreover, our study showed a significant decrease of Cube (*W*) component (which is dominant in the SR texture). AR process also modified the microstructure of aluminium sample. Comparing with SR, AR led to a refinement of microstructure: numerous bands appear along RD and a strongly fragmented structure with division into sub-grains is observed. However, basing on our results, it is difficult to conclude that AR leads to a smaller average grain size (i.e., to grain refinement), at least for the examined deformation (36% rolling reduction). On the other hand, a systematic grain refinement with increasing rolling asymmetry (A) was observed in deformed and annealed aluminium samples.

Our study of the rolled **titanium** shows, that AR leads to a characteristic texture rotation and homogenization across the material thickness, due to the occurrence of the predominant Σ_{13} internal stress component (similarly like in aluminium). A characteristic shift of the main texture maximum survives also after annealing. It was checked that with increasing deformation the grain size was decreasing. Moreover, the stress and strain shear component, present in AR process, produced a more fragmented structure of grains and grain refinement in some cases (e.g., in 20% asymmetrically rolled samples). A systematic grain refinement was confirmed in samples asymmetrically rolled (to 60%, 70% and 80% rolling reductions) and then annealed - similarly like in the case of aluminium.

The above result (checked in this work for aluminium and titanium) is of potential importance for industrially rolled materials: *AR followed by annealing leads to a more intensive grain refinement than SR*. Also, a grain and microstructure fragmentation is favoured by AR.

Chapter 5

5 FEM study of asymmetrically rolled aluminium and titanium

5.1 Introduction

The AR process was examined using FEM coupled with the crystallographic deformation model (LW model). The implementation of LW model into FEM was described in Chapter 3. Such the new created model enables a study of heterogeneous plastic deformation (like AR) taking into account its crystallographic nature. The simulation results for AR were compared with experimental ones. In the ABAQUS+LW modelling the real roll diameters and the sample size were introduced. The AR process, studied theoretically and experimentally, was realized using two identical rolls driven by independent motors, rotating with different angular velocities. As was already mentioned, during AR a strong shear stress is induced in the material. We examined the influence of this shear stress (and strain) on crystallographic textures and on basic mechanical properties. The results presented in this chapter were obtained for aluminium and titanium samples with initial crystallographic textures corresponding to the experimental ones. The calculated deformation textures were compared with experimental rolling textures from different sample layers.

5.2 ABAQUS model

The ABAQUS calculations were done in the following way. The initial model sample thickness was the same as experimental one, for aluminium sample it was 3 mm and for titanium - 8 mm. The real diameter of the rolls of d=180 mm was also used. The considered rolling reduction was 36% for aluminium and 40% for titanium (this corresponds to the final sample thickness of 1.95 mm for aluminium and 4.8 mm for titanium). The following degrees of rolling asymmetry were considered:

- for Al: A= 1.0; 1.05; 1.1; 1.3; 1.5; 2.0,
- for Ti: A=1.0; 1.1; 1.3; 1.5.

The new created model (FEM+LW), used for simulations, is a very time consuming tool (in each time increment and for each finite element the LW model is called; LW model itself performs many internal iterations). In order to decrease the calculation time the process was artificially accelerated by increasing the rate of deformation; this reduced the total simulation time and the number of time increments. The total calculation time of ABAQUS for aluminium was 0.275 s and for titanium - 0.25 s. The ABAQUS model samples were built from 8-node linear brick elements C3D8. More precisely, the elements C3D8R with reduced number of integration points were chosen (one integration point located in the centre). The reduction of calculation time can be also obtained by decreasing the number of elements. Consequently, some simplification of the model geometry, based on the process symmetry, was done. It was assumed in ABAQUS calculations that the sample does not deform along TD = x_2, i.e., $E_{22}=0$ (two other axes of the used coordinates system are: RD= x_1 and ND= x_3). In other words the *plane strain* was considered. The FEM sample contained 128 finite elements: 8 elements along ND, one element along TD and 16 elements along RD (8x1x16=128 elements).

The experimental texture of aluminium 6061 was determined by X-ray diffraction and that of titanium Grade 2 - by EBSD technique. In the next step, textures were represented by discrete grains (a given texture was represented by 1920 grains). We attached a polycrystalline sample containing 150 grains to each finite element of the C3D8R type (in each of 128 finite elements was 150 crystal grains - this gives the total number of 19200 grains representing a texture).

When modelling AR, the Coulomb friction model was applied to describe the interaction of contacting surfaces (rolls and deformed material). Accordingly, the limiting frictional shear stress between these surfaces is $\mu \cdot p$, where p is the contact pressure between the two surfaces and μ is a friction coefficient. The friction coefficient was estimated on the basis of the capture angle [69] and the value $\mu=0.30$ was used in the calculations. The rolls were modelled as non deforming rigid ones, using the *RIGID BODY option in ABAQUS software. A rigid body is a collection of nodes, whose motion is governed by the motion of a single node called a "reference point".

The appropriate values of Young modulus and of Poisson ratio were used in calculations (e.g., for aluminium: E=70 GPa and ν=0.34). The fixed Mass Scaling factor equal to 5 was applied.

5.3 Aluminium

5.3.1 Adjustment of model parameters for aluminium sample

Our next goal was to adjust correct model parameters, which describe mechanical properties of the examined polycrystalline aluminium. The initial texture was determined by X-ray diffraction and is shown in Fig. 4.5 b. To determine model parameters the tensile test along x_1 direction was considered using one FEM (ABAQUS) element coupled with LW model (Fig. 5.1). The polycrystalline sample, attached to a finite element, contained 150 grains with an orientation distribution close to the initial experimental texture.

Table 5.1. *FEM and LW model parameters for aluminium sample. The hardening parameters were found by fitting the calculated stress-strain curve to the experimental one.*

E [GPa]	ν	ρ [kg/m^3]	**slip systems**	τ_0 [MPa]	h_{sat} [MPa]	d	τ_{sat} [MPa]	a
70	0.34	2700	{111}<110>	70	390	1	235	1.2

The non-linear hardening was used in LW model; it is characterized by the following parameters: τ_0, h_{sat}, τ_{sat} and a. They were determined by adjustment of the FEM+LW predicted stress-strain curve to the experimental one. A perfect fit was obtained – Fig. 5.2. The determined parameters and other mechanical constants characterizing aluminium are listed in Table 5.1.

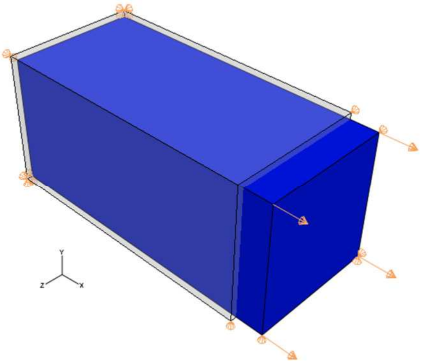

Fig. 5.1. *Tensile test simulation along x_1 direction using FEM. One element of C3D8R type with 8-nodes (but with one Gaussian point) was used and a polycrystalline model sample with 150 grains was attributed to this element.*

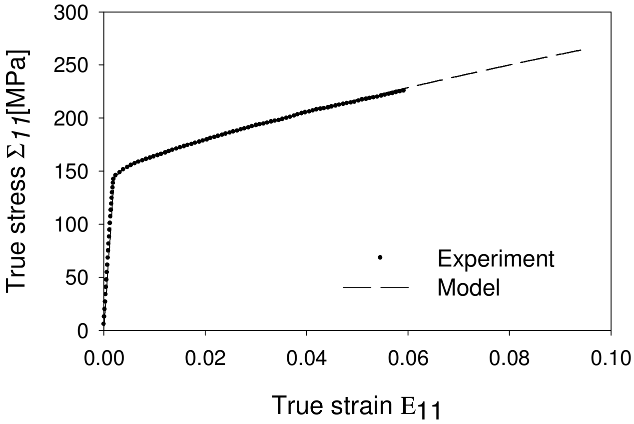

Fig. 5.2. *Comparison of the experimental tension strain-stress curve of polycrystalline aluminium with the calculated one (by FEM+LW model). The total ABAQUS simulation time was 0.1 s.*

It was also verified if the kinetic energy could be neglected as compared with the internal energy (condition for quasi-static process, discussed in Chapter 3). This condition is fairly fulfilled, which is shown in Fig. 5.3.

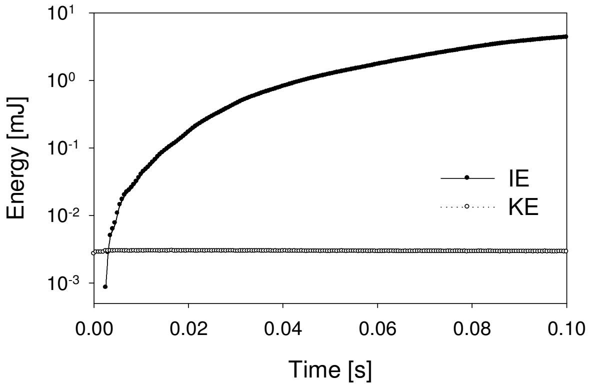

Fig. 5.3. *Plots of internal energy (IE) and kinetic energy (KE) versus simulation time for the examined polycrystalline aluminium sample.*

5.3.2 Mechanical characteristics of asymmetrically rolled aluminium

The results presented in this section were obtained for the aluminium with initial texture shown in Fig. 4.5 b. The distributions of Σ_{13} and Σ_{33} components of the internal stress in SR (*A*=1.0) and AR samples (*A*=1.05 and 1.3) are shown in Figs. 5.4 and 5.5.

One can note that during SR the shear stresses component, Σ_{13}, has the opposite sequence of signs on two surface layers (Fig. 5.4). In contrast, when the degree of rolling process increases, i.e., for *A*=1.3, there is no change of sign and the distribution of the Σ_{13} shear stress component becomes nearly homogeneous across the sample ! This results is in qualitative agreement with the calculations for isotropic material (Fig. 4.3).

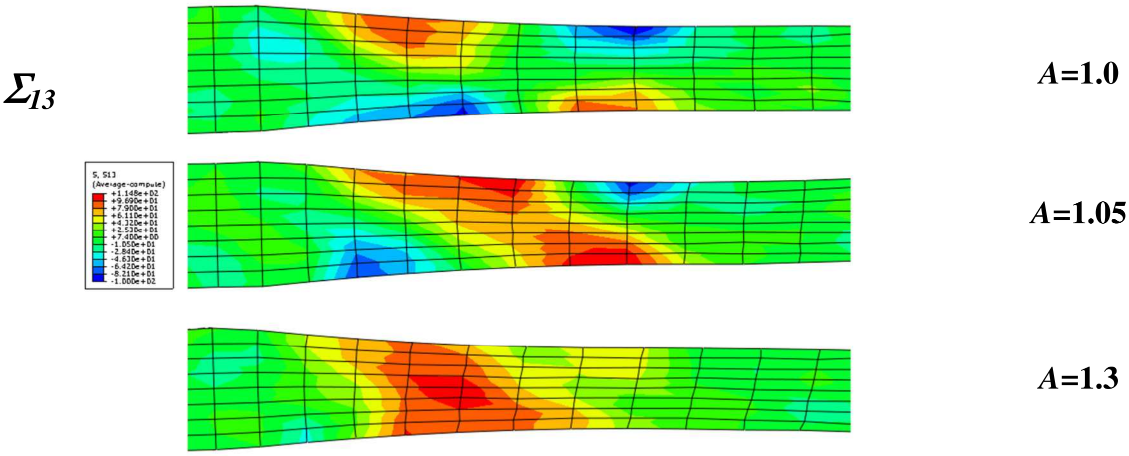

Fig. 5.4. *Distribution of Σ_{13} internal stress component during rolling of aluminium sample with asymmetry ratios $A=\omega_1/\omega_2$ equal to: 1, 1.05 and 1.3. Calculation was done for polycrystalline aluminium rolled to 36% reduction in one pass (FEM+LW model).*

The distribution of the Σ_{33} normal stress components for SR and AR is shown in Fig. 5.5. We note the decrease of the absolute value of this component in the case of AR (*A*=1.05 and *A*=1.3) compared with SR (*A*=1.0). This is in qualitative agreement with the result presented in Fig. 4.3 for *A*=1.15. This result means that the normal pressure exerted by rolls decreases with increasing rolling asymmetry.

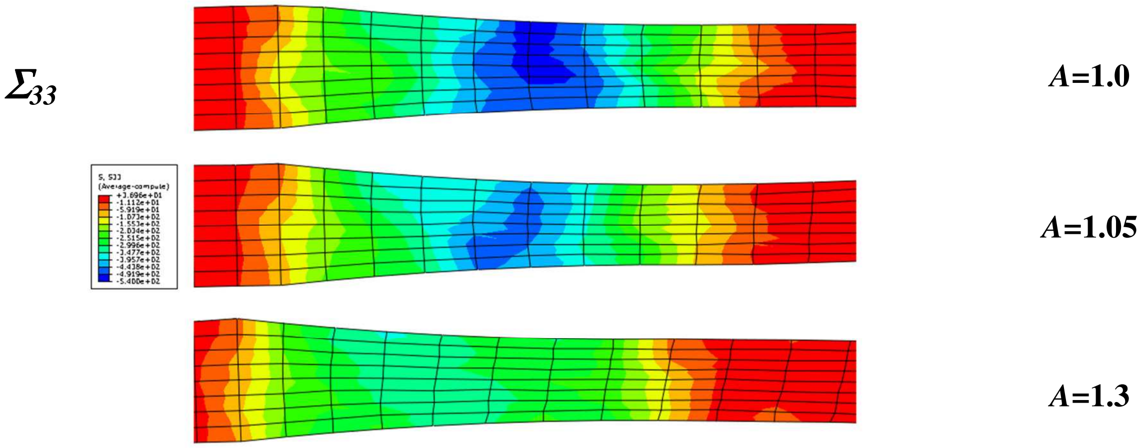

Fig. 5.5. *Calculated distribution of Σ_{33} internal stress component during rolling with asymmetry ratios $A=\omega_1/\omega_2$ equal to: 1, 1.05 and 1.3. Calculation was for polycrystalline aluminium rolled to 36% reduction in one pass (FEM+LW model).*

The distributions of principal strain components, E_{11} and E_{33}, during SR and AR are shown in Fig. 5.6. In the case of SR (A=1.0), we observe nearly perfectly symmetrical strain distributions with respect to the horizontal plane passing through the sample centre. In the case of AR (A=1.05 and A=1.3), we observe a departure from this symmetry and some sample bending arises.

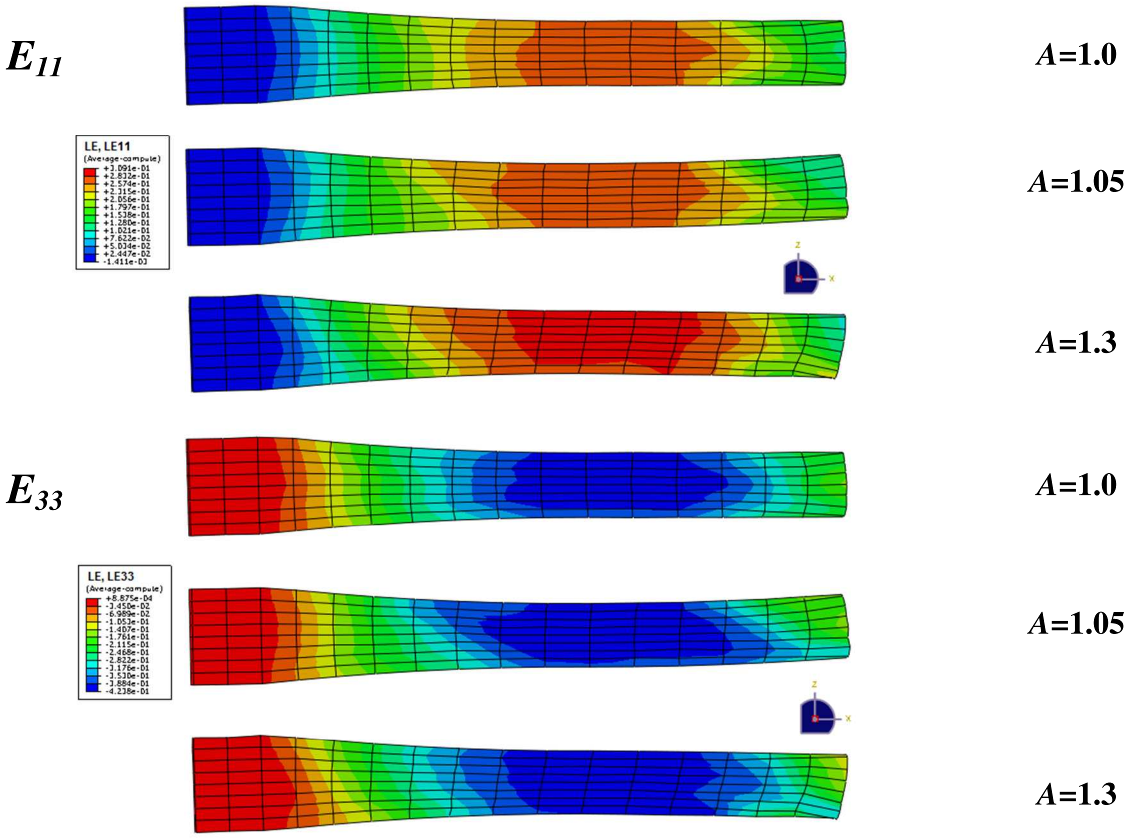

***Fig. 5.6**. Calculated distributions of strain components E_{11} and E_{33} during symmetric and asymmetric rolling of polycrystalline aluminium (A=1.0, A=1.05 and A=1.3.*

The variation of internal and kinetic energy vs. calculation time during rolling is shown in Fig. 5.7 (the case of *A*=1.0 is presented). Our FEM calculations were done in *Explicit mode* and the condition, which has to be verified is that the kinetic energy should be negligible compared with the internal one. According to the result shown in Fig. 5.7 we find that the kinetic energy is approximately 2÷3 orders of magnitude lower, therefore the criterion for a quasi-static process is fulfilled.

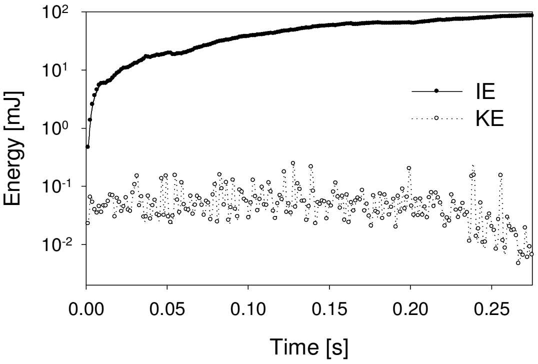

Fig. 5.7. *Plots of kinetic and internal energy (KE and IE) versus total simulation time for symmetric rolling of polycrystalline aluminium* ($A = \omega_1/\omega_2 = 1.0$).

And finally the external characteristics of the rolling process were examined. One of the advantages of AR, predicted by FEM calculations and verified experimentally, is the reduction of the average normal force (F_{AR}) exerted on the sample surface. This is a consequence of the reduction of the absolute value of the normal stress Σ_{33} exerted on the material by rolls (compare Figs. 4.3 and 5.5). The predicted normal force vs. A, for rolling of polycrystalline aluminium, is shown in Fig. 5.8a; it is presented as the ratio F_{AR}/F_{SR} . It was shown in [69][70], that the reduction of the applied normal force depends also on the deformation in one rolling pass (higher deformation leads to a higher reduction of force).

In agreement with experimental observations, our calculations predict that AR samples are bent in the direction perpendicular to the rolling plane - cf. Fig. 5.6. Bending is a typical behaviour during AR and has been analysed by different authors i.e. [71]. In general, it is undesirable effect. However, in some applications it can be used to obtain a cylindrical shape product from a plate such as, for example, during bending a sheet on a coiler. The calculated bend magnitude, defined as deflection (in mm) at the end of 200 mm rolled plate, versus A is shown in Fig. 5.8b. We note that bending can be reduced by an appropriate choice of the degree of anisotropy A. In our case (36% rolling reduction) its magnitude is strongly reduced for A>1.3. As expected, no bending was predicted for symmetric rolling, A=1.0. In general, the bend flash depends also on deformation in one rolling pass.

Another important variable is the total deformation work, W, supplied by the rolling mill to obtain a given deformation. It is presented as the ratio W_{AR}/W_{SR} , i.e., as the relative deformation work. This work increases with the degree of rolling asymmetry, A (Fig. 5.8c). It can be shown that this effect weakens with progressing deformation [72].

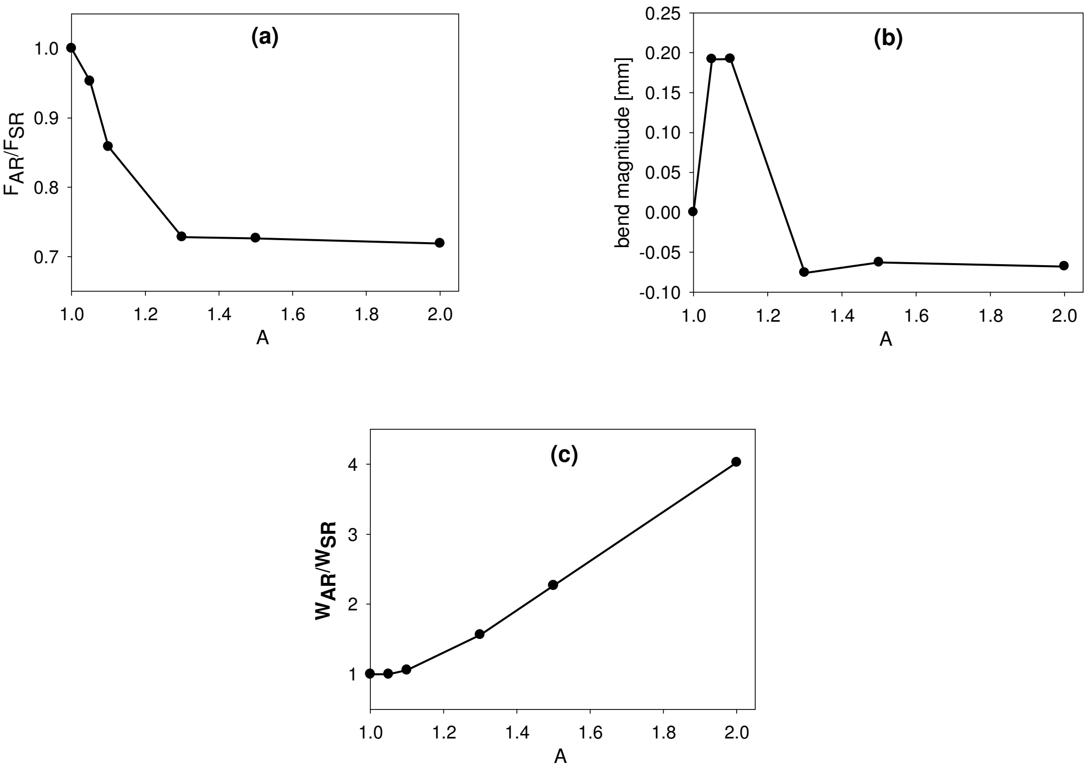

Fig. 5.8*. Mechanical characteristics versus $A=\omega_1/\omega_2$ predicted by FEM+LW model for asymmetric rolling of polycrystalline aluminium (rolling reduction 36% in one pass):*
a) relative normal force (F_{AR}/F_{SR}), b) bend magnitude defined as deflection (in mm) at the end of 200 mm rolled plate, c) relative deformation work (W_{AR}/W_{SR}).

5.3.3 Crystallographic textures of asymmetrically rolled aluminium

The rolling textures were calculated and measured in three regions of the sample: in the top, bottom and central layers. The variation of crystallographic texture in AR aluminium samples was discussed and described in section 4.4.2. The predicted rolling textures (FEM+LW model) for three sample layers and for three degrees of rolling asymmetry (A=1.0, A=1.1, A=1.5) are compared with experimental textures of aluminium in Figs. 5.9 – 5.11. Only $\varphi_2=0^0$ sections, the most representative for texture modification, are presented in these figures.

We observe in the predicted and experimental textures systematic shifts of the position of brass (B) component (they do not occur only in the centre layer of SR material). The signs of the predicted shifts of B orientation, visible as departures from the red line in the $\varphi_2=0^0$ section, agree with experimental ones in all considered cases of the rolling asymmetry:

A=1.0, *A*=1.1, *A*=1.5 (Figs. 5.9 – 5.11). These shifts corresponds to respective texture rotations around TD. Generally, the amplitudes of the shifts are lower in the experimental textures than in the predicted ones. This can be explained by a possible occurrence of some glide between the rolls and a deformed material.

Top surface **Centre** **Bottom surface**

a) Predicted: FEM+LW

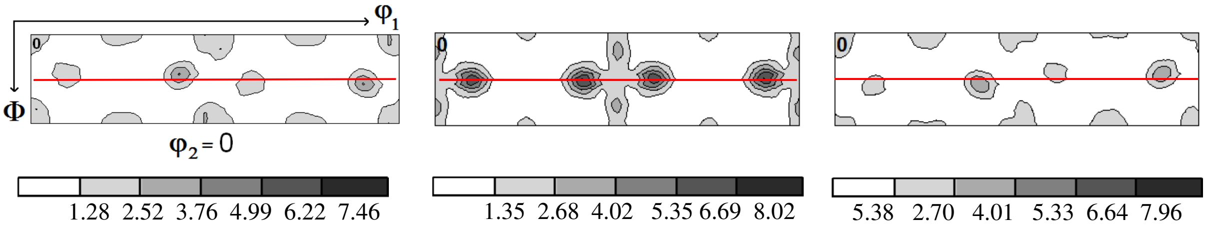

b) Experimental

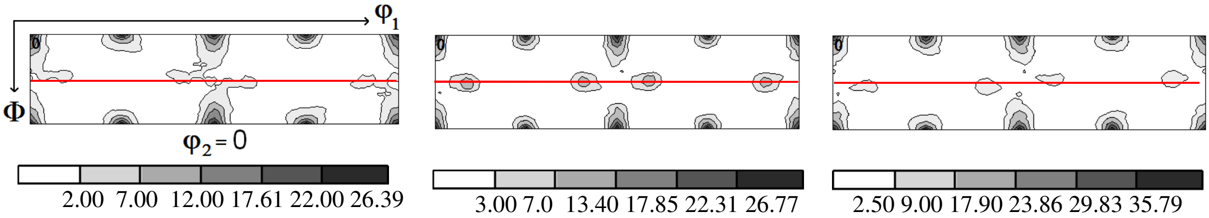

Fig. 5.9. *Comparison of symmetrically rolled textures of polycrystalline aluminium (A=ω_1/ω_2 =1.0): a) predicted by FEM+LW model, b) determined by X-ray diffraction. ODF $\varphi_2=0^0$ sections are shown.*

Top surface **Centre** **Bottom surface**

a) Predicted: FEM+LW

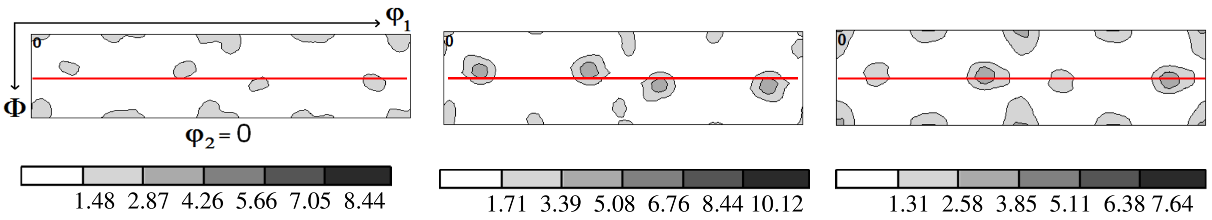

b) Experimental

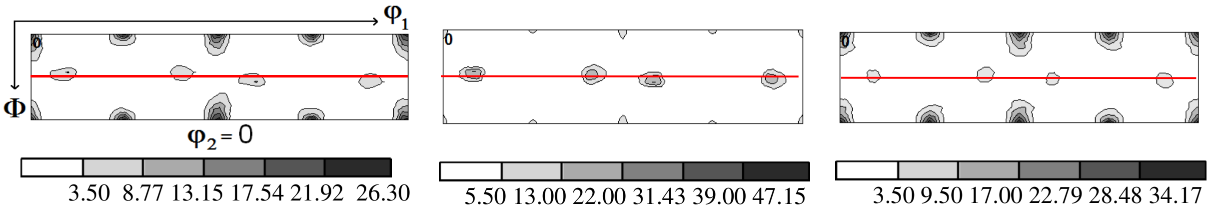

Fig. 5.10. *Comparison of asymmetrically rolled textures of polycrystalline aluminium (A=ω_1/ω_2 =1.1): a) predicted by FEM+LW model, b) determined by X-ray diffraction. ODF $\varphi_2=0^0$ sections are shown.*

Top surface **Centre** **Bottom surface**

a) Predicted: FEM+LW

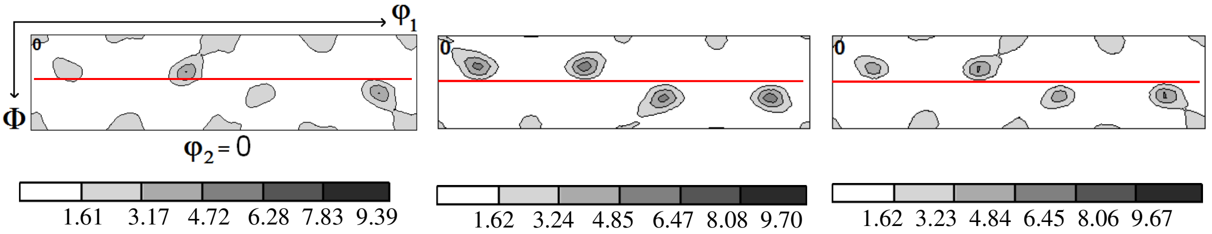

b) Experimental

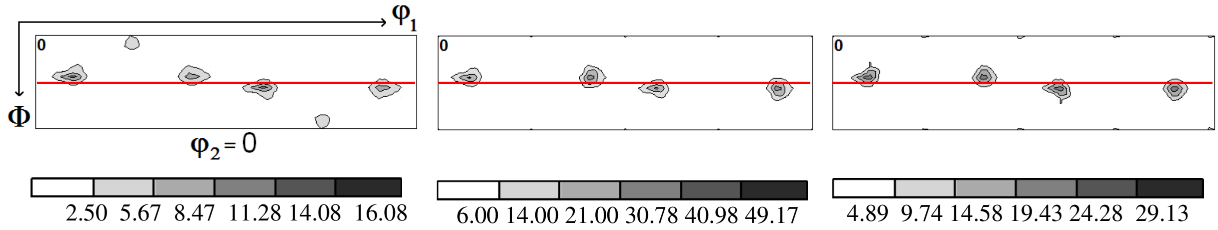

Fig. 5.11. *Comparison of asymmetrically rolled textures of polycrystalline aluminium ($A=\omega_1/\omega_2=1.5$): a) predicted by FEM+LW model, b) determined by X-ray diffraction. ODF $\varphi_2=0^0$ sections are shown.*

The character of shifts of the maxima of *B* component in SR and AR aluminium textures was already discussed in Section 4.4.2. We observe the opposite signs of the shift in the top and bottom layer textures of SR material, while in the centre layer there is no shift (Fig. 5.9). In contrast, a homogeneous shift appears in all three material layers of AR samples (figs. 5.10 - 5.11). The effect is clearly visible in the case of $A=1.5$ (Fig. 5.11). Therefore, we can conclude that one observes the effect of texture homogenization across the material thickness after AR.

The amplitude of texture rotation around TD (causing the shift of texture maxima) was analyzed in function of distance from the top surface. The division of the rolled material into eight layers, used in FEM+LW calculations, is shown in Fig. 5.12.

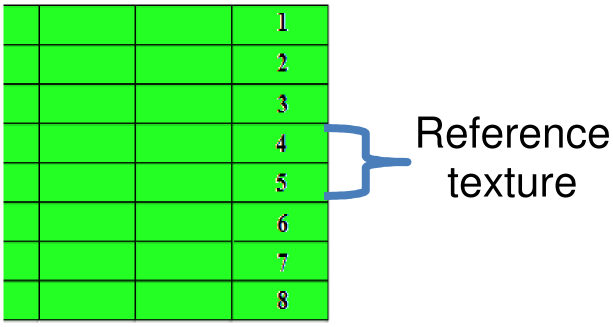

Fig. 5.12. *Division of the rolled material into eight layers used in FEM+LW calculations.*

In each of the considered layers, the angle *Ω* was estimated, which characterizes the texture rotation around TD. This angle was determined by finding an opposite rotation (- *Ω*), which restored back the orthorhombic symmetry of texture, i.e. it made it similar to the texture from the central layer of SR material (*A*=1.0). The variation of such determined angle *Ω* vs. distance from the top surface is shown in Fig. 5.13. It can be noted that in the case of symmetric rolling (*A*=1.0) the angle *Ω* changes the sign, when passing from the top to the bottom surface and *Ω*=0 appears in the sample centre. This is consistent with the character of shifts visible in Fig. 5.9. Still for *A*=1.05 the angle *Ω* changes the sign, but this occurs already closer to the bottom surface. For higher *A* values the angle *Ω* has negative sign everywhere across the sample. Let us note that for *A*=1.5 and *A*=2.0 the distribution of *Ω* versus depth becomes more homogeneous. Hence we conclude, that the texture rotation across the sample is much more homogeneously distributed after AR than after SR. This means that AR materials have more homogeneous textures than SR ones.

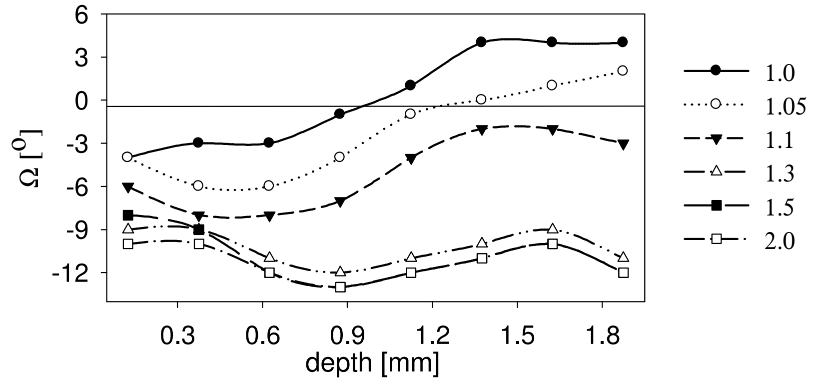

Fig. 5.13. *Rotation angle Ω vs. depth for textures from different layers of aluminium sample with reference to the texture of the centre layer of symmetrically rolled material. The following rolling asymmetry ratios, A=ω_1/ω_2, were considered: 1.0, 1.05, 1.1, 1.3, 1.5, 2.0.*

Another illustration of texture variation across the sample is shown in Fig. 5.14. The rolled material studied by FEM+LW model was divided again into eight layers (Fig. 5.12). The average texture of two central layers (No. 4 and 5) served as the reference one. Next the correlation factor, *R*, according to the procedure developed in [36], was used to express the similarity between a given texture and the reference one (a short explanation of the meaning of R factor was done in section 2.3). The calculated correlation factor R versus depth for different degrees of rolling asymmetry is shown in Fig. 5.14. We notice that the strongest variation of R appears for low A (1.0, 1.05, 1.1). For higher degrees of asymmetry (A=1.5 and A=2.0) the variation of R becomes nearly flat and reaches the values of R around 0.9. This confirms the effect of texture homogenization across the sample thickness during AR.

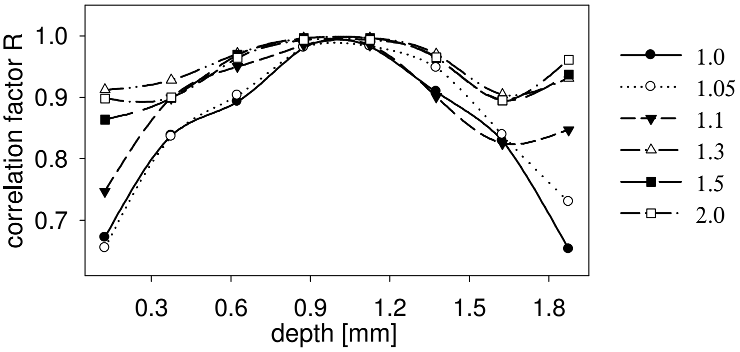

Fig. 5.14. *Correlation factor R expressing similarity of textures from different layers of aluminium sample with the reference SR texture of the centre layer. The following degrees of rolling asymmetry, A=ω_1/ω_2, were considered: 1.0, 1.05, 1.1, 1.3, 1.5, 2.0.*

5.3.4 Examination of texture stability

The stability of AR textures was examined using the polycrystalline deformation model (LW). As already discussed, the main role in texture modification during AR plays the Σ_{13} shear stress component, therefore its influence on the predicted results was examined. A set of initial grains, with crystal orientations regularly disposed in the Euler space was used (every 5^0 with respect to φ_1, Φ, φ_2). This 'sample' was deformed using the following applied stress tensor:

$$\Sigma_{ij} = \Sigma \begin{bmatrix} 1 & 0 & K \\ 0 & 0 & 0 \\ K & 0 & -1 \end{bmatrix} \tag{5.1}$$

where Σ is the stress magnitude and K expresses the proportion of Σ_{13} stress component.

The magnitude of lattice rotation (Δ) of each grain, resulting from deformation, was examined. It was calculated as a misorientation between the initial and final grain orientations after 36% rolling reduction (consistently with the experimental aluminium textures). A given texture orientation is potentially stable if Δ is close to zero (this is a necessary condition for orientation stability). The rotation magnitude Δ was calculated for all points of the grid in the considered part of the Euler space, namely, every 5^0 in the range $0 \leq \varphi_1 \leq 360^0$, $0 \leq \Phi \leq 90^0$, $0 \leq \varphi_2 \leq 90^0$. The calculations were done for six values of K, namely 0, 0.2, 0.5, 1, 2, 4 and 'orientation stability' maps were then drawn.

The predicted orientation distributions of Δ are shown in Fig. 5.15. The minima of rotation magnitude (Δ) correspond to white zones and the maxima - to black zones. We note that the previously discussed shifts of the B component maxima (visible in $\varphi_1=0^0$ section) in the *experimental* AR texture for A=1.5, in three material layers (cf. Fig. 5.11 b), are nicely reproduced by the shifts of the rotation magnitude minima in the cases of K=0.2. An analogous correspondence occurs between the *predicted* AR textures for A=1.5 (Fig. 5.11 a) and the minima of Δ in the case of K=0.5. Hence, we note that a real magnitude of the shear stress component, Σ_{13}, during AR is described approximately by K=0.2. It should be also noted that the minima of Δ for K=0 correspond very well to the maxima of the experimental SR texture from the centre layer (Fig. 5.9 b - centre), where the B component shift does not appear. All the above correspondences confirm that the examined textures are stable (the necessary condition is fulfilled).

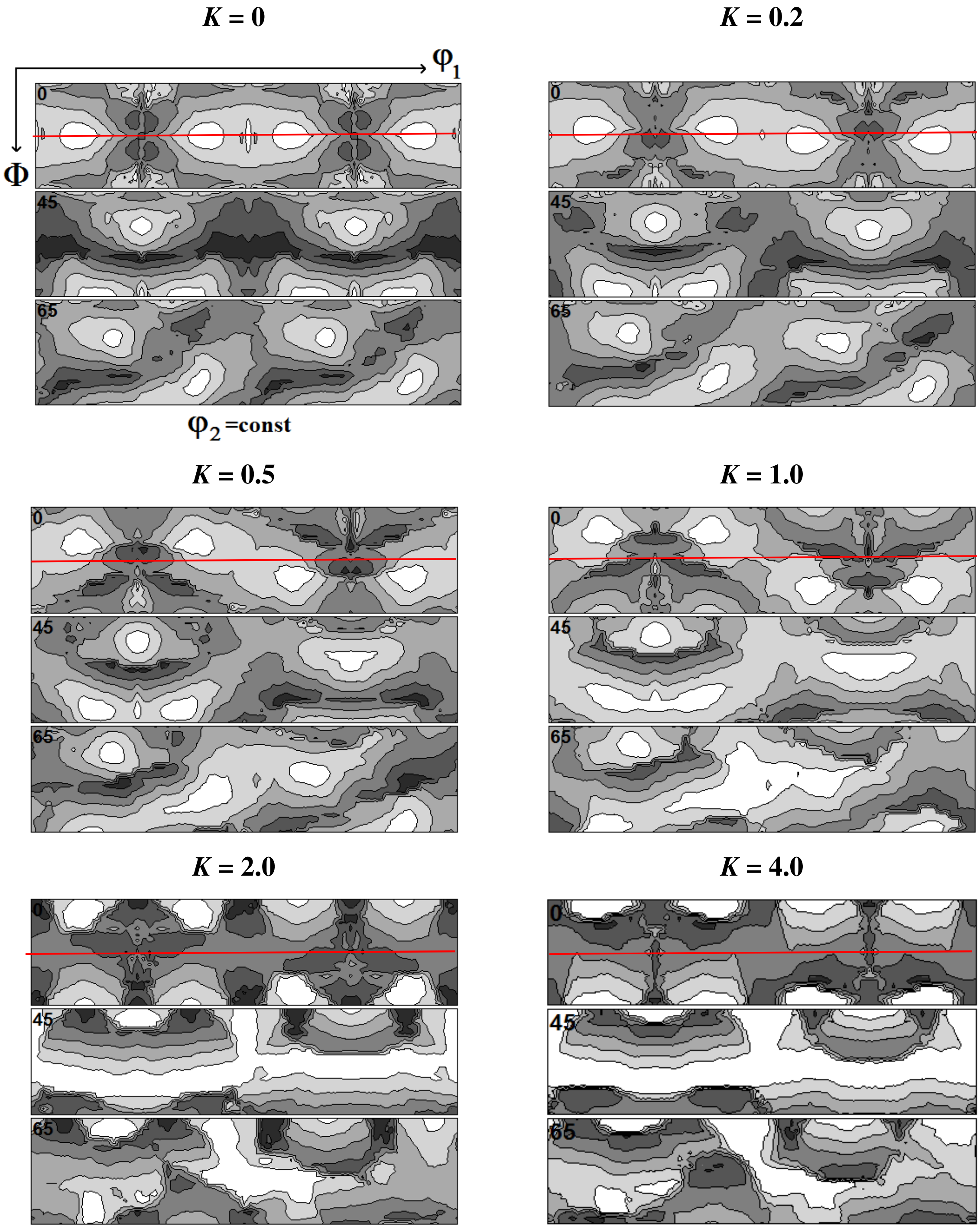
$K = 0$

$K = 0.2$

$K = 0.5$

$K = 1.0$

$K = 2.0$

$K = 4.0$

Fig. 5.15. *Stability maps calculated for symmetric and asymmetric rolling for K = 0, 0.2, 0.5, 1.0, 2.0 and 4.0. White area show orientations with minimum rotation, black – with maximum rotation.*

An interesting result is that a very high amplitude of the shear stress component, which is to say *K*=4, leads to the formation of rotation magnitude minima which correspond to a typical b.c.c. rolling texture with dominating rotated cube component - *RW* $(0^0, 0^0, 45^0)$ - Fig.5.16. A similar effect was confirmed in literature (e.g., [9]).

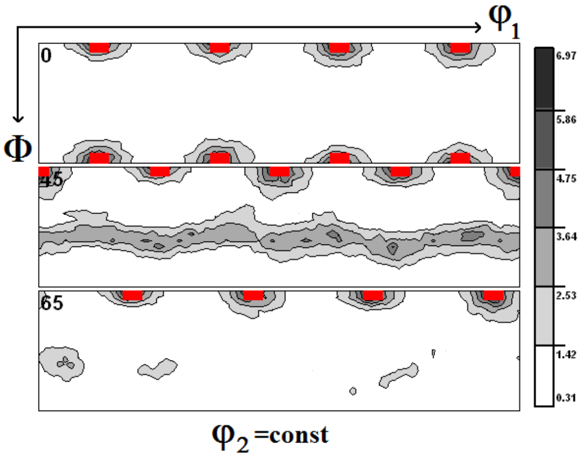

Fig. 5.16. *Experimental texture of ferritic steel symmetrically rolled to the reduction 50% (material with b.c.c. structure). The RW component (🟥) is marked.*

5.3.5 Influence of friction coefficient

We have also examined the influence of friction coefficient on the predicted textures and on the shear stress (Σ_{13}) distribution across the sample. The results for SR (*A*=1.0) are presented in Fig. 5.17. The following values of the friction coefficient (μ) were examined: 0.3, 0.25 and 0.2. Principally, there are two effects, when the friction coefficient is lowered:

a) the Σ_{13} component becomes weaker,

b) the shift of brass component *B* (in $\varphi_1 = 0$ section) is slightly smaller.

Therefore, we conclude that a main effect of lowering the friction coefficient is a modification of the Σ_{13} component distribution in the material; a very weak effect on texture is observed.

(a) μ=0.3

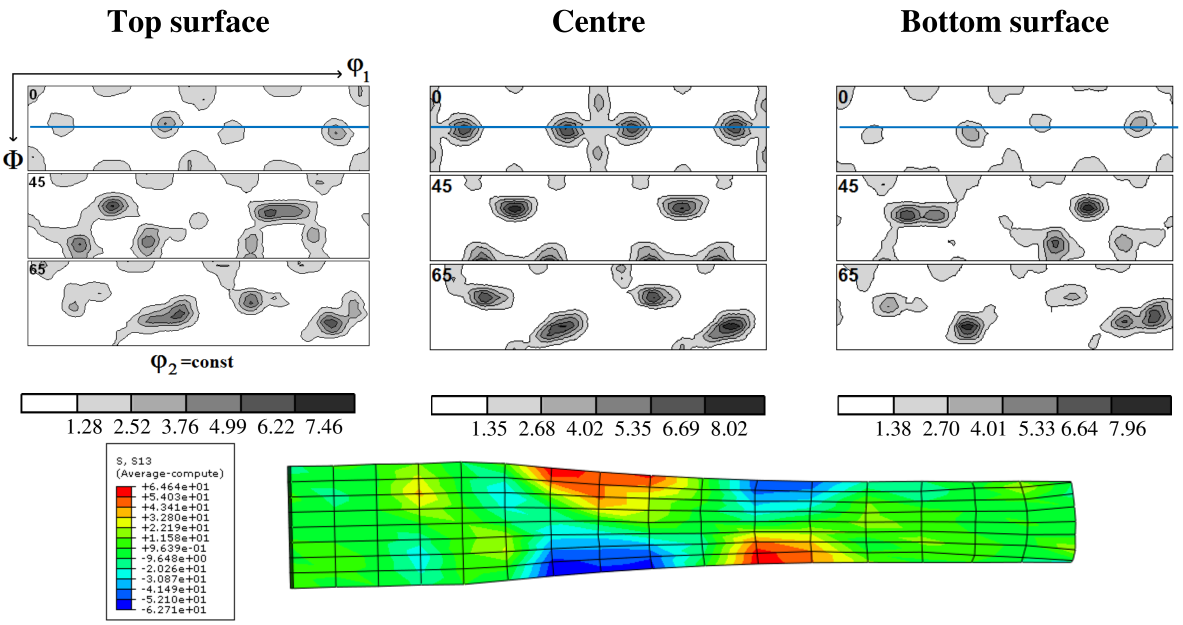

(b) μ=0.25

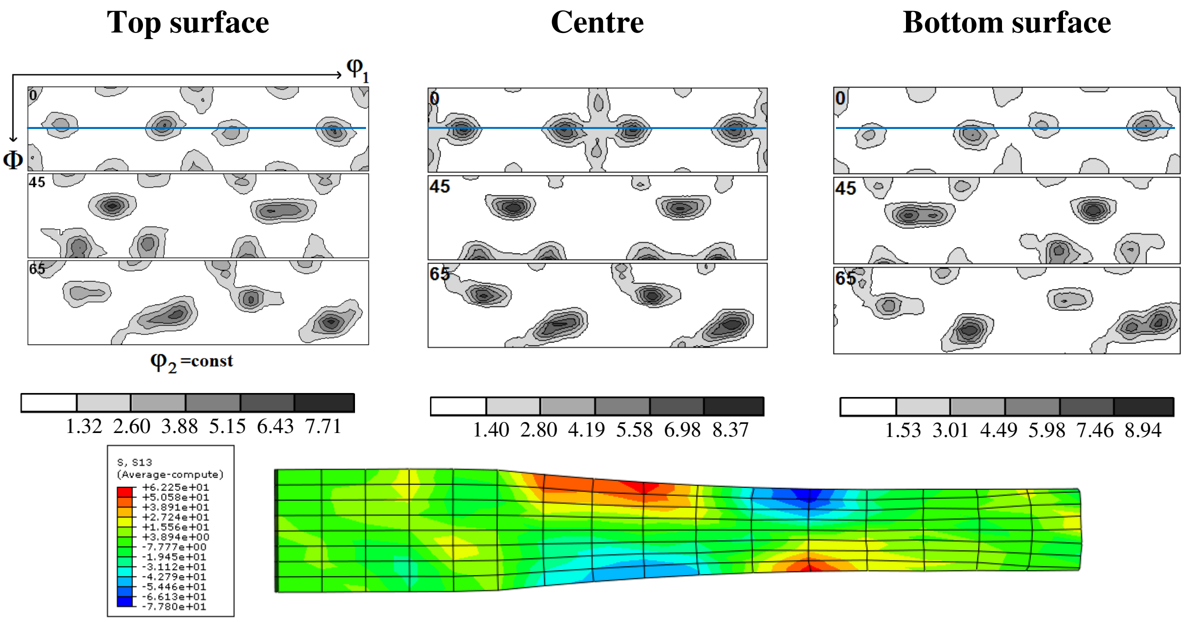

(c) μ=0.2

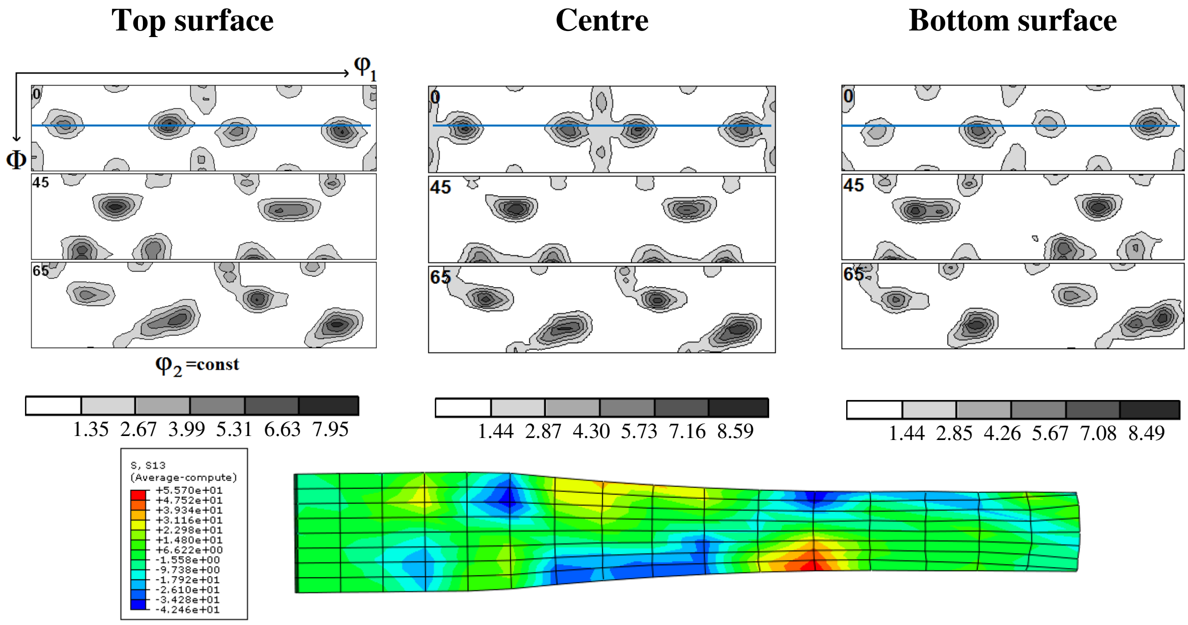

Fig. 5.17. *Textures and distributions of Σ_{13} internal stress component across the polycrystalline aluminium sample predicted by FEM+LW model for different values of friction coefficient: μ = 0.3, 0.25 and 0.2. Symmetric rolling (A=1.0) of polycrystalline aluminium sample to 36% reduction in one roll pass was considered.*

5.3.6 Plastic anisotropy

Textures resulting from SR and AR modify physical properties of a material. The example of practical importance is the plastic anisotropy. It can be characterized by the Lankford coefficient R_L, defining the width-to-thickness reduction ratio during a tensile test:

$$R_L = \frac{\varepsilon_W^{pl}}{\varepsilon_T^{pl}} \tag{5.2}$$

In rolled textured sheets, R_L factor is highly anisotropic, in other words, it depends on the tensile axis orientation with respect to RD, defined by the angle α, hence R_L=R_L(α). The isotropic plasticity corresponds to R_L =1 for any α value. The R_L vs. α relations for the top, bottom and centre layers in the initial and SR and AR material were calculated basing on experimentally determined textures, using the procedure proposed in [73] and they are shown in Fig. 5.18. It is clear that R_L *(α)* is different after the two rolling modes: SR and AR ones. The most important differences between these two modes of rolling appear:

- in the central layer for $\alpha=45^0$,
- in top surface for transverse direction ($\alpha=90^0$), and
- in the bottom surface for transverse and rolling directions ($\alpha=0^0$ and $\alpha=90^0$).

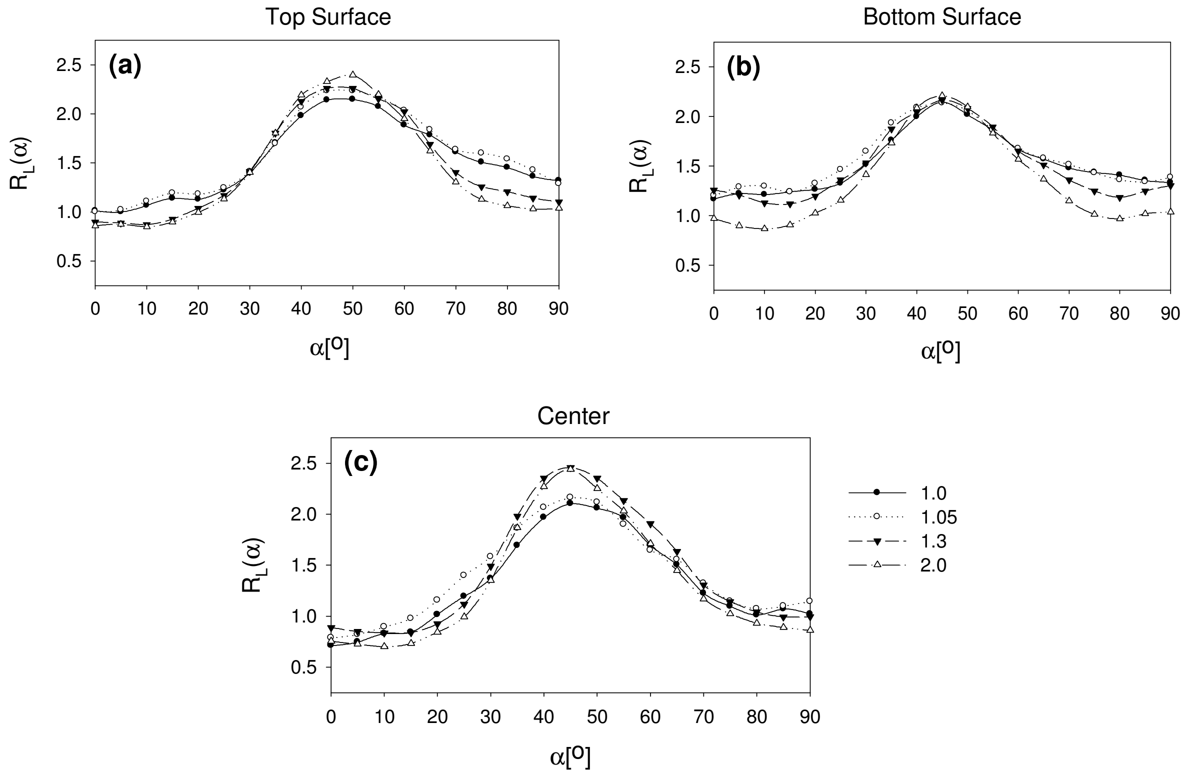

Fig. 5.18. Calculated Lankford coefficient vs. α *(angle from rolling direction) in three sample layers for materials rolled with different* $A=\omega_1/\omega_2$ *ratios: (a) top, (b) bottom and (c) centre surface.*

Therefore, we can conclude that AR can be used to modify the plastic anisotropy.

5.4 Titanium

5.4.1 Adjustment of model parameters for titanium sample

In order to simulate the processes of SR and AR of the commercially pure polycrystalline titanium (Grade 2) we had to adjust first correct model parameters, which described mechanical properties of this material. The initial experimental texture of titanium was determined by EBSD technique and is shown in Fig. 4.13. To determine model parameters the results of tension test were considered. The same simplified ABAQUS + LW model was used as in the case of tension test of aluminium (described in the section 5.3.1). The studied material was represented as one finite element (Fig. 5.1) and a polycrystalline model sample with 150 grains was connected with it. The crystallites of this model sample had the orientation distribution corresponding to the experimentally determined initial texture of titanium sample.

The non-linear hardening law characterized by the parameters: h_{sat}, τ_0, a, τ_{sat} was used. They were determined by adjustment of the FEM+LW predicted stress-strain curve to the experimental one - Fig.5.19. It can be noted that the predicted curve does not coincide well with the experimental one in the range of elasto-plastic transition. This is mainly due to use of relatively simple non-linear hardening law (Eq. 1.15) but also to the occurrence of highly anisotropic phenomena in this range, difficult to describe.

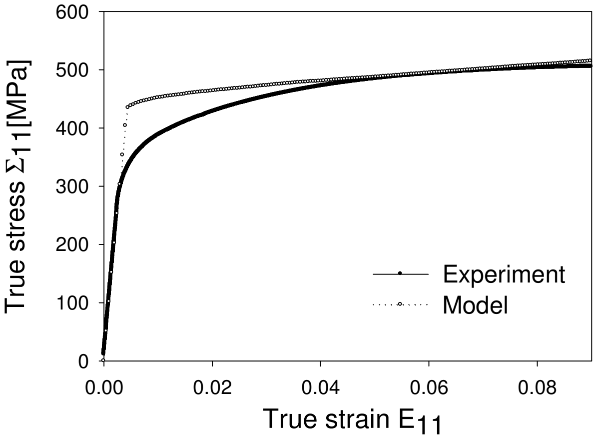

Fig. 5.19. Comparison of experimental tension strain-stress curve of titanium (Grade 2) with calculated one (FEM+LW). The total simulation time was 0.1 s.

An illustration of this anisotropy is given in Fig. 5.20, where the experimental stress-strain curves determined for three characteristic sample directions are shown: for RD, ND and the direction inclined 45^0 from RD. This is the reason that in future calculations a more sophisticated hardening law should be tried. However, as seen in Fig. 5.19, our adjustment is correct in elastic and plastic range, which are essential for our calculations.

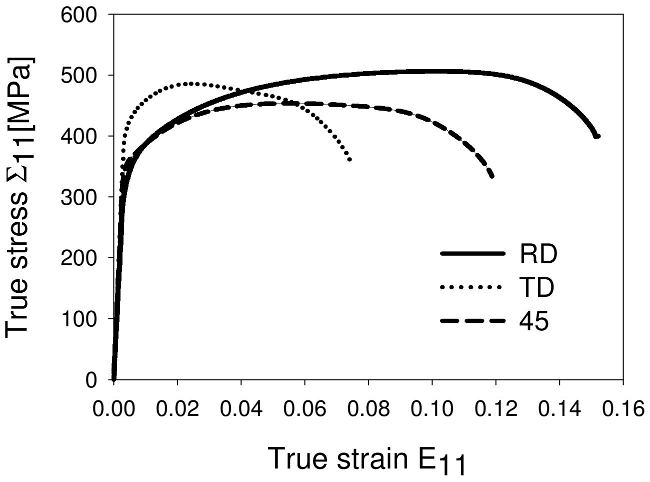

Fig. 5.20. *Experimental tension strain-stress curves for titanium for three directions in the rolled plate: RD-rolling direction, ND-normal direction and the direction inclined 45^0 to RD.*

The material and model parameters used in the calculations for titanium are presented in Tables 5.3 and 5.4. It should be noted that in the calculations for titanium the twinning mechanism was taken into account. Our EBSD measurements confirmed that two types of twinning systems are active during rolling. The observed maxima of misorientation angle distribution (Figs. 4.20 and 4.21) correspond to the boundaries of tensile and compressive twins. Consequently, these two types of twins were taken into account in our calculation.

***Table 5.3**. FEM and LW model parameters for titanium sample. The hardening parameters were found by fitting the calculated tension stress-strain curve to the experimental one.*

E (GPa)	ν	ρ (kg/m^3)	h_{sat} (MPa)	d	τ_{sat} (MPa)	A
101	0.34	4500	250	1.0	440	1.5

Table. 5.4 *Slip and twinning system used for titanium and their initial critical shear stresses τ_0 (expressed in MPa).*

Slip systems			**Twinning systems**		
Prismatic	$\{10\bar{1}0\}\langle 11\bar{2}0\rangle$	τ_0=215	Tensile	$\{10\bar{1}2\}\langle\bar{1}011\rangle$	τ_0=280
Basal <a>	$\{0001\}\langle 11\bar{2}0\rangle$	τ_0=350	Compressive	$\{11\bar{2}2\}\langle\bar{1}\bar{1}23\rangle$	τ_0=365
Pyramidal <a>	$\{10\bar{1}1\}\langle 11\bar{2}0\rangle$	τ_0=235			

Also in the present case the condition for quasi-static process (discussed in section 3.3) is fulfilled, which is shown in Fig. 5.21.

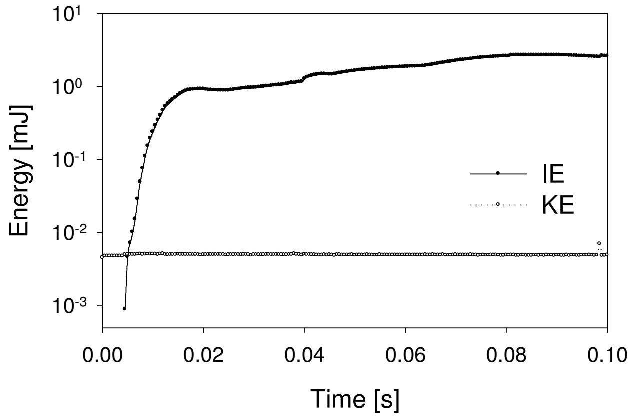

Fig. 5.21. *Calculated plots of internal and kinetic energy (IE and KE) versus simulation time for titanium deformed in uniaxial tension test.*

5.4.2 Internal stresses during asymmetric rolling

The in-depth distributions of the internal stress components, Σ_{13} and Σ_{33}, during SR and AR (A=1.3 and A=1.5). are shown in Fig. 5.22. The Σ_{13} component plays an important role for the material properties during rolling. Its distribution has characteristic feature: in SR (A=1.0) it has opposite variations in both surface layers (top and bottom). With increasing rolling asymmetry its distribution becomes nearly homogeneous across the sample (for A=1.5). In contrast, the distribution of Σ_{33} stress component has relatively homogeneous distribution across the sample thickness for the examined degrees of asymmetry, but its amplitude distinctly decreases with increasing degree of rolling asymmetry. This confirms a known property of AR: the normal force is reduced in this process (which is beneficial for roll mill durability).

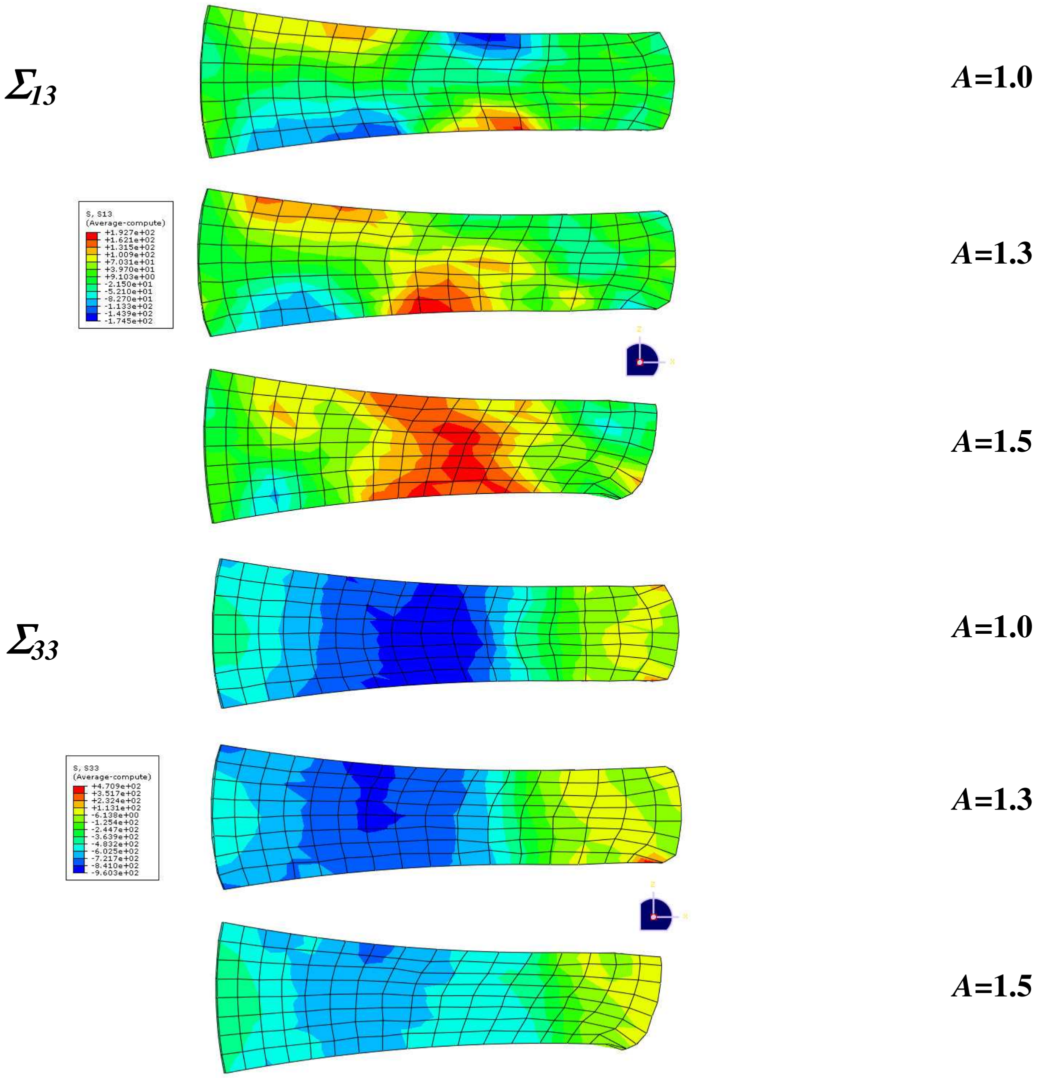

Fig. 5.22. *Calculated distribution of Σ_{13} and Σ_{33} stress components during rolling of titanium for: A=1.0, A=1.3 and A=1.5. Results obtained for polycrystalline titanium rolled to 40% reduction using FEM+LW model.*

In order to obtain stable solutions by ABAQUS/Explicit solver, the kinetic energy was controlled during calculations. The variation of internal and kinetic energy vs. calculation time during rolling is shown in Fig. 5.23 (the case of SR, i.e., for *A*=1.0, is presented). The obtained result confirms that the criterion for a quasi-static process is fulfilled (the kinetic energy should not exceed a small fraction - typically 10% - of the internal energy during total simulation time).

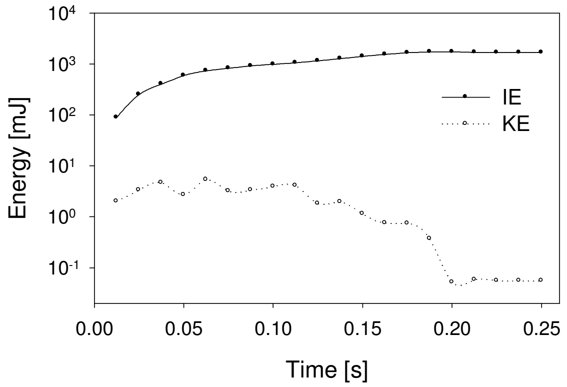

Fig. 5.23. Plots of kinetic and internal energy (KE and IE) versus total simulation time for symmetric rolling of polycrystalline titanium (A=1.0). Total simulation time was 0.25 s.

5.4.3 Crystallographic textures of asymmetrically rolled titanium

The predicted (MES+LW model) and measured textures across the sample thickness (top, centre and bottom layers) for SR (*A*=1.0) and AR (*A*=1.3) are shown in Fig. 5.24 and 5.25. The variation of experimental texture of titanium vs. degree of rolling asymmetry was already discussed in section 4.5.2.

The characteristic effect after SR is the symmetric position of the main texture maximum with respect to the line $\varphi_2=30^0$ in the centre layer (in $\varphi_1=0^0$ ODF section). In contrary, this maximum is shifted to the right (i.e., towards higher φ_2 values) in the top layer and to the left (i.e., towards smaller φ_2 values) - in the bottom layer (cf. Fig. 5.24 b). This corresponds to the appearance of the opposite shear stresses (Σ_{13}) in two surface layers. This effect is clearly predicted by our model (Fig. 5.24 a) and is reflected in the measured texture (Fig. 5.24 b), though the amplitude of the shift is smaller in experimental ODF.

In AR process the shear stress is much more homogeneously distributed across the sample and, consequently, the shift of maximum has the same sense in three layers (shift to the right), as predicted by FEM+LW model - Fig. 5.25 a. Similar, although weaker, shifts are observed in experimental textures in three considered layers (Fig. 5.25 b).

As stated above, the amplitude of the maximum shift is lower in experimental textures than in predicted ones (the same effect was observed in aluminium sample). This effect is probably due to the appearance of a small glide between the rolls and a deformed material.

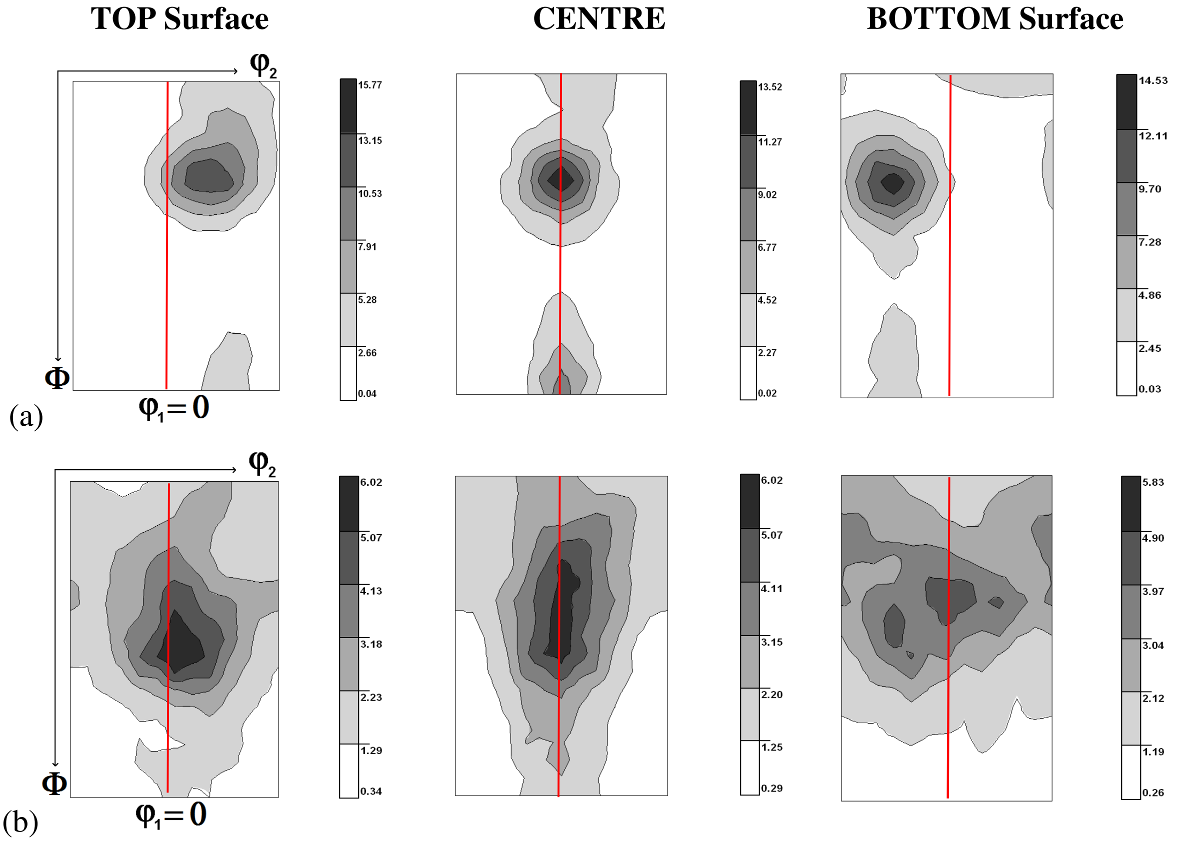

Fig. 5.24. *Symmetrically rolled textures of polycrystalline titanium* (A=ω_1/ω_2 =*1.0*)*: a) predicted by FEM+LW modelling, b) determined by EBSD technique.*

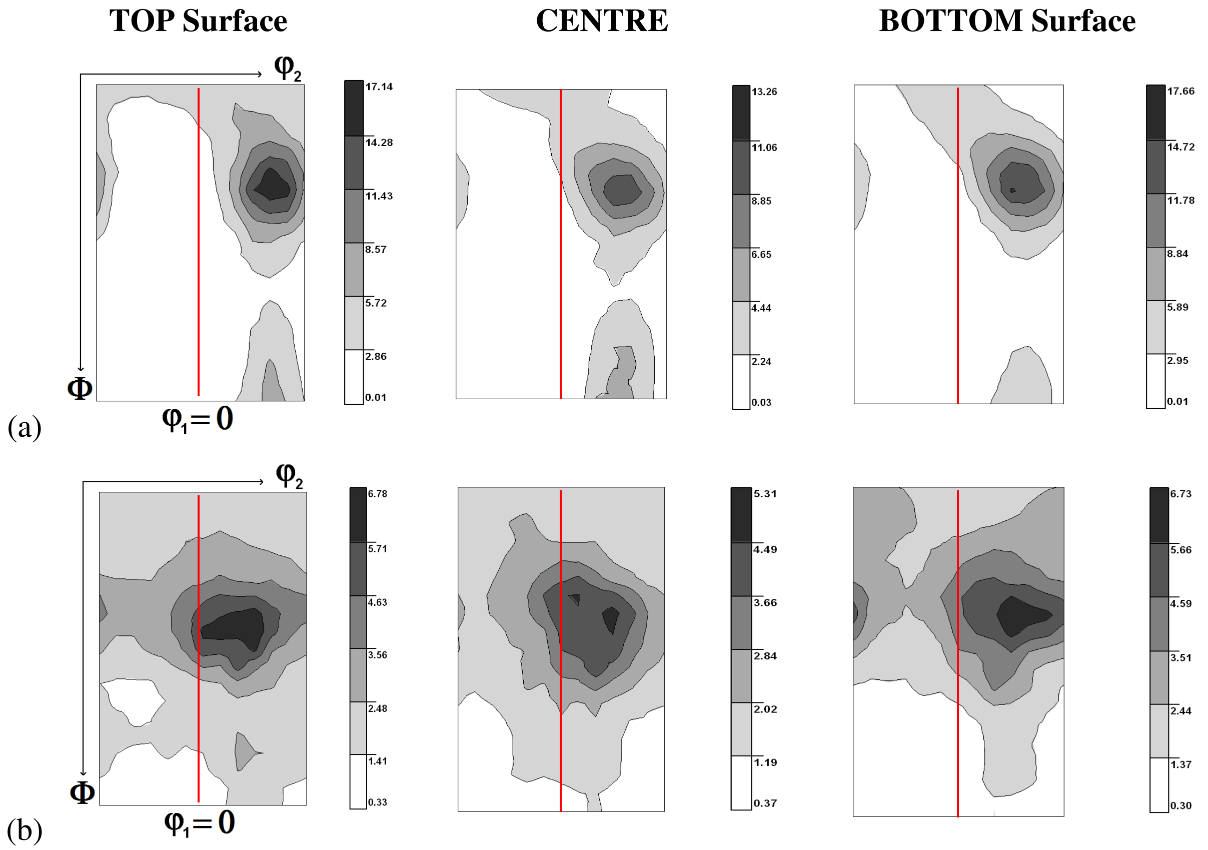

Fig. 5.25. *Asymmetrically rolled textures of polycrystalline titanium ($A=\omega_1/\omega_2=1.3$): a) predicted by FEM+LW modelling, b) determined by EBSD technique.*

The observed shifts of texture maxima in $\varphi_1=0^0$ ODF section, visible in Figs 5.24 and 5.25, are caused by corresponding texture rotations around TD. To examine this effect, the volume of the modelled sample was divided again into eight layers as shown in Fig. 5.12. The similar analysis as that for aluminium (cf. section 5.3.3) was done. We considered that a texture of a given layer can be related to the SR texture of the middle layer (Fig. 5.24 b - centre) by a rotation Ω around *TD*. The estimated rotation angle Ω vs. depth for different degrees of asymmetry *A*, is shown in Fig. 5.26. In the SR sample the rotation angle Ω changes the sign, when passing from the top to the bottom of the sample (in the centre being zero). In contrast, after AR with $A\geq1.3$ the rotation angle has the same sign and with increasing degree of asymmetry the relation of Ω vs. depth becomes nearly constant. This shows that AR leads to a nearly homogeneous texture across the material (in contrast to SR). The same effect was observed for AR aluminium (cf. Fig. 5.13).

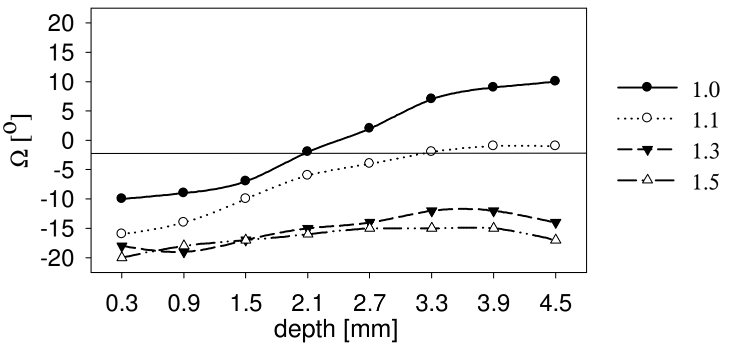

Fig. 5.26. Rotation angle Ω vs. depth for textures from different layers of titanium sample with reference to the texture of the centre layer of symmetrically rolled material. The following rolling asymmetry ratios, $A=\omega_1/\omega_2$, were considered: 1.0, 1.1, 1.3 and 1.5.

Another illustration of texture variation across the sample is shown in Fig. 5.27. The variation of correlation factor *R* between textures at different depths and the reference SR texture from the central layer is shown (analogous result is presented in Fig. 5.14 for aluminium).

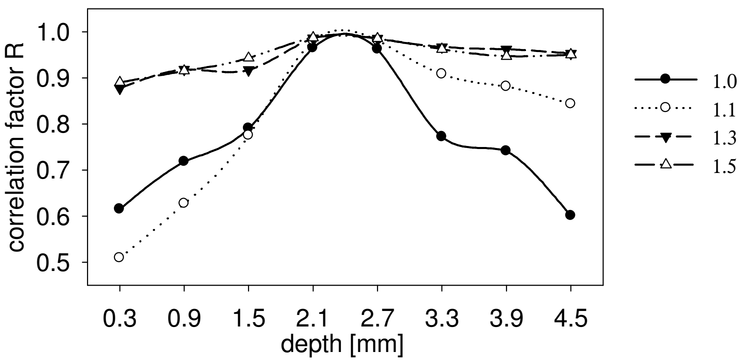

Fig. 5.27. Correlation factor R expressing similarity of textures from different layers of titanium sample with the reference SR texture of the centre layer. The following degrees of rolling asymmetry, $A=\omega_1/\omega_2$, were considered: 1.0, 1.1, 1.3 and 1.5.

Here again, we see that for low *A* (*A*=1.0 and A=1.1) texture varies significantly across the sample, while for *A*=1.3 and *A*=1.5 we observe much more flat relation.

Another important issue is a possible influence of twinning mechanism on crystallographic textures. The comparison of textures predicted under two assumptions: !) only slip systems were active, and !!) slip and twinning systems were active - is presented in Fig. 5.28. It is visible that introduction of twinning does not modify radically the predicted textures - compare Figs. 5.28 a and 5.28 b. The effect introduced by twinning, observed mainly in the centre layer, consists in a slight reinforcement of the maximum placed at $\phi=90^0$ and $\varphi_2=30^0$ in the $\varphi_1=0^0$ ODF section.

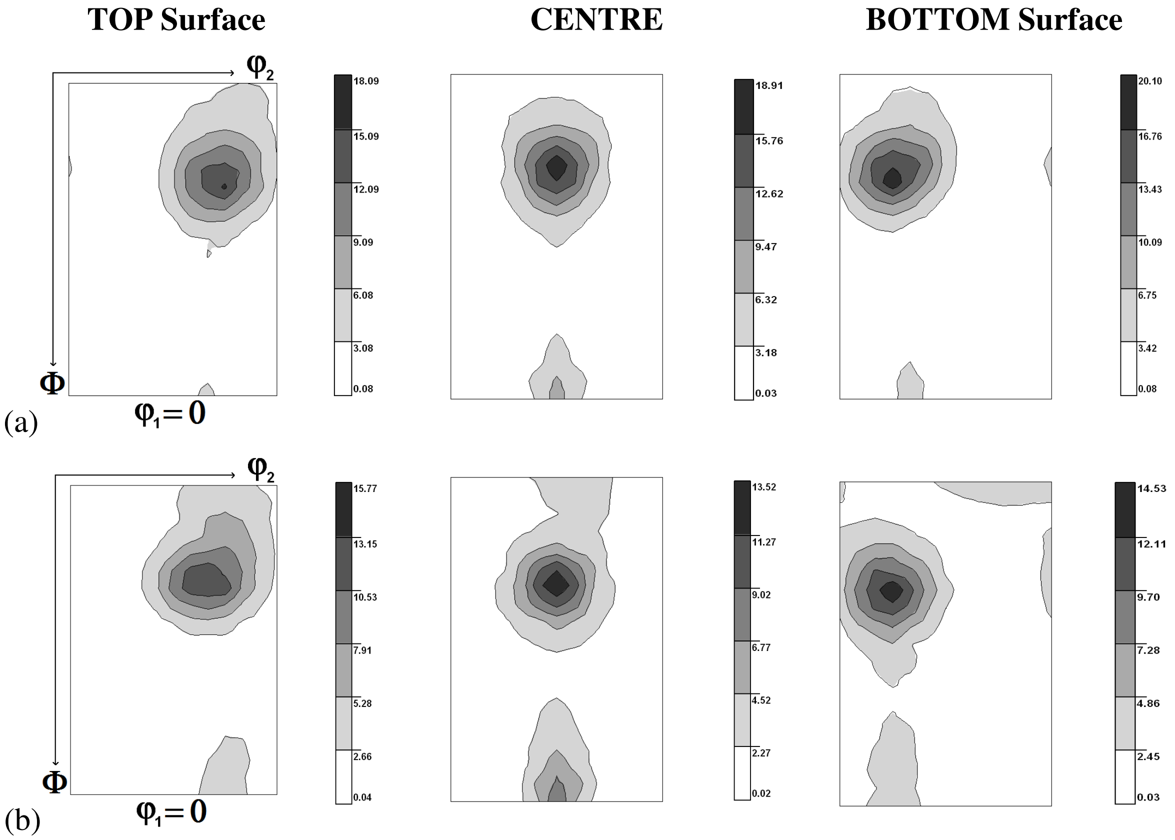

***Fig. 5.28**. Comparison of symmetrically rolled textures of polycrystalline titanium (A=ω_1/ω_2 =1.0) predicted by FEM+LW model under two assumptions: a) only slip systems were active, b) slip and twinning systems were active.*

Finally, the result concerning the twinned volume proportion across the sample, is presented in Fig. 5.29, where the fractions of tensile, compressive and of total twin volume vs. depth are shown. In order to avoid the influence of texture variation between different finite elements, we used exactly the same initial 150 lattice orientations of grains associated with each finite element; their orientation distribution represented the initial experimental titanium texture shown in Fig. 4.13. Regarding the total twin volume fraction (Fig. 5.29 a) we can conclude that it has the highest value near two sample surfaces (top and bottom) for all considered rolling asymmetries. The tensile twins show a similar behaviour for *A*=1.0 *A*=1.1, while for higher *A* values more flat curves are observed. In contrast, higher volume fractions of compressive twins appear generally near the sample surfaces in the case of AR (*A*=1.3 and *A*=1.5).

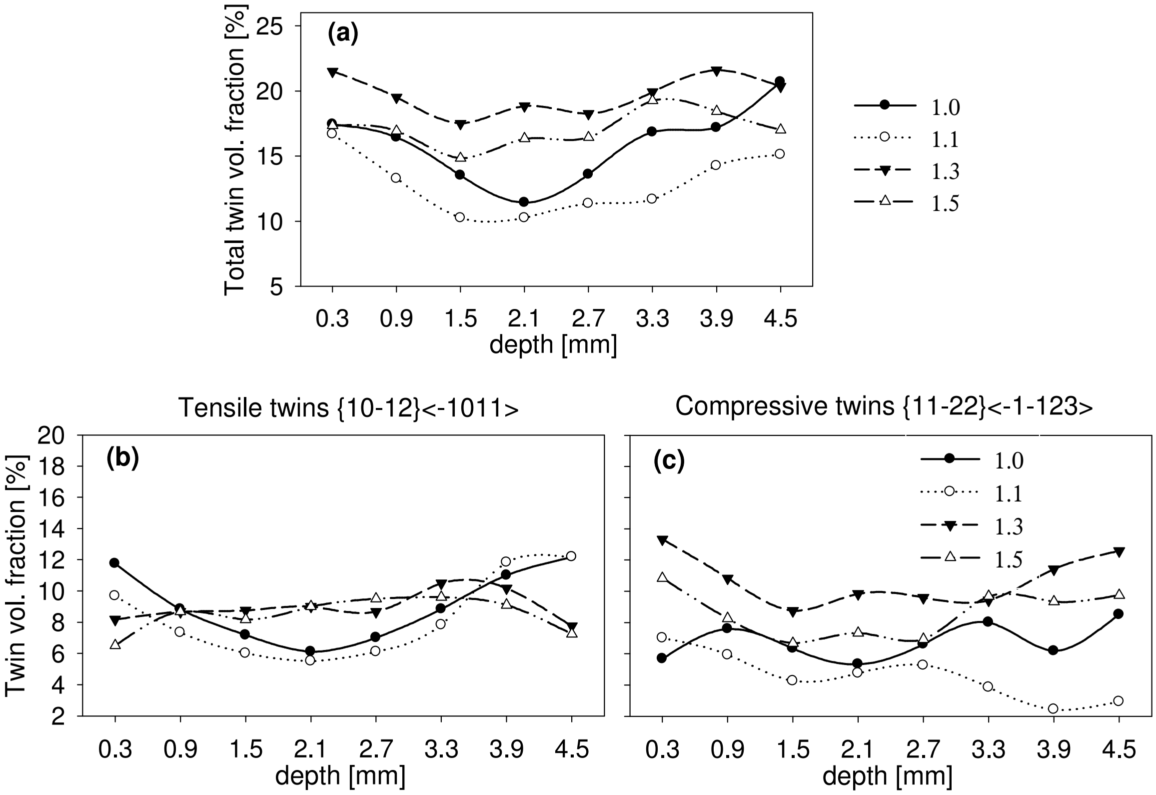

Fig. 5.29*. Calculated twinned volume fractions versus depth in the sample: a) total twined volume fraction, b) tensile twins volume fraction, c) compressive twins volume fraction. Results for rolling asymmetries A=1.0, 1.1, 1.3, 1.5 are shown.*

5.5 Conclusions

Basing on FEM calculations, we find the following properties of AR and resulting material properties:

- during AR the Σ_{13} shear stress component has nearly homogeneous distribution across the sample, while during SR it changes the sign in the surface layers,
- as a consequence of the above, textures of aluminium and titanium after AR are quite homogeneous across the sample. This is expressed by the same shift of texture maxima in three considered sample layers, as well as by a flat relation of the correlation factor *R* vs. depth (*R* expresses similarity of a texture from a given layer with the reference texture from the centre layer of SR material). In contrast, SR leads to more heterogeneous texture distribution in the material,

- the value of Σ_{33} internal stress component decreases with increasing rolling asymmetry. This confirms the advantages of AR: it reduces the applied normal forces necessary to perform the required deformation. The normal force and applied torque are smaller in AR than in SR, which is favourable for the mill durability.
- the bend flash appearing after AR varies with the degree of asymmetry (A) and with deformation; it can be minimized choosing optimal process parameters,
- friction coefficient between rolls and a material modifies the internal stress distribution,
- AR can be used to modify the plastic anisotropy of material. In the case of aluminium the largest differences between AR and SR appear: in the centre sample layer at $\alpha=45^0$, in top layer at $\alpha=90^0$ and in the bottom layer at $\alpha=0^0$ and $\alpha=90^0$ (α is the angle between RD and a given direction in the rolling plane).

It should be also noted that though the developed FEM+LW model was applied in the case of AR, it can be also used for other deformation geometries like deep drawing, extrusion or stamping.

General conclusions

We have examined the crystallographic mechanisms of plastic deformation of f.c.c. and h.c.p. metals. For this purpose the LW model was used. Our attention was focused on the deformation mechanisms of aluminium (6061) and titanium (grade 2).

The main problem concerning textures of f.c.c. metals is the appearance of two types of rolling texture, i.e. the brass and copper-type textures, in spite of the same crystalline structure and basically the same operating slip systems, i.e., {111}<110> ones. It should be recalled that in aluminium the copper-type rolling texture is developed. There is a long discussion in the literature about the problem of 'copper-brass' texture transition. A few factors were taken into account in the study of this problem in the present work: type of definition of crystal rotation, appearance of twinning mechanism and activation of additional slip systems (slip by partial dislocations, activation of cross-slip systems or of non-octahedral slip systems). The calculations performed in this work lead to the following conclusions:
- the formation of the *brass type texture* is the most successfully predicted using the {111}<110> slip in the frame of a weak interaction model (low *L* values) with *PR lattice rotation definition*. This model leads to a single and duplex slip deformation pattern. According to experimental observations, such the behaviour is favoured by thin twin lamella, which are formed in α-brass. They confine the dislocation movement to principal slip systems, hence they impose a single and duplex slip. The formation of thin twin lamella should not to be confused with the *volume twinning*; the latter does not appear in α-brass in sufficient quantity at room temperature. In addition, the sharpness of such predicted brass-type texture can be moderated by adding random stresses, which leads to a better agreement with experimental texture. The other considered mechanisms (volume twinning, slip by partial dislocations, activity of non-octahedral slip systems, cross-slip) do not improve the agreement with experimental brass texture.

In contrast, formation of the *copper-type texture* is much easier to explain. It is predicted assuming a strong interaction level (high *L* values) and the {111}<110> slip. The best agreement with experimental copper texture is obtained with *CL definition of rotation*.

The deformation mechanisms of pure titanium, leading to texture predictions close to experimental data, are: slip systems: $\{10\bar{1}0\}\langle 11\bar{2}0\rangle$ (prismatic), $\{0001\}\langle 11\bar{2}0\rangle$ (basal <a>), $\{10\bar{1}1\}\langle 11\bar{2}0\rangle$ (pyramidal <a>) and twinning systems: $\{10\bar{1}2\}\langle\bar{1}011\rangle$ (tensile twins) and

$\{11\bar{2}2\}\langle\bar{1}\bar{1}23\rangle$ (compressive twins). However, it was found in our EBSD measurements that twin volume fraction in titanium strongly decreases with deformation and our calculations confirmed a relatively small influence of twinning on the predicted textures already for medium deformations.

In more complex plastic deformations, like asymmetric rolling, a strongly heterogeneous microstructure is produced. Classical 1-point deformation models, do not describe sufficiently this heterogeneity. This was the reason why LW model was implemented into Finite Element Method and as a result the LW+FEM model was created. This software was tested first, successfully, on the examples of tension stress-strain curves of aluminium and titanium. After these verifications the LW+FEM model was used for a study of internal stress and texture heterogeneity in asymmetrically rolled materials.

Polycrystalline aluminium and titanium were rolled symmetrically and asymmetrically with different rolling asymmetries. The experimental laboratory rolling mill, used in our study, had two identical rolls driven by independent motors, which assured the range of rolling asymmetry, $A=\omega_1/\omega_2$, between 1 and 1.5. The process of AR causes many material modifications. Our EBSD study performed for aluminium and titanium showed that AR leads to:

- *grain refinement* in the range of low deformations (it should be noted that in this range the EBSD technique gives reliable results),
- *systematic grain refinement in materials rolled asymmetrically to higher reductions and then annealed.* This result is of potential importance for industrial applications,
- generally, *stronger fragmentation inside grains* (expressed by higher values of the average grain orientation spread and of the Kernel average misorientation) ,
- *texture modification* (by rotation around the transverse direction) and its homogenization across the material thickness.

The LW+FEM model was used to study the AR process and resulting material properties. The theoretical analyses were done for polycrystalline aluminium and titanium. These results explained some of our experimental observations and confirmed other effects reported in the literature. The main findings are listed below:

During AR the Σ_{13} shear component of internal stress has a nearly homogeneous distribution across the sample thickness (which is not the case during SR). As a consequence, the textures of aluminium and titanium after AR are quite homogeneous across the sample thickness. In contrast, the SR leads to more heterogeneous texture distribution. These predictions are in agreement with experimental results.

Only moderate modifications of titanium textures were predicted, when twinning was introduced (in the range of medium deformations). The calculated twinned volume fraction of a material varies versus depth in rolled samples and depends on a degree of the rolling asymmetry.

The applied normal force and torque are smaller in AR than in SR, which is favourable for mill durability. The bend flash appearing after AR, which in many cases is undesired effect, varies with the degree of rolling asymmetry (A) and with deformation; it can be minimized choosing optimal process parameters. The friction coefficient between rolls and a material modifies internal stress distribution.

Our calculations also confirm that AR can be used to modify the plastic anisotropy of materials (as a consequence of texture modification). The most important modifications appear in the central and two surface layers of the rolled material.

It can be also noted that the developed FEM+LW software, besides of application to symmetric and asymmetric rolling, can be also used for other deformation geometries like deep drawing, extrusion or stamping.

List of symbols and abbreviations

Symbols:

Σ_{ij} - tensor of internal or applied stresses,

σ_{ij} - tensor of residual or grain stress,

E_{ij} - sample deformation tensor,

ε_{ij} - grain deformation tensor,

f - volume fraction of a grain,

$\boldsymbol{n}$, $\boldsymbol{m}$ - unit vectors of slip plane and direction,

$\boldsymbol{K_1}$, $\boldsymbol{\eta_1}$ – unit vectors of twin plane and direction,

L - coefficient of grain-matrix interaction,

α' - elasto-plastic accommodation parameter,

α – the angle between axis and the rolling direction,

ν - Poisson coefficient,

G- the shear modulus,

E - Young's modulus,

ρ - density of a material,

δe_{ij} - tensor of displacement gradient,

$\sigma_{(hkl)[uvw]}$ - shear stress in a considered slip system,

ω_{ij} - rotation tensor,

$(hkl)[uvw]$ - slip or twinning system,

$\{hkl\}<uvw>$ - family of slip or twinning system,

τ_c and τ_0 - critical shear stress for slip (or twinning) and its initial value,

$\delta\gamma$- slip shear increment,

H_{ij}, h_0 , d - hardening matrix, its amplitude and hardening anisotropy parameter,

q^{ij} - describes the „structure" of hardening matrix,

τ_{sat}, h_{sat} - parameters of saturating law of hardening,

φ_1 ,Φ, φ_2 - Euler angles,

F_T, F_R, F_E, δg_{ij}, g_{ij} – threshold value for twinning mechanism and associated parameters,

Σ, Σ^0, $\Delta\Sigma$, k, - external stress tensor amplitude; initial value, increment value and k increments indicator,

$\boldsymbol{a_1}, \boldsymbol{a_2}, \boldsymbol{a_3}, \boldsymbol{c}$ – unit vectors for h.c.p. elementary cell,

(hkil)[prst] - Bravais-Miller indices of planes and directions (in h.c.p. structure),

R, R_C, R_B - correlation factor, its correlation factor for copper texture and brass,

g_A - crystal orientation,

$\sigma_{ij(rand)}$ – tensor of 'random stresses'

C, B, S, G, W, RW – ideal orientation in f.c.c. structure: copper, brass, S, Goss, Cubic and rotated Cubic components,

Δt - time increment,

u - acoustic wave speed,

h - length of final element,

Σ_{ij}^{Old} – stress old tensor in a given ABAQUS increment,

Σ_{ij}^{New} – stress new tensor in a given ABAQUS increment,

A - asymmetry ratio ($A = \omega_1/\omega_2$),

$\langle S\rangle_{number}$, $\langle S\rangle_{area}$ - average grain area (*number, area*),

S_i , v_i area and fraction of the *i-th* grain in a measured map,

p- pressure,

μ - friction coefficient,

F_{SR} , F_{AR} - normal force for symmetric and asymmetric rolling,

W_{AR} , W_{SR} – external work for symmetric and asymmetric rolling,

Ω - angle of a texture rotation around TD,

Δ - amplitude of lattice rotation,

K - proportionality factor of Σ_{13} stress component,

R_L - Lankford coefficient.

Abbreviations:

AR - asymmetric rolling,

ARB - Accumulative Roll Bonding,

AGOS - average grain orientation spread

CAE - Complete ABAQUS Environment,

CEC - Cyclic Extrusion Compression,

CL - classical rotation definition,

EBSD - Electron Back Scatter Diffraction, ECAP - Equal Channel Angular Pressing,

f.c.c. – face-centered cubic structure,

FEM - Finite Elements Method,

h.c.p. – hexagonal close packed structure,

HPT - High Pressure Torsion,

IE - internal energy,

IPF - Inverse Pole Figure,

KAM - Kernel Average Misorientation,

KE - kinetic energy,

LSPM - Laboratoire des Sciences des Procédés et des Matériaux,

LW - Leffers-Wierzbanowski model,

ND - normal direction,

ODF - Orientation Distribution Function,

OIM - Orientation Imaging Map,

PR - preservation condition definition for rotation,

RD - rolling direction,

SPD - severe plastic deformation,

SR - symmetric rolling,

TD - transverse direction,

UFG - ultra-fine grain.

Reference

[1] T. Leffers, “Computer Simulation of the Plastic Deformation in Face-Centred Cubic polycrystals and the Rolling Texture Derived,” *Phys. Stat.Sol,* vol. 25, pp. 337-344, 1968.

[2] T. Leffers, *Scripta Met.,* vol. 1, p. 1121, 1968.

[3] K. Wierzbanowski, in *PhD Thesis, AGH University of Science and Technology*, Krakow, 1978.

[4] K. Wierzbanowski, “Generalized Computer Program for Texture Simulation,” *Arch. Hutn.,* vol. 27, p. 189, 1982.

[5] K. Wierzbanowski, J. Jura, W. Haije and R. Helmholdt, “FCC Rolling Texture Transitions in Relation to Constraint Relaxation,” *Crystal Research and Technology,* vol. 27, pp. 513-522, 1992.

[6] K. Wierzbanowski, A. Baczmanski, P. Lipinski and A. Lodini, “Elasto-plastic models of polycrystalline material deformation and their applications,” *Archives of Metallurgy and Materials,* vol. 52, pp. 77-86, 2007.

[7] K. Wierzbanowski and J. Jasieński, “Some Comments on Sachs and Taylor Type Deformation,” vol. 15, p. 585, 1981.

[8] K. Wierzbanowski, “Computer Simulation of Rolling Texture Formation in H.C.P. and Orthorhombic Metals,” *Scripta Met.,* vol. 13, p. 795, 1979.

[9] K. Wierzbanowski and Z. Jasieński, “Some Results of Examination of Rolling Texture Heterogeneity,” *Scripta Met.,* vol. 16, p. 653, 1982.

[10] R. Hill, “Continuum Micro-Mechanics of Elastoplastic Polycrystals,” *J. Mech. Phys. Solids,* vol. 13, p. 89, 1965.

[11] M. Berveiller and A. Zaoui, “An Extension of the self-consistent scheme to plastically flowing polycrystals,” *J. Mech. Phys Solids,* vol. 26, p. 325, 1979.

[12] P. Lipinski and M. Berveiler, “Elastoplasticity of micro-inhomogeneous metals at large strains,” *Int. Journal of Plasticity,* vol. 5, p. 149, 1989.

[13] A. Molinari, G. Canova and S. Ahzi, “A self Consistent Approach of the Large Deformation Polycrystal Viscoplasticity,” *Acta Met.,* vol. 35, p. 2983, 1987.

[14] R. Asaro and A. Needleman, *Acta Mater.,* vol. 33, pp. 923-953, 1985.

[15] R. Lebensohn and C. Tome, *Acta Mater.,* vol. 41, p. 2611, 1993.

[16] G. Sachs, “On the Derivation of a Condition of Flow,” *Z. Verein. Deutsch. Ing.,* vol. 72, p. 734, 1928.

[17] G. Taylor, “Plastic Strain of Metals,” *J. Inst Met.,* vol. 62, p. 307, 1938.

[18] E. Kroner, “Zur plastischen Verformung des Vielkristalls,” *Acta Met.,* vol. 9, p. 155, 1961.

[19] T. Lin, “Analysis of Elastic and Plastic Strains of a FCC Crystal,” *J. Mech. Phys. Solids,* vol. 5, p. 143, 1957.

[20] W. Hosford, “On Orientation Changes Accompanying Slip and Twinning,” *Texture of Crystalline Solids,* vol. 2, pp. 175-182, 1977.

[21] K. Wierzbanowski, “Numerical Prediction of Cross-Rolling and Compression Textures,”

Scripta Metallurgica, vol. 13, pp. 1117-1120, 1979.

[22] P. Franciosi, M. Berveiller and A. Zaoui, "Latent Hardening in Copper and Aluminium Single Crystals," *Acta Met.,* vol. 28, p. 273, 1980.

[23] T. Leffers and R. Ray, "The brass-type texture and its derivation from the copper-type texture," *Progress in Materials Science,* vol. 54, pp. 351-396, 2009.

[24] J. Grewen and G. Wasserman, "The role of mechanical twinning in deformation of f.c.c. metals," in *Formation mechanisms and structure of the rolling texture of f.c.c. metals, Recristallization, Grain Growth and Structure*, London, American Society for Metals, Chapman & Hall, 1966, pp. 382-385.

[25] J. Kallend and G. Davies, "A simulation of texture development in f.c.c. metals," *Phil. Mag.,* vol. 25, pp. 471-490, 1972.

[26] C. Tome, R. Lebensohn and U. Kocks, "A model for texture development dominated by deformation twinning. Application to zirconium alloys," *Acta Metal. Mater.,* vol. 39, pp. 2667-2680, 1991.

[27] W. Wen, S. Gull and S. Ahzi, "Rolling texture transition in FCC metals using the viscoplastic ϕ-model and considering mechanical twinning," *Mater. Sci. Forum,* Vols. 702-703, pp. 241-244, 2012.

[28] C. Reid, Deformation geometry for materials scientists, Pergamon Press, 1973.

[29] F. v Göhler and G. Sachs, "Walz- Rekristallisationstextur regular-flächenzentrierter," *Metalle III. Z. Physik,* vol. 56, pp. 477-484, 1929.

[30] H. Hu, P. Sperry and P. Beck, "Rolling textures in face-centered cubic metals," *J. Metals,* vol. 4, pp. 76-81, 1952.

[31] P. Van Houtte, L. Delannay and I. Samajdar, "Quantitative prediction of cold rolling textures in low- carbon steel by means of the lamel model," *Textures and Microstructures,* vol. 31, pp. 109-149, 1999.

[32] C. Lee and B. Duggan, "Deformation banding and copper-type rolling textures," *Acta Metal. Mater.,* vol. 41, pp. 2691-2699, 1993.

[33] T. Leffers, "A model for rolling deformation with grain subdivision. Part II: The subsequent stage," *Int. J. Plasticity,* vol. 17, pp. 491-511, 2001.

[34] G. Sarma and P. Dawson, "Texture predictions using a polycrystal plasticity model incorporating neighbour interaction," *Int. J. Plasticity,* vol. 12, pp. 1023-1054, 1996.

[35] R. Lebensohn, "N-site modeling of a 3D viscoplastic polycrystal using fast Fourier transform," *Acta Mater.,* vol. 49, pp. 2723-2737, 2001.

[36] J. Tarasiuk and K. Wierzbanowski, "Application of the Linear Regression Method for Comparison of Crystallographic Textures," *Phil. Mag. A,* vol. 73, pp. 1083-1091, 1996.

[37] B. Duggan, M. Hatherly, W. Hutchinson and P. Wakefield, "Deformation structures and textures in cold-rolled 70:30 brass," *Metal Sci.,* vol. 12, pp. 343-351, 1978.

[38] F. Haessner, "Zur Theorie der Walztexturen kubisch flächenzentrierter," *Metalle. Z. Metallkde,* vol. 54, pp. 98-111, 1963.

[39] H. Hu, R. Cline and R. Goodman, "Recrystallization, Grain Growth and Textures," *American Society for Metals, Metals Park,* pp. 295-367, 1966.

[40] K. Wierzbanowski, "Computer Simulation Study of Texture Transitions in F.C.C. Metals and Alloys," in *Proc. of the 5-th Intern. Conf. on Textures of Materials, Ed. by G.Gottstein and Lucke*, Berlin, 1978.

[41] U. Kocks, C. Tome and H. Wenk, Texture and Anisotropy, Cambridge: Cambridge

University Press, 1998.

[42] R. Lebensohn and T. Leffers, “The Rules for the lattice rotation accompanying slip as derived from a self consistent model,” *Textures and Microstructures,* vol. 31, pp. 217-230, 1999.

[43] T. Leffers and R. Lebensohn, “Ambiguities in the calculation of lattice rotations for plane-strain deformation,” in *Proc. o the 11-th. Int. Conf. on Textures of Materials (ICOTOM-11), Z. Liang et al. eds., International Academic Publ.*, 1996.

[44] F. Haessner, “Formation mechanisms and structure of the rolling texture of f.c.c. metals, Recrystallization, Grain Growth and Structure,” in *American Society for Metals, Chapman & Hall*, London, 1966.

[45] K. Sekine, “Effect of Cube Plane Slip on the Development of Rollong Textures in f.c.c. metals,” *Transaction of the Japan Institute of Metals,* vol. 12, pp. 166-169, 1971.

[46] T. Leffers, “Texture prediction including non-octahedral slip,” in *proc. 15-th Riso Int. Syposium on Material Science: Numerical Prediction of Deformation Processes and the Behavior of Real Materials, Ed by S.I. Andersen et al.*, Riso Nat. Laboratory, Roskilde, Denmark, 1994.

[47] B. Bacroix and J. J. Jonas, “The influence of non-octahedral slip on texture development in f.c.c. metals,” *Textures Microstruct,* vol. 8/9, pp. 267-311, 1988.

[48] C. Maurice and J. Driver, “Hot rolling textures of aluminium,” *Mater. Sci. Forum,* Vols. 157-162, pp. 807-812, 1994.

[49] R. Smallmamn and D. Green, “The dependance of rolling texture on stacking fault energy,” *Acta Metall.,* vol. 12, pp. 145-154, 1964.

[50] I. Dillamore and W. Roberts, “Rolling textures in f.c.c. and b.c.c. metals,” *Acta Metall.,* vol. 12, pp. 281-293, 1964.

[51] L. A. Dobrzanski, Podstawy nauki o materiałach i metaloznawstwo, Warszawa: WNT Editions, 2002.

[52] P. Gangli and P. Arato, “Computer simulation study of the role of cross-slip in the formation of textures in f.c.c. metals,” *Phil. Mag.,* vol. 34, pp. 465-478, 1976.

[53] J. Kallend, U. Kochs, A. Rollet and H. Wenk, “Operational texture analysis,” Center for Materials Science, Los Alamos National Laboratoty, 1990.

[54] H. Hibbitt, B. Karlson and D. Sorensen, ABAQUS Analysis User's Manual Version 6.7, 2007.

[55] O. Zienkiewicz and R. Taylor, The finite element method,5th ed., Butterworth-Heinemann, Boston: Oxford, 2002.

[56] J. Jiang, Y. Ding, F. Zuo and A. Shan, “Mechanical properties and microstructures of ultrafine-grained pure aluminum by asymmetric rolling,” *Scripta Materialia,* vol. 60, p. 905–908, 2009.

[57] R. Valiev and T. Langdon, “Principles of equal-channel angular pressing as a processing tool for grain refinement,” *Prog. Mater. Sci.,* vol. 51, pp. 881-981, 2006.

[58] Y. Hwang and G. Tzou, “Analytical and experimental study on asymmetrical sheet rolling,” *Int. J. Mech. Sci.,* vol. 39, pp. 289-303, 1997.

[59] J. Sidor, A. Miroux, R. Petrov and L. Kestens, “Microstructural and crystallographic aspects of conventional and asymmetric rolling processes,” *Acta Materialia,* vol. 56, pp. 2495-2507, 2008.

[60] S. Wronski, B. Ghilianu, T. Chauveau and B. Bacroix, “Analysis of textures heterogeneity in cold and warm asymmetrically rolled aluminium,” *Materials Characterization,* vol. 62, no. 1, pp. 22-34, 2011.

[61] F. J. Simões, R. J. Alves de Sousa, J. A. Grácio, F. Barlat and J. W. Yoon, “Mechanical behavior of an asymmetrically rolled and annealed 1050-O sheet,” *International Journal of Mechanical Sciences,* vol. 50, pp. 1372-1380, 2008.

[62] S. Akbari Mousavi, S. Ebrahimi and R. Madoliat, “Three dimensional numerical analyses of asymmetric rolling,” *Journal of Materials Processing Technology,* vol. 187–188, p. 725–729 , 2007.

[63] A. Wauthier, H. Regle and J. Formigoni, “Gwenola Herman The effects of asymmetrical cold rolling on kinetics, grain size and texture in IF steels,” vol. 60, no. 2, p. 90–95, 2009.

[64] S. Wronski, J. Tarasiuk, B. Bacroix, A. Baczmanski and C. Braham, “Investigation of plastic deformation heterogeneities in duplex steel by EBSD,” *Mater. Charact.,* vol. 73, p. 52–60, 2012.

[65] H. Lu, P. Sivaprasad and C. H. J. Davies, “Treatment of misorientation data to determine the fraction of recrystallized grains in a partially recrystallized metal,” *Materials Characterizations,* vol. 51, pp. 293-300, 2003.

[66] H. Bunge, Texture Analysis in Material Science, United Kingdom: Butterworths London, 1982.

[67] Y. B. Chun, S. H. Yu, S. L. Semiatin and S. K. Hwang, “Effect of deformation twinning on microstructure and texture evolution during cold rolling of CP-titanium,” *Materials Science and Engineering A,* vol. 398, pp. 209-219, 2005.

[68] S. Y. Mironov, G. A. Salishchev, M. M. Myshlyaev and R. Pippan, “Evolution of misorientation distribution during warm 'abc' forging of commercial-purity titanium,” *Materials Science and Engineering A,* vol. 418, pp. 257-267, 2006.

[69] P. Gudur, M. Salunkhe and U. Dixit, “A theoretical study on the application of asymmetric rolling for the estimation of friction,” *International Journal of Mechanical Sciences,* vol. 50, p. 315–327, 2008.

[70] M. Salimia and F. Sassanib, “Modified slab analysis of asymmetrical plate rolling,” *International Journal of Mechanical Sciences,* vol. 44, no. 1999–2023, 2002.

[71] J.-S. Lu, O.-K. Harrer, W. Schwenzfeier and F. Fischer, “Analysis of the bending of the rolling material in asymmetrical sheet rolling,” *International Journal of Mechanical Sciences,* vol. 42, pp. 49-61, 2000.

[72] S. Wroński, K. Wierzbanowski, B. Bacroix, M. Wróbel, E. Rauch, F. Montheillet and M. Wroński, “Texture heterogeneity of asymmetrically rolled low carbon steel,” *Archives of Metallurgy and Materials,* vol. 54, pp. 89-102, 2009.

[73] M. Arminjon and B. Bacroix, “On plastic potentials for anisotropic metals and their derivation from the texture function,” *Acta Mechanica,* vol. 88, pp. 219-243, 1991.

[74] K. Wierzbanowski, M. Wroński, A. Baczmański, B. Bacroix, P. Lipinski and A. Lodini, “Problem of lattice rotation due to plastic deformation. Example of rolling of f.c.c. materials,” *Archives of Metallurgy and Materials,* vol. 56, pp. 575-584, 2011.

[75] S. Wronski, K. Wierzbanowski, B. Bacroix, M. Wrobel, T. Chauveau and M. Wronski, “Crystallographic Textures Variation in Asymmetrically Rolled Steel,” *Mater. Sci. Forum,* Vols. 638-642, pp. 2811-2816, 2010.

[76] M. Wronski, K. Wierzbanowski and T. Leffers, “On the lattice rotations accompanying slip,” *Materials Science and Technology,* vol. 29, pp. 129-133, 2013.

Author's publications

[A1] S. Wroński, K. Wierzbanowski, B. Bacroix, M. Wróbel, E. Rauch, F. Montheillet, **M. Wroński**, "Texture heterogeneity of asymmetrically rolled low carbon steel", *Archives of Metallurgy and Materials*, vol. 54, pp. 89-102, 2009.

[A2] S. Wroński, K. Wierzbanowski, B. Bacroix, M. Wróbel, T. Chauveau and **M. Wroński**, "Crystallographic Textures Variation in Asymmetrically Rolled Steel", *Mater. Sci. Forum*, vol. 638-642, pp. 2811-2816, 2010.

[A3] **M. Wroński**, K. Wierzbanowski, A. Baczmański, P. Lipiński, B. Bacroix, W. Seiler and A. Lodini, "Influence of grain-matrix interaction intensity and lattice rotation definition on predicted residual stresses and textures", *Mater. Sci. Forum*, vol. 681, pp. 405-410, 2011.

[A4] K. Wierzbanowski, **M. Wroński**, A. Baczmański, B. Bacroix, P. Lipinski and A. Lodini, "Problem of lattice rotation due to plastic deformation. Example of rolling of f.c.c materials", *Archives of Metallurgy and Materials*, vol. 56, pp. 575-584, 2011.

[A5] K. Wierzbanowski, **M. Wroński**, A. Baczmański, B. Bacroix, P. Lipinski and A. Lodini, "Some comments on lattice rotation in aspect of brass-copper texture transition", *Mater. Sci. Forum*, vol. 702-703, pp. 212-215, 2012.

[A6] **M. Wroński**, K. Wierzbanowski and T. Leffers, "On the lattice rotations accompanying slip", *Materials Science and Technology*, vol. 29, pp. 129-133, 2013.

[A7] K. Wierzbanowski, A. Baczmanski, R. Wawszczak, **M. Wroński**, M. Wróbel, A. Lodini, C. Braham, W. Seiler, "Residual stress in ferrite and austenite during rolling and recovery processes", *Mater. Sci. Forum*, 2013. – accepted, in print

[A8] K. Wierzbanowski, **M. Wroński**, A. Baczmanski, P. Lipinski, B. Bacroix, A. Lodini, "Effect of intergranular interaction and lattice rotation on predicted residual stress and textures. Case of austenite and ferrite", *Mater. Sci. Forum*, 2013. - accepted, in print

[A9] S. Wroński, K. Wierzbanowski, **M. Wroński**, B. Bacroix, "Three Dimensional Analysis of Asymmetric Rolling with Flat and Inclined Entry", *Archives of Metallurgy and Materials*, vol. 59, 2014. - accepted, in print

Conferences

[K1] S. Wroński, K. Wierzbanowski, B. Bacroix, M. Wróbel, T. Chauveau and **M. Wroński**, "Crystallographic Textures Variation in Asymmetrically Rolled Steel", Abstracts of Int. Conf.: THERMEC, p. 276**,** Berlin, 2009.

[K2] K. Wierzbanowski, **M. Wroński**, A. Baczmański, "Two Approaches to Lattice Rotation in Plastic deformation Models", Conference Proceedings : Frontiers in Modern Physics and Applications, Faculty of Physics and Applied Computer Science, AGH University of Science and Technology, pp. 115-117, Kraków, 2009.

[K3] K. Wierzbanowski, A. Baczmański, J. Tarasiuk, P. Lipiński and **M. Wroński**, "Mechanical model predictions for Al_3Mg_2 alloy", Abstracts of the 1st International Conference on Complex Metallic Alloys and their Complexity (C-MAC 1), p. 19, Nancy, France, 2009.

[K4] **M. Wroński**, K. Wierzbanowski, A. Baczmański, P. Lipiński and A. Lodini, "Influence of grain-matrix interaction intensity and lattice rotation definition on predicted residual stresses and textures", 8-th European Conference on Residual Stress (ECRS8), - Book of Abstracts p. 37, La Garda, Italy, 2010.

[K5] **M. Wroński**, K. Wierzbanowski, A. Baczmański, J. Tarasiuk, P. Lipiński and S. Wroński, "Predictions of mechanical properties of β-Al-Mg alloy- Example of compression and rolling", Poster Session Abstracts of Int. Conf.: C-MAC Days, p. 19, Max Planck Institute for Chemical Physics of Solids, Dresden, Germany, 2010.

[K6] K. Wierzbanowski, A. Baczmański, R. Wawszczak, **M. Wronski**, M. Wróbel, A. Lodini, C. Braham, W. Seiler, "Residual stress in ferrite and austenite during rolling and recovery processes", 6th International Conference on Mechanical Stress Evaluation by Neutrons and Synchrotron Radiation (MECA SENS VI), Book of Abstracts, p. 28 , Hamburg, Germany, 2011.

[K7] K. Wierzbanowski, **M. Wroński**, A. Baczmanski, P. Lipinski, B. Bacroix, A. Lodini, "Influence of intergranular interaction and lattice rotation on predicted residual stress and texture", Abstracts of 6th International Conference on Mechanical Stress Evaluation by Neutrons and Synchrotron Radiation (MECA SENS VI), p. 33, Hamburg, Germany, 2011.

[K8] K. Wierzbanowski, **M. Wroński**, A. Baczmański, B. Bacroix, P. Lipinski and A. Lodini, "Some comments on lattice rotation in aspect of brass-copper texture transition", Abstracts of 16-th Int. Conf. on Textures on Materials (ICOTOM 16), Bombay, India, 2011.

[K9] K. Wierzbanowski, **M. Wroński**, A. Baczmański and S. Wroński, "Effect of intergranular interaction and lattice rotation on predicted residual stress and texture for polycrystalline metals", Program for CMAC Days Abstract Booklet, p. 35, University of Liverpool, UK, 2011.

[K10] **M. Wroński**, K. Wierzbanowski, S. Wroński, B. Bacroix and M. Wróbel, “Modification of polycrystalline metal properties by asymmetric rolling”, Annual Meeting of: European integrated centre for the development of Metallic Alloys and Compounds (C-MAC), Proceedings of C-MAC Days, p. 40, AGH University of Science and Technology, Kraków, Poland, 2012.

[K11] **M. Wroński**, “Implementation of polycrystalline deformation model into finite elements method code”, *Proceedings of the ISD Workshops*, Faculty of Physics and Applied Computer Science AGH University of Science and Technology, pp. 45-48, Kraków, Poland 2013.

[K12] **M. Wronski**, K. Wierzbanowski, S. Wronski, B. Bacroix, A. Lodini, P. Lipinski, "Study of texture development in asymmetrically rolled titanium. Experimental study and calculations", Colloque de l’Association Française de Cristallographie, Programme et résumés, p.115, Bordeaux, France, 2013